Toward a Model System for Understanding Vibrational Coherence Transfer

by

Joseph H. Meadows

A dissertation submitted in partial fulfillment
of the requirements for the degree of
Doctor of Philosophy
(Chemistry)
in the University of Michigan
2023

Doctoral Committee:

Professor Kevin Kubarych, Chair
Professor Steven Cundiff
Professor Eitan Geva
Professor Roseanne Sension

Joseph H. Meadows

jhmea@umich.edu

ORCID iD: 0009-0005-6302-7299

© Joseph H. Meadows, 2023

All Rights Reserved

Dedication

To my grandfather, Richard Shaffer

Acknowledgments

Since I first claimed the desk I would have for the majority of my graduate career, I have had a quote from Jacob Bronowski's *The Ascent of Man* pinned to its backdrop that says, "Science is a very human form of knowledge. We are always at the brink of the known, we always feel forward for what is hoped. Every judgment in science stands on the edge of error and is personal. Science is a tribute to what we can know although we are fallible." The last seven years have been overwhelming and, at times, incredibly disheartening. Looking back over my time at Michigan, I think I was prepared for my science to be difficult. I was not, however, prepared for how difficult everything outside of my science would be. By far the most human element of science is the support its pursuit requires, and I would like to honor those who have supported me during my own pursuit of what we can know.

First and foremost, I would like to thank my advisor, Kevin Kubarych, who has been endlessly supportive of me and my science, particularly when I did not have the wherewithal to see the next steps, either personally or professionally. Kevin has been a fantastic boss over the last seven years and has always emphasized that he's just as invested in my wellbeing as a person as he is my success as a scientist. I would also like to thank my thesis committee for their wisdom, input, and patience as I scrambled to put my defense together on short notice.

Next, I have to thank the present and past members of the Kubarych group, who have been phenomenal coworkers and friends through the most challenging years of my life. You have all encouraged and inspired me to be a more thoughtful and collaborative scientist. Specifically, I want to thank Lindsay Mantell, Rong Duan, Vivian Crum, and Katie Barnes for their care and companionship throughout the years. I had the privilege to officiate Lindsay and Mark's wedding, and I will forever be grateful for them as friends and confidants. I would like to extend a special thanks to the Kubarych group's current members: Vivian and Katie. The two of them single-handedly kept me sane during this last home stretch, and I will deeply miss our coffee runs and movie nights.

I would have been completely lost without the incredible people I am fortunate to count as my friends. To Audrey, thank you for helping me remember the importance of personal pizzas and the joy of choosing to not know characters' names. To Ciara and Hannah, I'm sorry that I'm leaving Michigan right as we were all going to be in Ann Arbor again. To Kenny, thank you for being my most constant friend. To Taylor, thank you for reminding me to go outside when things inside get too stressful. To Heather, thank you for being a beacon of queer joy. I'm so glad we've both found ourselves time after time. To Nic, thank you for reminding me that there's a world outside of grad school. To Liz and Jack, thank you for matching my energy with boundless enthusiasm. To Eri and Salem, thank you for giving me new episodes of the podcast to listen to when I'm on the bus. To Nico, Josh, and Marina, thank you for making a space for me to crash when most everyone else I knew in town had left. To my D&D group, thank you for always meeting my bad ideas with a "yes, and?"

During the last seven years, I've found myself at a mix of dinner tables, life events, and family holidays. I have found an abundance of joy in my friends' families as they have welcomed me with open arms. To the Tolberts, thank you for refusing to let me spend the beginning of covid alone in my apartment. To the Reynolds, thank you for giving me a home during the holidays. To the Chapmans (and Jacob), thank you for becoming my family. There's really no way for me fully express just how much it means to know I have you all in my corner.

Finally, I need to thank the two people who are the center of my entire world. To Cole, thank you for being my other half. I've never found cause for as much celebration and concern as I have in our friendship, and I am forever grateful to have found a person as conscientious and compassionate as you. I do apologize for the coffee cups of whiskey I've made you drink with me over the years, but I am so thankful that you've always been there to lean on when I'm unsure of myself. Thank you for driving me to mystery midnight MRIs and for always being willing to jump headfirst into a mosh pit with me. To Holly, thank you for being the best sister a person could ask for. Throughout our friendship, you've inspired me to continually mirror the growth that you embody so wonderfully. I am incredibly proud of the person I've seen you become, and I am undoubtedly a better version of myself because every time I see you, I see the effort and care with which you navigate the world. Thank you for keeping me stocked up on Aloha shirts and always making time even though you're incredibly busy becoming a real doctor. Both of you are why I'm here. I love you both endlessly.

Table of Contents

Dedication ii
Acknowledgments iii
List of Figures viii
List of Tables xvii
List of Abbreviations xvii
Abstract xx
Chapter 1: Introduction 1
1.1 Introduction 1
1.2 Metal Carbonyls 6
1.2.1 Dicobalt Hexacarbonyl Complexes 8
1.2.2 Applications and Synthesis of Dicobalt Hexacarbonyl Complexes 9
1.2.3 Assignment of Vibrational Modes in DCHC 11
1.3 Two-Dimensional Infrared Spectroscopy 14
1.3.1 2D-IR Experimental Apparatus 15
1.3.2 Third-Order Response and Double-sided Feynman Diagrams 17
1.3.3 General Interpretation of 2D-IR spectra 21
1.3.4 Analysis of t_2 coherences in 2D-IR 23
1.4 Redfield Theory 26
1.4.1 The Secular Approximation 27
1.4.2 Coherence Transfer 28
1.5 Outline 30
Chapter 2: Alkyl-Substituted Dicobalt Hexacarbonyl Complexes as a Platform for Investigating Vibrational Coherence Transfer 32
2.1 Introduction 32
2.2 Experimental Methods 34
2.3 Results 36
2.4 Discussion 41

2.5 Conclusion 45
Chapter 3: Aryl-Substituted Dicobalt Hexacarbonyl Complexes as an Electronically Tunable Model System for Vibrational Coherence Transfer 46
3.1 Introduction 46
3.2 Experimental Methods 48
3.3 Results 50
3.4 Discussion 56
3.5 Conclusion 59
Chapter 4: Ultrafast Vibrational Dynamics of Alkynyl Dicobalt Hexacarbonyl Complexes in Alkane Solvent Environments 60
4.1 Introduction 60
4.2 Experimental Methods 64
4.3 Results 65
4.4 Discussion 68
4.5 Conclusion 70
Chapter 5: Conclusion 71
5.1 Key Results 71
5.2 Future Directions 72
Appendix 75
A.1 Derivation of the Redfield Equation 75
A.2 Assignment of Modes for Alkynyl DCHC Complexes 80
A.3 Difference Frequency Tables for Alkynyl DCHC Complexes 88
A.4 2D-IR Spectra of Selected DCHC Complexes in *n*-dodecane 90
References 93

List of Figures

Figure 1.1: Depiction of anharmonic coupling by way of (a) changes in a one-dimensional PES showing the effects of changes in a chemical bond with coordinate R with respect to stretching (dashed line) and compression (dotted line) on an anharmonic oscillator and (b) the motional narrowing of two excited states due to anharmonic coupling. Adapted from sources.[1,2] 1

Figure 1.2: (a) Formation of the metal-CO bond in metal carbonyls. (b) Metal carbonyl stretching frequency shifting with respect to the amount of π-backbonding in the metal-CO bond. 7

Figure 1.3: Structures of generic (a) μ-dithiolate diiron hexacarbonyl and (b) μ-η^2-η^2-alkynyl dicobalt hexacarbonyl complexes respectively, alongside computed structures of (c) μ-propane dithiolate (pdt) diiron hexacarbonyl and (d) μ-η^2-η^2-3-hexyne-dicobalt hexacarbonyl (3-hex DCHC). 9

Figure 1.4: (a) Pauson-Khand reaction, showing the 2+2+1 cycloaddition formation of a cyclopentenone from an alkyne, alkene, and $Co_2(CO)_8$. (b) Nicholas reaction, showing the $Co_2(CO)_8$ stabilzation of a propargylic ether during nucleophilic substitution. 10

Figure 1.5: Synthetic scheme for the formation of alkynyl DCHC complexes with a series of eight alkyne ligands. 11

Figure 1.6: (a) FTIR spectrum of 3-hex DCHC in n-heptane with computationally assigned vibrational modes for each peak and each carbonyl assigned a number 1-6. (b) Normalized displacements (in Å) of each carbonyl C≡O bond per mode, including mode 2*, which is not spectroscopically visible. 12

Figure 1.7: Pulse train for 2D-IR experiments showing excitation by the two pump pulses (teal) separated by the coherence time (t_1), the probe pulse (purple) separated by the waiting time (t_2), and the detection of the generated signal E_S. 15

Figure 1.8: Diagram of the 2D-IR experimental apparatus, with OPAs and DFGs simplified for clarity. 16

Figure 1.9: Noncollinear geometry used in 2D-IR experiments, denoting rephasing and nonrephasing signals generated by the scanning of the k_1 or k_2 motor, respectively. 17

Figure 1.10: Density matrix representation of the light-matter interactions in third-order spectroscopy, with populations occurring on the matrix diagonal (where n = m) and coherences on the off-diagonal (where n ≠ m). 18

Figure 1.11: Three-mode three-level system consisting of mode **a'** (in red), mode **a** (in orange), and mode **s** (in teal), their overtones, and combination bands (in purple) originating from a common ground state. 20

Figure 1.12: Double-sided Feynman diagrams representing six of the eight possible Liouville pathways both the rephasing and nonrephasing signals. For clarity, Dirac notation about each component has been omitted. 21

Figure 1.13: Cartoon representations of a three-mode system in (a) a linear absorption spectrum and (b) a 2D spectrum at an arbitrary waiting time such that $t_2 > 0$. ...22

Figure 1.14: Representation of the loss of correlation between excitation and detection frequencies at (a) early waiting times and (b) later waiting times. 24

Figure 1.15: Cartoon of (a) a 2D-IR spectrum of a three-mode system with a region of interest drawn around the upper crosspeak of modes **s** and **a'**, (b) a t_2 slice of the peak amplitude oscillating at $\Delta\omega_{sa'}$, and (c) the Fourier-transformation of the oscillation at $\Delta\omega_{sa'}$. 25

Figure 1.16: (a) Double-sided Feynman diagram for the rephasing crosspeak of mode **a** and mode **s** via t_2 coherence, and (b) a density matrix representation of that same crosspeak. (c) Double-sided Feynman diagram of that same crosspeak with a coherence-to-coherence transfer between mode **a** and mode **a'**, and (d) a density matrix showing the pathway of the coherence transfer event. 29

Figure 2.1: (a) Structures of the 3-hex, TMSi, and 1T1H DCHC complexes, and (b) linear absorption spectra of their metal carbonyl stretching modes in n-heptane. 35

Figure 2.2: Rephasing absolute value 2D-IR spectrum of 3-hex-DCHC in n-heptane with mode assignments and representations of the linear absorption spectrum along each frequency axis. 37

Figure 2.3: 2D-IR data for 3-hex-DCHC including (a) rephasing absolute value 2D-IR spectrum, (b) rephasing coherence map at ω_2 = 35-40 cm^{-1}, (c) rephasing coherence map at ω_2 = 60-65 cm^{-1}, (d) nonrephasing absolute value 2D-IR spectrum, (e) nonrephasing coherence map at ω_2 = 35-40 cm^{-1}, and (f)

nonrephasing coherence map at ω_2 = 60-65 cm^{-1}. Dotted lines have been added to show the upper limit of ω_2 for rephasing coherence maps. Red circles denote unexpected ω_2 intensities. 38

Figure 2.4: 2D-IR data for TMSi-DCHC including (a) rephasing absolute value 2D-IR spectrum, (b) rephasing coherence map at ω_2 = 35-40 cm^{-1}, (c) rephasing coherence map at ω_2 = 60-65 cm^{-1}, (d) nonrephasing absolute value 2D-IR spectrum, (e) nonrephasing coherence map at ω_2 = 30-35 cm^{-1}, and (f) nonrephasing coherence map at ω_2 = 60-65 cm^{-1}. Dotted lines have been added to show the upper limit of ω_2 for rephasing coherence maps. Red circles denote unexpected ω_2 intensities. 39

Figure 2.5: 2D-IR data for 1T1H-DCHC including (a) rephasing absolute value 2D-IR spectrum, (b) rephasing coherence map at ω_2 = 35-40 cm^{-1}, (c) rephasing coherence map at ω_2 = 60-65 cm^{-1}, (d) nonrephasing absolute value 2D-IR spectrum, (e) nonrephasing coherence map at ω_2 = 30-35 cm^{-1}, and (f) nonrephasing coherence map at ω_2 = 60-65 cm^{-1}. Dotted lines have been added to show the upper limit of ω_2 for rephasing coherence maps. Red circles denote unexpected ω_2 intensities. 40

Figure 2.6: (a) Calculated structure and (b) carbonyl displacement probabilities for 3-hex-DCHC as compared to (c) the calculated structure and (d) carbonyl displacement probabilities for 1T1H-DCHC. 41

Figure 2.7: Time-domain population slices and frequency-domain Frobenius spectra for the **3,6** crosspeak of (a, b) 3-hex-DCHC, (c, d) TMSi-DCHC, and (e, f) 1T1H-DCHC

featuring a prominent spectral feature at 64 cm^{-1}, indicating coherence-to-coherence transfer from **4,6** to **3,6**. 43

Figure 3.1: Molecular orbitals for ethynylpyrene-DCHC (EtPyr-DCHC) showing (a) the highest occupied molecular orbital (HOMO) and (b) the lowest unoccupied molecular orbital (LUMO) both with significant overlap between the alkyne ligand and the cobalt carbonyl moiety. 48

Figure 3.2: (a) Structures of the DPhA, EtPyr, EtFc, PhA, and PhTMSi DCHC complexes, and (b) linear absorption spectra of their metal carbonyl stretching modes in n-heptane. 49

Figure 3.3: Rephasing absolute value 2D-IR spectrum of EtPyr-DCHC in n-heptane with mode assignments and representations of the linear absorption spectrum along each frequency axis. 50

Figure 3.4: 2D-IR data for DPhA-DCHC including (a) rephasing absolute value 2D-IR spectrum, (b) rephasing coherence map at ω_2 = 30-45 cm^{-1}, (c) rephasing coherence map at ω_2 = 50-65 cm^{-1}, (d) nonrephasing absolute value 2D-IR spectrum, (e) nonrephasing coherence map at ω_2 = 35-40 cm^{-1}, and (f) nonrephasing coherence map at ω_2 = 50-60 cm^{-1}. Dotted lines have been added to show the upper limit of ω_2 for rephasing coherence maps. Red circles denote unexpected ω_2 intensities. 51

Figure 3.5: 2D-IR data for EtPyr-DCHC including (a) rephasing absolute value 2D-IR spectrum, (b) rephasing coherence map at ω_2 = 30-45 cm^{-1}, (c) rephasing coherence map at ω_2 = 50-65 cm^{-1}, (d) nonrephasing absolute value 2D-IR

spectrum, (e) nonrephasing coherence map at ω_2 = 35-40 cm^{-1}, and (f) nonrephasing coherence map at ω_2 = 50-60 cm^{-1}. Dotted lines have been added to show the upper limit of ω_2 for rephasing coherence maps. Red circles denote unexpected ω_2 intensities. 52

Figure 3.6: 2D-IR data for EtFc-DCHC including (a) rephasing absolute value 2D-IR spectrum, (b) rephasing coherence map at ω_2 = 30-45 cm^{-1}, (c) rephasing coherence map at ω_2 = 50-65 cm^{-1}, (d) nonrephasing absolute value 2D-IR spectrum, (e) nonrephasing coherence map at ω_2 = 35-40 cm^{-1}, and (f) nonrephasing coherence map at ω_2 = 50-60 cm^{-1}. Dotted lines have been added to show the upper limit of ω_2 for rephasing coherence maps. Red circles denote unexpected ω_2 intensities. 53

Figure 3.7: 2D-IR data for PhA-DCHC including (a) rephasing absolute value 2D-IR spectrum, (b) rephasing coherence map at ω_2 = 30-45 cm^{-1}, (c) rephasing coherence map at ω_2 = 50-65 cm^{-1}, (d) nonrephasing absolute value 2D-IR spectrum, (e) nonrephasing coherence map at ω_2 = 35-40 cm^{-1}, and (f) nonrephasing coherence map at ω_2 = 50-60 cm^{-1}. Dotted lines have been added to show the upper limit of ω_2 for rephasing coherence maps. Red circles denote unexpected ω_2 intensities. 54

Figure 3.8: 2D-IR data for PhTMSi-DCHC including (a) rephasing absolute value 2D-IR spectrum, (b) rephasing coherence map at ω_2 = 30-45 cm^{-1}, (c) rephasing coherence map at ω_2 = 50-65 cm^{-1}, (d) nonrephasing absolute value 2D-IR spectrum, (e) nonrephasing coherence map at ω_2 = 35-40 cm^{-1}, and (f)

nonrephasing coherence map at ω_2 = 50-60 cm^{-1}. Dotted lines have been added to show the upper limit of ω_2 for rephasing coherence maps. Red circles denote unexpected ω_2 intensities. 55

Figure 4.1: An illustration of (a) potential carbonyl stretching frequencies with respect to C≡O bond length, and (b) the spectral results of interconversion between the carbonyl populations over time. 62

Figure 4.2: (a) Structures of the 3-hex (blue), TMSi (orange), and EtPyr (yellow) DCHC complexes, and (b) linear absorption spectra of their metal carbonyl stretching modes in n-heptane. 64

Figure 4.3: 2D-IR spectra of 3-hex-DCHC in n-heptane at 0.5 ps, 10 ps, and 25 ps. 65

Figure 4.4: 2D-IR spectra of TMSi-DCHC in n-heptane at 0.5 ps, 10 ps, and 25 ps. 65

Figure 4.5: 2D-IR spectra of EtPyr -DCHC in n-heptane at 0.5 ps, 10 ps, and 25 ps. 66

Figure 4.6: Traces over t_2 for (a-c) rephasing peak amplitudes for mode **5** of 3-hex-DCHC (blue), TMSi-DCHC (orange), and EtPyr-DCHC (yellow) and (d-f) FFCFs for mode **5** of 3-hex-DCHC (blue), TMSi-DCHC (orange), and EtPyr-DCHC (yellow) in n-heptane. 66

Figure 4.7: Traces over t_2 for (a-c) rephasing peak amplitudes for mode **5** of 3-hex-DCHC (blue), TMSi-DCHC (orange), and EtPyr-DCHC (yellow) and (d-f) FFCFs for mode **5** of 3-hex-DCHC (blue), TMSi-DCHC (orange), and EtPyr-DCHC (yellow) in n-dodecane. 67

Figure 4.8: Rephasing Frobenius spectra of the **3,6** crosspeak in TMSi-DCHC in (a) n-heptane and (b) n-dodecane. 67

Figure 4.9: 2D-IR data for TMSi-DCHC in (a-c) n-heptane and (d-f) n-dodecane including (a and d) rephasing absolute value 2D-IR spectrum, (b and e) rephasing coherence map at ω_2 = 35-40 cm^{-1}, (c and f) rephasing coherence map at ω_2 = 60-65 cm^{-1}. 68

Figure 5.1: A series of ethynylfluorobenzene DCHC complexes. 73

Figure 5.2: Synthesis of a heterobimetallic iron-cobalt hexacarbonyl propargyl cation by isolobal substitution of cobalt tricarbonyl by iron pentacarbonyl.[73] 74

Figure A.1: (top-down) Linear absorption spectrum, normalized carbonyl displacements by vibrational mode, and carbonyl recruitment probability by vibrational mode for 3-Hex-DCHC. 80

Figure A.2: (top-down) Linear absorption spectrum, normalized carbonyl displacements by vibrational mode, and carbonyl recruitment probability by vibrational mode for TMSi-DCHC. 81

Figure A.3: (top-down) Linear absorption spectrum, normalized carbonyl displacements by vibrational mode, and carbonyl recruitment probability by vibrational mode for DPhA-DCHC. 82

Figure A.4: (top-down) Linear absorption spectrum, normalized carbonyl displacements by vibrational mode, and carbonyl recruitment probability by vibrational mode for EtPyr-DCHC. 83

Figure A.5: (top-down) Linear absorption spectrum, normalized carbonyl displacements by vibrational mode, and carbonyl recruitment probability by vibrational mode for EtFc-DCHC. 84

Figure A.6: (top-down) Linear absorption spectrum, normalized carbonyl displacements by vibrational mode, and carbonyl recruitment probability by vibrational mode for PhA-DCHC. 85

Figure A.7: (top-down) Linear absorption spectrum, normalized carbonyl displacements by vibrational mode, and carbonyl recruitment probability by vibrational mode for PhTMSi-DCHC. 86

Figure A.8: (top-down) Linear absorption spectrum, normalized carbonyl displacements by vibrational mode, and carbonyl recruitment probability by vibrational mode for 1T1H-DCHC. 87

Figure A.9: 2D-IR spectra of 3-hex-DCHC in n-dodecane, featuring (a-c) rephasing and (d-f) nonrephasing spectra at t_2 = 0.5 ps, 10 ps, and 25 ps. 90

Figure A.9: 2D-IR spectra of TMSi-DCHC in n-dodecane, featuring (a-c) rephasing and (d-f) nonrephasing spectra at t_2 = 0.5 ps, 10 ps, and 25 ps. 91

Figure A.10: 2D-IR spectra of EtPyr-DCHC in n-dodecane, featuring (a-c) rephasing and (d-f) nonrephasing spectra at t_2 = 0.5 ps, 10 ps, and 25 ps. 92

List of Tables

Table A.1: 3-hex-DCHC Frequency Table 88

Table A.2: TMSi-DCHC Frequency Table 88

Table A.3: DPhA-DCHC Frequency Table 88

Table A.4: EtPyr-DCHC Frequency Table 88

Table A.5: EtFc-DCHC Frequency Table 89

Table A.6: PhA-DCHC Frequency Table 89

Table A.7: PhTMSi-DCHC Frequency Table 89

Table A.8: 1T1H-DCHC Frequency Table 89

List of Abbreviations

DCHC: dicobalt hexacarbonyl

2D-IR: two-dimensional infrared

PES: potential energy surface

FMO: Fenna-Matthews-Olson

CO: carbon monoxide

PKR: Pauson-Khand reaction

DCO: dicobalt octacarbonyl

DFT: density functional theory

B3LYP: Beck, 3-parameter, Lee-Yang-Parr

LanL2DZ: Los Alamos National Laboratory 2 Double-Zeta

3-hex: 3-hexyne-dicobalt hexacarbonyl

TMSi: bis(trimethylsilyl)acetylene

DPhA: diphenylacetylene

EtPyr: ethynylpyrene

EtFc: ethynylferrocene

PhA: phenylacetylene

PhTMSi: 1-phenyl-2-trimethylsilylacetylene

1T1H: 1-trimethylsilyl-1-hexyne

RDC: rhodium dicarbonyl acetylacetonate

FTIR: Fourier-transform infrared

Mid-IR: mid-infrared

β-BBO: β-barium borate

OPA: optical parametric amplifier

DFG: difference frequency generation

FWHM: full-width at half-maximum

IVR: intramolecular vibrational redistribution

ROI: region of interest

DMDC: dimanganese dicarbonyl

SEC: spectroelectrochemistry

Abstract

Ultrafast vibrational dynamics, most often considered within the framework of the secular approximation of Redfield theory, have proven consistently sensitive to anharmonic coupling and nonsecular vibrational coherence transfer. While significant effort has been made to characterize vibrational coherence transfer in both small molecules and large, biological systems, no investigation thus far has studied vibrational coherence transfer with respect to systematic changes in molecular structure.

This work covers the investigation of a series of substituted alkynyl dicobalt hexacarbonyl (DCHC) complexes with ultrafast two-dimensional infrared (2D-IR) spectroscopy for the purpose of uncovering their propensity for vibrational coherence transfer. Originally developed as catalytic intermediates, DCHC complexes are small, air-stable organometallic molecules that involve the coordination of dicobalt octacarbonyl to a bridging alkyne via click chemistry. Their straightforward synthesis and relatively rigid molecular structure make the DCHC complexes a worthy class of molecules to use as the basis for a model system to elucidate the mechanisms by which vibrational coherence transfer occurs.

In total, this work focuses on a series of eight DCHC complexes, which vary significantly in chemical structure, molecular symmetry, and electronic nature in the pursuit of a systematic assessment of vibrational coherence transfer in small molecules.

Each complex is defined with regard to its appended ligand, which can be broadly separated into alkyl- and aryl-substituted alkynes and subdivided into symmetrically and asymmetrically substituted complexes. Although we observe significant changes in the vibrational modes of the eight complexes due to the effects of their ligands, we find compelling evidence for vibrational coherence transfer in all of them.

This dissertation, and its proposed future directions, presents a spectroscopic investigation into vibrational coherence transfer with respect to a series of systematically-substituted alkynyl DCHC complexes and serves as an extension to the work done by several past members of our group, who laid the groundwork for this present discussion.

Chapter 1

Introduction

1.1 Introduction

The relationship between molecular structure and chemical reactivity is inextricably linked to molecular degrees of freedom, which most notably allow for coupling between high- and low-frequency motions. Even simple fluctuations in molecular structure require not only torsional displacements, but also changes in interatomic bond distances and other nuclear degrees of freedom. Approaching molecular motions within the context of the Born-Oppenheimer approximation, the energetic requirements for these processes are largely determined by related changes in the molecule's electronic energies. Interactions between multiple vibrational modes are generally treated via anharmonic coupling, which is ultimately defined by a full, multidimensional potential energy surface (PES). Therefore, it follows that structural fluctuations will inevitably lead to changes in the PES, as shown in **Figure 1.1**.[1,2]

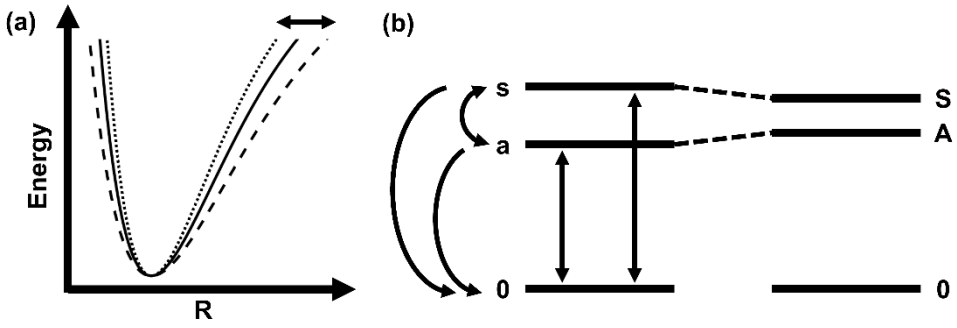

Figure 1.1: Depiction of anharmonic coupling by way of (a) changes in a one-dimensional PES showing the effects of changes in a chemical bond with coordinate R with respect to stretching (dashed line) and compression (dotted line) on an anharmonic oscillator and (b) the motional narrowing of two excited states due to anharmonic coupling. Adapted from sources.[1,2]

When considering anything but the simplest molecules, we cannot readily access the entire 3N-6-dimensional PES; however, we may potentially make measurements that directly correspond to the anharmonic coupling between modes. With insight into the nature of relevant reaction coordinates and transition states, we can focus our attention directly on modes that correspond exact molecular motion, or we can investigate these processes indirectly by addressing modes that are coupled to the relevant degrees of freedom. Two-dimensional infrared (2D-IR) spectroscopy, which we will discuss at greater length in section **1.3**, can be informative due to its ability to measure the transfer of energy between vibrational modes directly or to detect frequency fluctuations that arise from molecular flexibility. Both of these dynamical phenomena occur via anharmonic coupling between high-frequency, spectroscopically-visible degrees of freedom and low-frequency, chemically-relevant degrees of freedom.

Within ultrafast spectroscopy, there is a notable history of measuring the intramolecular vibrational redistribution (IVR) of a system either directly in the time domain or indirectly through its signatures in the frequency domain. Such frequency-domain signatures of IVR are well-established theoretically as a result of anharmonic coupling between modes and the density of states in the system's environment. Furthermore, due to coupling between modes, they are known to occur at frequency difference of the two coupled vibrational states. Recent work from our group has found a correlation between the low-frequency density of states as determined by Kerr effect spectroscopy and the IVR rate constants measured with 2D-IR.[3] Furthermore, in alcohol solvent environments, where hydrogen bonding from the solvent can directly interfere with the vibrational energies of a ligand, we have found a correlation between the solute-solvent hydrogen

bond formation and solvent-dependent IVR timescales.[4] Conversely, we have also employed 2D-IR to investigate molecular flexibility via the influence that low-frequency structural fluctuations exert on high-frequency, spectroscopically visible transitions. In both a simple “piano-stool” complex and a series of diiron hydrogenase active site mimics, we have observed spectral diffusion in nonpolar solvent environments arising from structural fluctuations and not from direct solvation dynamics.[5,6] Molecular flexibility and “loose” chemical coordination have become increasingly pertinent to the pursuit of understanding established catalytic processes and developing new catalysts—which are often defined by a second coordination sphere consisting of changes in ligand structure separate from direct interaction with an active metal site.[7,8]

With molecular flexibility and second-sphere coordination in mind, this dissertation seeks to shift focus to a dynamical phenomenon that has thus far not been thoroughly studied in molecular systems—namely, we aim to investigate the coherence that arises among impulsively excited vibrational states. When a short pulse, whose bandwidth is sufficiently broad enough to span multiple excited states, interacts with a molecule, transient oscillations are known to appear in both pump-probe and 2D spectroscopy.[9–12] These oscillations—which are often called quantum beats—can simply reflect the information obtained via linear absorption spectroscopy; however, vibrational, or vibronic, quantum beats may also correspond to non-equilibrium excited state dynamics that result from optical excitations that may lead to photochemical reactions of structural isomerization. These cases of vibronic coherence, therefore, may sometimes be linked to the structural dynamics proceeding from a photoexcitation and its potential chemical reactions. In 2D-IR spectroscopy, however, we rarely expect significant structural

changes to a molecule as a direct result of exciting vibrational modes, and the quantum beats that arise within 2D-IR experiments usually correspond directly to the frequency differences predicted by the linear infrared spectrum of the molecule. The perturbation theory that underlies the interpretation of 2D spectra makes prescribed predictions about how coherences arise and evolve in time-dependent spectroscopy experiments, and a more complete descriptions of those predictions is presented in section **1.4**. Several years ago, our group found that, when analyzed in great detail, it is possible for coherent oscillations of 2D peak features to appear that cannot be explained by the most common theoretical description and its assumptions. From earlier work on simple metal carbonyls, which found more subtle deviations from the established norm to more recent studies of diiron dithiolate hexacarbonyl complexes, which found significant deviations from the theoretical assumptions, we see consistent dynamical pathways in a range of metal carbonyl systems that must be explained via coherence transfer—where $\rho_{ab} \rightarrow \rho_{cd}$. Coherence transfer, which is most often ignored in theoretical treatments of nonlinear spectroscopy, was also precluded in the original formulation of Redfield theory, where Redfield himself disregarded anything but simple decoherence—where $\rho_{ab} \rightarrow 0$—as a possibility. This so-called “secular approximation” is the foundation for the widely-used ideas of longitudinal (population) and transverse (coherence) relaxation in nuclear magnetic resonance spectroscopy as well as the optical Bloch equations. The actual mechanism of coherence transfer entails the coupling of two high-frequency degrees of freedom via mutual coupling to a low-frequency degree of freedom, which facilitates the transfer of coherence through a low-energy pathway. This mutual coupling between frequency regimes necessitates that anharmonic coupling underscores any coherence

transfer process. Therefore, by analyzing a series of coordination complexes with identical first coordination spheres and changes in their second coordination sphere, we seek to investigate their propensity for coherence transfer more systematically than has been accomplished before. A complete understanding of these coherence transfer phenomena is dependent upon a dedicated theoretical treatment; however, the data presented here should provide adequate motivation for such theoretical work.

Molecular catalytic systems—both natural and synthetic—have proven remarkably sensitive to the effects of coherence transfer by way of anharmonic coupling and intraband coherences.[11,13–17] Most recently, researchers have found that both vibrational and electronic coherence transfer play a vital role in the biological systems that allow for the conversion of available water and carbon dioxide into breathable oxygen and usable energy with the aid of incident solar energy via photosynthesis.[18–21] Of these photosynthetic systems, the Fenna-Matthews-Olson (FMO) complex and bacterial reaction center have been invaluable in furthering our understanding of photosynthesis as an anharmonically coupled process.[22–24] Using a variety of ultrafast spectroscopic techniques, researchers have been able to elucidate the contributions of coherence transfer to the electronic, vibrational, and vibronic regimes of photosynthetic systems' ultrafast dynamics.[16,25–27]

Conversely, synthetic molecular catalysts, such as diiron hydrogenase active site mimics and other small organometallic complexes are reliable platforms for studying ultrafast dynamics and coherence transfer phenomena in more readily parsed quantum mechanical systems.[2,11,12,14,28] While large biological systems may still be evaluated somewhat simply by way of an exitonic Hamiltonian, the inherent degrees of freedom in

such systems vastly increase the complexity of any spectroscopic interpretation.[16,25,29] Due to this natural complexity, it is a worthwhile endeavor to find and develop model systems that combine the excitonic robustness of a multi-site system while being structurally straightforward enough that their spectroscopic interpretations can be more targeted in scope. Much of the previous work in our group has focused on small, organometallic carbonyl complexes as clear model systems for ultrafast vibrational dynamics and vibrational coherence transfer phenomena in a wide variety of chemical environments due to metal carbonyls' unique and well-documented vibrational characteristics.[6,30–32] More specifically, this work is an extension of previous efforts within the group—completed by Dr. Peter Eckert—pertaining to the ultrafast dynamics, structural fluctuations, and vibrational coherence transfer phenomena of diiron dithiolate hexacarbonyl complexes, which are most often used as air-stable biomimetic stand-ins for the diiron hydrogenase active site.[6,15]

1.2 Metal Carbonyls

Transition metal carbonyl complexes, formed from the addition of carbon monoxides (CO) to transition metal atoms, have been a focal point of organometallic chemistry since the mid-1830s.[33] Their prominence in the broader context of chemistry can be attributed to both their general ease of synthesis as well as their propensity to form coordination complexes with a wide variety of ligands. Spectroscopically, metal carbonyls are valuable because of the otherwise sparse 1800-2150 cm^{-1} region of the infrared spectrum in which they absorb, their high oscillator strengths, and because they are excellent reporters of their electronic environments due to π-backbonding—wherein the valence shell of the metal atom donates electron density back to the π-system of the

CO in addition to the more straightforward dative σ-bond formed covalently between the two moieties, which is shown in **Figure 1.2a**.[34–36] The π-backbonding donation of electron density to the π* antibonding molecular orbital of the CO directly weakens the bond order of the affected CO, thus making its vibrational frequency lower. Because the C≡O bond order is directly correlated to the frequency at which its vibration absorbs light, metal carbonyls in specific environments can be distinguished from one another spectroscopically. This observable relationship is particularly useful when considering the molecular structure and electronic environment of various metal carbonyl complexes. As the bond order of the metal carbonyl CO approaches that of free CO, its vibrational frequency increases to match that of its free counterpart, which is indicated spectroscopically as an increase in vibrational frequency. A structural interpretation of this phenomenon can be attributed to the modulation of π-backbonding between the CO and its metal center by a number of electronic and structural effects; however, the simplest interpretation of the relationship is that π-backbonding and vibrational frequency are inversely proportional, as shown in **Figure 1.2b**.[37–39]

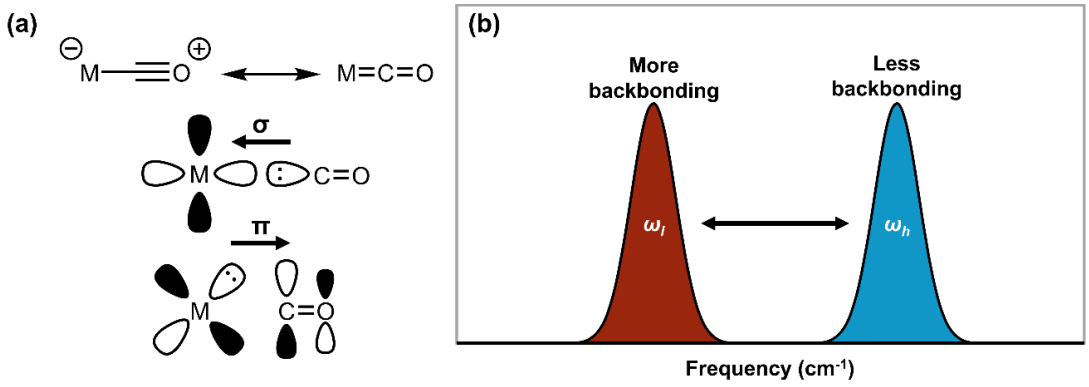

Figure 1.2: (a) Formation of the metal-CO bond in metal carbonyls. (b) Metal carbonyl stretching frequency shifting with respect to the amount of π-backbonding in the metal-CO bond.

1.2.1 Dicobalt Hexacarbonyl Complexes

Among metal carbonyls, alkynyl dicobalt hexacarbonyl (DCHC) complexes are excellent candidates for in-depth study with respect to vibrational coherence transfer due to their synthetic versatility and structural similarity to diiron dithiolate hexacarbonyl complexes, which experience significant intraband coherences and notable coherence transfer via anharmonic coupling.[15] Both DCHC and diiron dithiolate complexes are first-row bimetallic transition metal complexes that contain synthetically tunable bridging ligands. In both cases, the bridging ligands lend the molecules a tetrahedrane-like shape, as shown in **Figure 1.3**; however, the central moiety of the diiron dithiolate complex is markedly less rigid due to the lack of a direct bond between the two sulfur atoms as opposed to the alkyne ligand of DCHC. The haptic bonds anchoring the alkyne ligand of the DCHC complex are coordinated in an η^2-η^2 formation in which the π-systems of the C≡C bond overlap with the valence shell of the cobalt atoms. Therefore, the cobalt-carbon bonds of DCHC share much of their electronic nature with the π-backbonding traditionally associated with transition metal carbonyl bonds.[40] This series of haptic bonds grants much greater electron delocalization between the alkyne ligand, metal centers, and metal carbonyls of the complex—all of which allows the ligand to influence the electronic environment of the metal carbonyls much more directly than in the diiron dithiolate complex. The difference in the orientation of the bridging ligand between the complexes is also significant—while the ligand of the diiron dithiolate complex extends vertically away from the diiron carbonyl structure, the ligand of the alkyne DCHC complex extends laterally along an axis perpendicular to the cobalt-cobalt bond.[41] This difference in bonding allows for more direct steric interference between the ligand and the DCHC

moiety, which affects the molecule's typical C_{2v} symmetry group when bonded to larger and more sterically-intrusive ligands.[42]

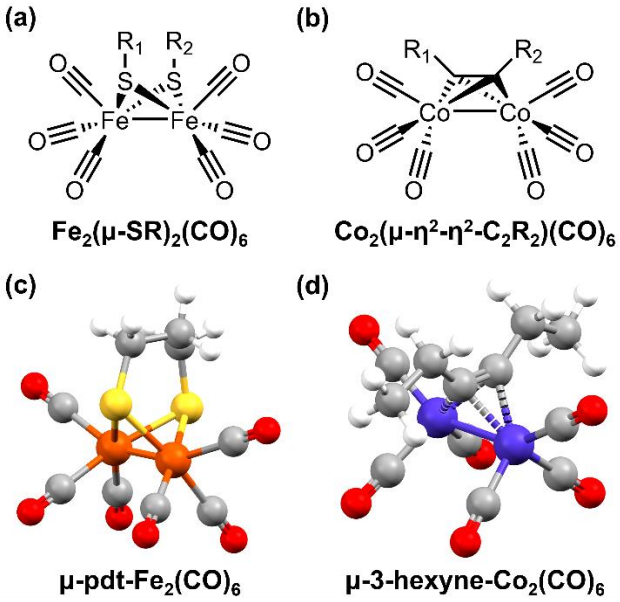

Figure 1.3: Structures of generic (a) μ-dithiolate diiron hexacarbonyl and (b) μ-η2-η2-alkynyl dicobalt hexacarbonyl complexes respectively, alongside computed structures of (c) μ-propane dithiolate (pdt) diiron hexacarbonyl and (d) μ-η2-η2-3-hexyne-dicobalt hexacarbonyl (3-hex DCHC).

1.2.2 Applications and Synthesis of Dicobalt Hexacarbonyl Complexes

DCHC complexes most notably serve as catalytic intermediates for both the Pauson-Khand reaction (PKR) and the Nicholas reaction, both of which were developed in the late 1970s.[43,44] The PKR entails the formal [2+2+1] cycloaddition reaction of an alkyne, an alkene, and CO to form a regioselective cyclopentenone with the aid of dicobalt octacarbonyl (DCO)—forming the alkynyl DCHC complex as an intermediate species with stoichiometrically quantitative yields.[45] Similarly, the Nicholas reaction employs DCO as a protecting group for the carbon-carbon alkyne bond in a propargylic ether that undergoes nucleophilic substitution in the presence of a Lewis Acid. In both cases, the DCHC moiety is removed through oxidative means either as a matter of fact in the PKR, or as a discrete step in the Nicholas reaction; both reactions are shown in **Figure 1.4**.

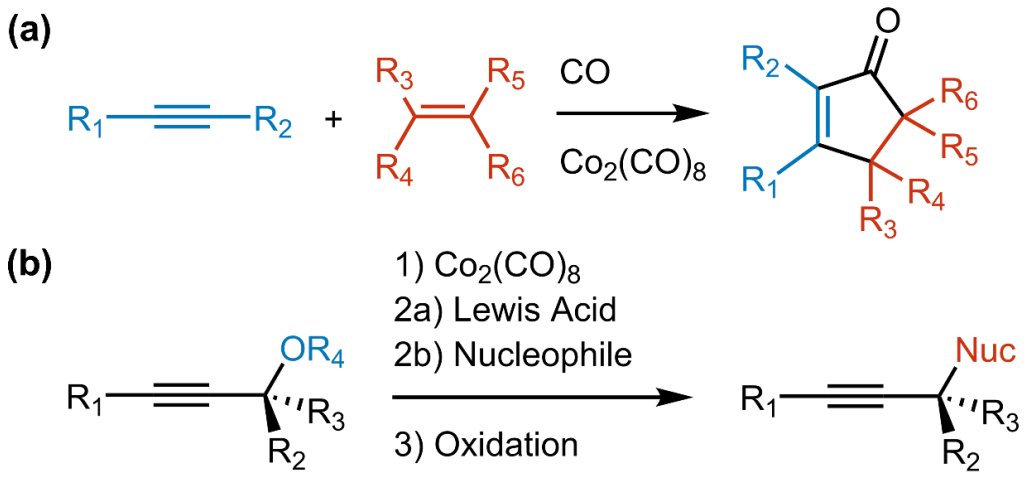

Figure 1.4: (a) Synthetic scheme for the Pauson-Khand reaction, showing the [2+2+1] cycloaddition formation of a cyclopentenone from an alkyne, alkene, and $Co_2(CO)_8$. (b) Synthetic scheme for the Nicholas reaction, showing the $Co_2(CO)_8$ stabilzation of a propargylic ether during nucleophilic substitution.

Previous studies of alkynyl DCHC complexes have focused largely on their versatility as both catalysts and protecting groups; however, more recent work has sought to characterize the complexes themselves due to their robust electrochemical properties as well as their remarkable resilience to both light and air.[45–48] The facile coordination of alkyne ligands to the dicobalt octacarbonyl moiety has given rise to a suite of complexes that are widely useful as catalysts for regioselective chemistry, labile chromophoric tags for bio-orthogonal chemistry, and potential additions to anticancer therapies.[47,49–52] This work focuses on a series of alkyl- and aryl-substituted alkynyl DCHC complexes, shown in **Figure 1.5**, as a tunable model system for investigating vibrational coherence transfer phenomena through the application of two-dimensional infrared spectroscopy (2D-IR). Previous work in our group has investigated the ultrafast dynamics, intraband coherences, and vibrational coherence transfer in DCO, diiron dithiolate hexacarbonyls, and other small metallocarbonyl complexes with multidimensional optical spectroscopy—to which this work stands as an extension.[11,15,31]

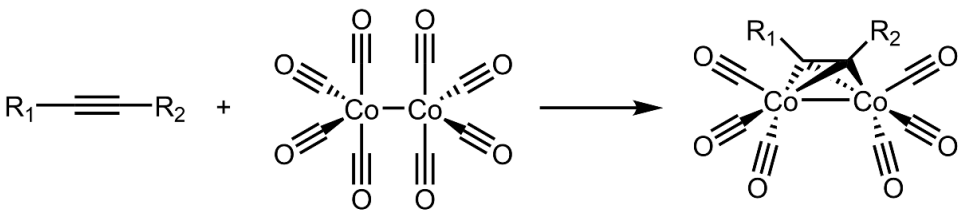

1. **3-Hex: R_1,R_2 = C_2H_5**
2. **TMSi: R_1,R_2 = $Si(CH_3)_3$**
3. **DPhA: R_1,R_2 =C_6H_5**
4. **EtPyr: R_1: Pyrene, R_2 = H**
5. **EtFc: R_1: Ferrocene, R_2 = H**
6. **PhA: R_1 = C_6H_5, R_2 = H**
7. **PhTMSi: R_1: C_6H_5, R_2 = $Si(CH_3)_3$**
8. **1T1H: R_1 = $Si(CH_3)_3$, R_2 = C_4H_9**

Figure 1.5: Synthetic scheme for the formation of alkynyl DCHC complexes with a series of eight alkyne ligands.

1.2.3 Assignment of Vibrational Modes in DCHC

The vibrational modes of DCHC complexes, as with all organometallic complexes, are linear combinations of individual symmetry group transformations determined by the point group of the chosen system and are often evaluated computationally with density functional theory (DFT) calculations.[40,53,54] With metal carbonyls specifically, their relevant vibrational modes can be readily thought of as an n-dimensional matrix wherein the size of the matrix directly corresponds to how many metal carbonyls are present in the chemical system—with each mode representing a different overall transformation. Additionally, each carbonyl mode will recruit any number of the available metal carbonyls to various extents. Thus, a two-carbonyl system such as rhodium dicarbonyl acetylacetonate (RDC) has two metal carbonyl vibrational modes both involving RDC's two metal carbonyls. Meanwhile a six-carbonyl system like DCHC will have six metal carbonyl modes, all of which will perform a different symmetry transformation on the complex's molecular structure.[55] Because each molecular system's normal modes are determined by their symmetry group, it is important to consider molecular symmetry when approaching the assignment of normal modes. RDC belongs to the simplest point group P_1, while the DCHC complexes generally belong to the C_{2v} point group, meaning that the

available transformations will differ between the two systems. Because both DCHC and diiron dithiolate complexes belong to the C_{2v} point group, analogs between the two systems' vibrational modes will naturally arise.

The vibrational modes of all eight DCHC complexes presented in this work were assigned using a combination of DFT calculations and Fourier-transform infrared (FTIR) spectroscopy, as shown in **Figure 1.6** for 3-hex DCHC, which is used as the archetypal example of the DCHC complex. DFT calculations were performed with Gaussian09 using the Becke, 3-parameter, Lee-Yang-Parr (B3LYP) functional, the 6-311+G(d,p) basis set

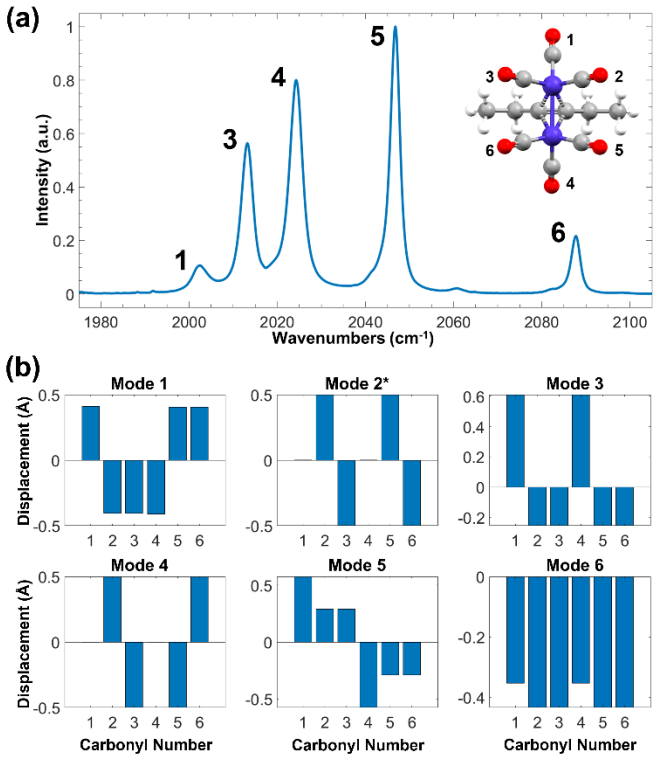

Figure 1.6: (a) FTIR spectrum of 3-hex DCHC in n-heptane with computationally assigned vibrational modes for each peak and each carbonyl assigned a number 1-6. (b) Normalized displacements (in Å) of each carbonyl C≡O bond per mode, including mode 2*, which is not spectroscopically visible.

for all main group atoms, and the Los Alamos National Laboratory 2 Double-Zeta (LanL2DZ) basis set as a pseudopotential for transition metal atoms, which agrees with literature precedent for calculations for metal carbonyl complexes.[56,57] While the specific

assignment of modes varies among the eight DCHC complexes in this work, all eight species exhibit similarities befitting their similar structures. In all cases, the highest frequency mode (mode 6) is a fully symmetric stretch of all six C≡O bonds. Furthermore, all eight complexes share similar behaviors among carbonyls 1 and 4 (hereafter referred to as axial carbonyls) and carbonyls 2, 3, 5, and 6 (hereafter referred to as equatorial carbonyls). Finally, all eight species exhibit two distinct groups of carbonyls each consisting of one axial carbonyl and two equatorial carbonyls centered about a singular cobalt atom, which are grouped as carbonyls 1-3 (group A) and carbonyls 4-6 (group B). In this way, we can separate the vibrational modes along the Co-Co internuclear axis, which is the focal point of the established symmetry axes of the C_{2v} point group for the DCHC complexes.

For 3-hex DCHC specifically, the lowest frequency mode (mode **1**, at 2002 cm^{-1}) is an out-of-phase and antisymmetric stretch, meaning that carbonyl groups A and B are moving in opposite directions while the axial and equatorial carbonyls in each group are moving opposite of each other. Predictably, this mode does not perturb the dipole of the molecule significantly, leading to a small oscillator strength in the observed FTIR spectrum. Mode **2** is an in-phase rocking motion with minimal axial contribution and is predicted by DFT to be very weak, and therefore does not appear on the FTIR spectrum; however, it may be convolved with mode 1 due to their near degeneracy. Mode **3** (at 2013 cm^{-1}) is an out-of-phase symmetric stretch, with groups A and B moving in unison, but the axial and equatorial components are opposed to one another. Mode **4** (at 2024 cm^{-1}) is an antisymmetric rocking motion with some similarities to mode **2**; however, its equatorial contributions are opposed to one another in each group, leading to greater perturbation

of the dipole moment. Mode **5** (at 2047 cm^{-1}) is the highest-intensity peak with an in-phase antisymmetric stretch, where groups A and B are opposed, but the axial and equatorial contributions are in-phase. Finally, as discussed, mode **6** (at 2088 cm^{-1}) is the highest-frequency mode and is a fully symmetric stretch of all six carbonyls. Because this work focuses on DCHC complexes in nonpolar solvent environments, there is clear separation of all five visible modes with sharp spectral features; however, in a more polar environment, the spectral convolution of modes occurs as line shapes broaden due to differences in the solvent environments surrounding the metal carbonyls.[4,58]

It is important to note that through the introduction of ligands, it is both possible and likely to break the C_{2v} symmetry of the DCHC complexes along either of their symmetry axes. Regardless, because all eight complexes preserve the dicobalt hexacarbonyl moiety itself, discussions of all complexes' vibrational modes can be approximated to C_{2v} symmetry.[59]

1.3 Two-Dimensional Infrared Spectroscopy

While metal carbonyl complexes like DCHC are excellent infrared chromophores due to their aforementioned photophysical properties, the wealth of information contained in their spectra cannot be accessed through traditional linear spectroscopy methods. Rather, the use of higher-order multidimensional optical spectroscopy is required to fully elucidate the complexities of metal carbonyls' vibrational modes. To this end, we used 2D-IR spectroscopy in order to overcome the limitations of linear spectroscopy and further investigate our series of DCHC complexes *in situ.*

1.3.1 2D-IR Experimental Apparatus

2D-IR is a third-order nonlinear optical spectroscopy technique performed by overlapping a sequence of ultrashort laser pulses with a sample in both space and time to produce a third-order response. In our experimental apparatus, the pulse sequence, shown in **Figure 1.7**, consists of three mid-infrared (mid-IR) pulses separated by two waiting times.

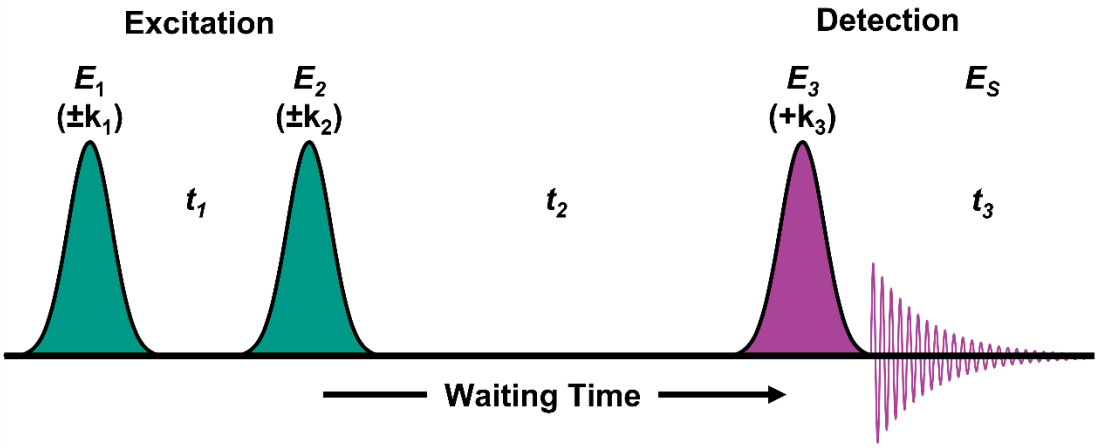

Figure 1.7: Pulse train for 2D-IR experiments showing excitation by the two pump pulses (teal) separated by the coherence time (t_1), the probe pulse (purple) separated by the waiting time (t_2), and the detection of the generated signal E_S.

The 100-femtosecond (fs) pulses are generated in a Ti:sapphire regenerative amplifier at a repetition rate of 1 kHz and are originally centered at 800 nm, as has been reported elsewhere.[60] The 800 nm light is passed through a pair of independent β-barium borate (β-BBO) optical parametric amplifiers (OPAs).[61,62] The output from the OPAs then drives a pair of AgGeS difference frequency generation (DFG) crystals to generate four identical mid-IR pulses at approximately 2025 cm^{-1} with a full-width at half-maximum (FWHM) of approximately 125 cm^{-1}.[63] The fourth pulse—called the local oscillator—passes around the sample and is used to interfere with the generated signal as a phase reference for data processing. The signal and local oscillator are further overlapped with an 800 nm chirped pulse in a 5% MgO-doped $LiNbO_3$ crystal, where sum frequency

generation upconverts the mid-IR signal into visible light such that it can be detected with a charge-coupled device (CCD) spectrometer camera that is synchronized with the 1 kHz repetition rate of the Ti:sapphire amplifier. A diagram of the experimental apparatus is provided in **Figure 1.8**.

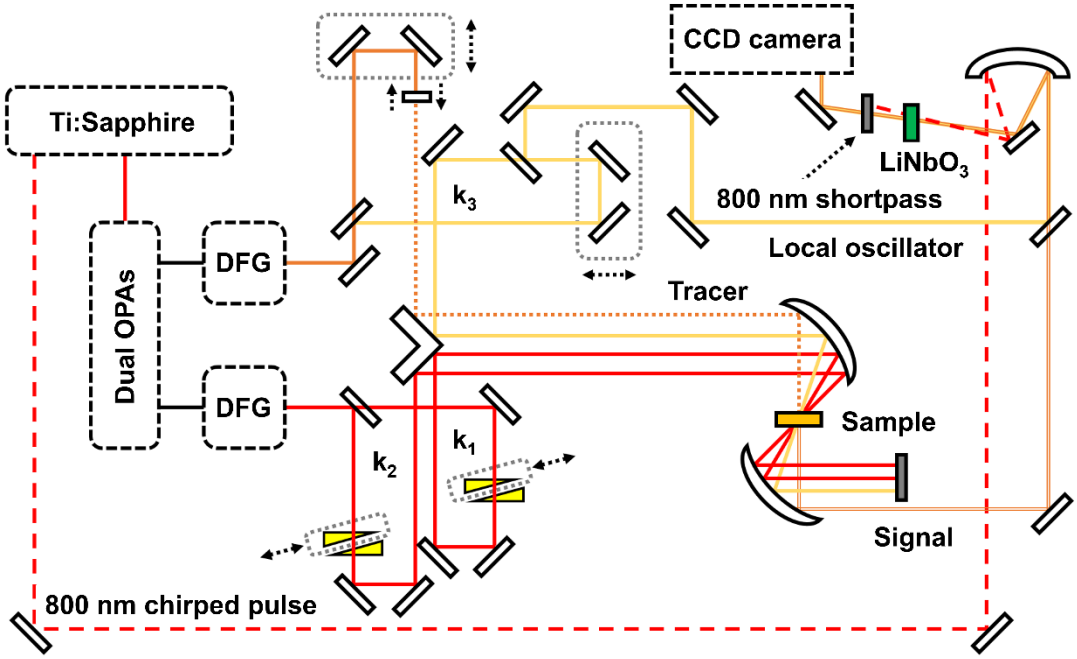

Figure 1.8: Diagram of the 2D-IR experimental apparatus, with OPAs and DFGs simplified for the sake of clarity.

The pulses interacting with the sample can be categorized as two pump pulses (k_1 and k_2) and a probe pulse (k_3) and are overlapped at the sample in a noncollinear geometry shown in **Figure 1.9**. The first waiting time (t_1)— referred to hereafter as the coherence time—occurs between the two pump pulses and is generated by continuously scanning a ZnSe wedge over a time delay of approximately 10 picoseconds (ps). The coherence time is subsequently Fourier-transformed to generate the excitation frequency (ω_1) axis of our 2D spectra. The second waiting time (t_2) occurs between the second pump and the probe pulse and is set at fixed values of t_2 via a delay stage. After generation at the sample, the signal is overlapped with a so-called “local oscillator” that

serves as a reference for the relative phase of the signal vector with respect to the original pump and probe pulses. The signal and local oscillator then overlap with the 800 nm chirped pulse output from the Ti:Sapphire amplifier. The signal is finally collected by a CCD spectrometer that provides the detection axis (ω_3) for our spectra directly.[63]

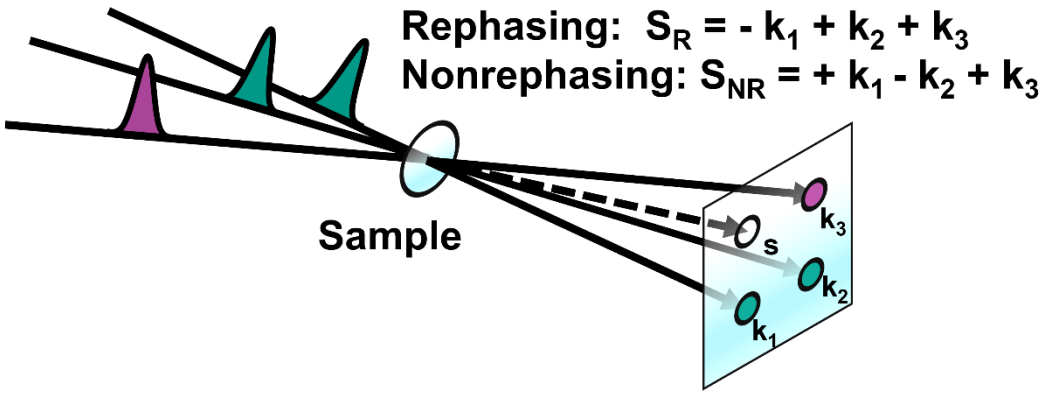

Figure 1.9: Noncollinear geometry used in 2D-IR experiments, denoting rephasing and nonrephasing signals generated by the scanning of the k_1 or k_2 motor, respectively.

Two possible signals may be separately collected by this experimental apparatus depending on which pump pulse is being delayed by scanning its respective ZnSe wedge along a translation stage. When the motor for the k_1 wedge is scanned, a rephasing signal is collected. Conversely, when the motor for the k_2 wedge is scanned, a nonrephasing signal is collected along the same vector. Thus, our 2D-IR experiments are conducted by collecting 2D spectra for both the rephasing and nonrephasing signals at a series of chosen points along t_2.

1.3.2 Third-Order Response and Double-sided Feynman Diagrams

Because 2D-IR is third-order nonlinear spectroscopy, the signal it generates follows the third order of nonlinear response. In contrast to FTIR, wherein both excitation and detection arise from a single light-matter interaction, the excitation and detection of 2D-IR arise from three independent light-matter interactions that happen in sequence.

For each of these interactions, the occurring pulse acts on the sample's vibrational modes by creating either a vibrational coherence or population depending on where in the sequence the interaction takes place. Using the framework originally employed in photon echo spectroscopy, we can understand these interactions via a series of density matrices, where the time-dependent density of a given state is defined by the time-evolution of the system's Hamiltonian, shown as,[64]

$$\rho(t) = \rho + (i\hbar)^{-1} \int_0^{\tau} [\mathcal{H}(t), \rho(t)] dt = \sum_n^{\infty} \rho^{(n)}(t) \tag{1.1}$$

Where, for a single wavefunction ψ, the density of states is given by,

$$\rho_{nm} \equiv |\psi_n\rangle\langle\psi_m| = \sum_{n,m} c_n c_m^* |n\rangle\langle m| \tag{1.2}$$

For a two-level system, the binary operator results in a 2×2 density matrix, yielding values for vibrational populations on the matrix diagonal and vibrational coherences on the off-diagonal. Visualizing this alongside a series of three pulses allows us to visualize each discrete step, as shown in **Figure 1.10**.[65]

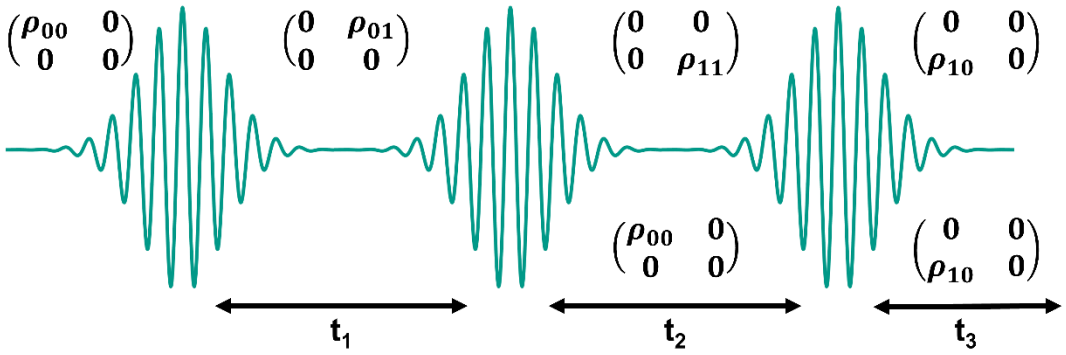

Figure 1.10: Density matrix representation of the light-matter interactions in third-order spectroscopy, with populations occurring on the matrix diagonal (where n = m) and coherences on the off-diagonal (where n ≠ m).

With each interaction, one side of the system is acted upon to create vibrational coherences during t_1 and t_3 and a vibrational population during t_2. During each waiting time, the system evolves and dephases until the next pulse, at which point it is acted upon once again. While all three waiting times involve dephasing, the system experiences dephasing and population relaxation during t_2. The result of all three interactions is a third-order polarization of the system dipole such that,

$$P^{(3)}(t_3, t_2, t_1) \propto \int_0^\infty dt_3 \int_0^\infty dt_2 \int_0^\infty dt_1 \sum_n \begin{pmatrix} R^{(3)}(t_3, t_2, t_1) E_3(t - t_3) \cdot \dots \\ E_2(t - t_2 - t_3) E_1(t - t_3 - t_2 - t_1) \end{pmatrix} \quad (1.3)$$

Where $R^{(3)}$ is given by,

$$R^{(3)}(t_3, t_2, t_1) = \left(-\frac{i}{\hbar}\right)^3 \left\langle \Big[\Big[[\mu(t_3 + t_2 + t_1), \mu(t_2 + t_1)]\mu(t_1)\Big]\mu(0)\Big] \right\rangle \quad (1.4)$$

While t_n represents the waiting time between the $(n-1)^{th}$ interaction and the nth interaction, and μ is the system's dipole moment at each respective time point.[66,67] The total number of possible pathways increases exponentially with the order of the system response, which becomes intractable rather quickly as the number of oscillators increases.[68] For the sake of simplicity, we will consider a three-mode, three-level system consisting of mode **a'** (in red), mode **a** (in orange) and mode **s** (in teal), their overtones

(**2a'**, **2a**, and **2s** respectively), and their combination bands (**aa'**, **sa'**, and **sa** in purple), as shown in **Figure 1.11**.

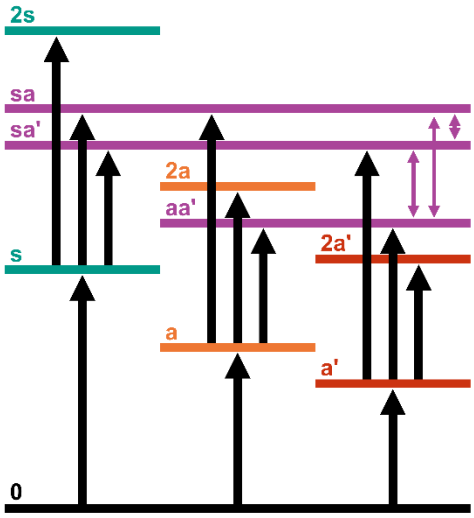

Figure 1.11: Three-mode, three-level system consisting of mode **a'** (in red), mode **a** (in orange), and mode **s** (in teal), their overtones, and combination bands (in purple) originating from a common ground state.

To better visualize these possibilities, we use double-sided Feynman diagrams of the Liouville pathways associated with the rephasing and nonrephasing signals, shown in **Figure 1.12**.[69] Each double-sided Feynman diagram is read starting at the bottom and moving up, where each arrow indicates a discrete light-matter interaction to one side of the quantum mechanical system. Time passes between each interaction, and the system evolves in the indicated state until the next interaction, at which point the system will respond to the new stimulus. This time-evolution framework in Liouville space is identical to the photon echo spectroscopy discussed previously, and it is clear to see that the system evolves in a coherence of states during t_1 and t_3 (ρ_{nm}, where $n \neq m$) while evolving in a population during t_2 (ρ_{nm}, where $n = m$).

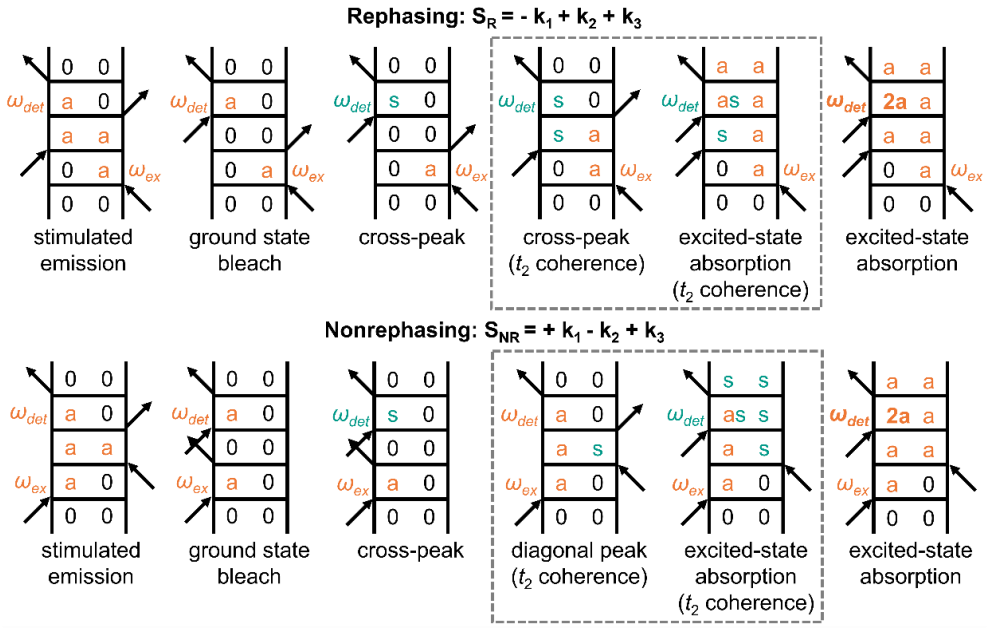

Figure 1.12: Double-sided Feynman diagrams representing six of the eight possible Liouville pathways both the rephasing and nonrephasing signals. For clarity, Dirac notation about each component has been omitted.

An important feature of the double-sided Feynman diagram approach is the ability to directly map pathways in Liouville space onto a real 2D-IR spectrum programmatically. Because the three interactions with the system correspond to the three pulses that generate each 2D-IR spectrum at a given t_2, each peak in a 2D spectrum may be understood as either the result of an individual pathway or the combination of multiple pathways.[63,70] This facile interpretation allows for a tremendous amount of information to be accessed quite readily in a series of 2D spectra.

1.3.3 General Interpretation of 2D-IR spectra

Using the Feynman diagram framework discussed in the previous section, we will once again consider the three-mode system presented in **Figure 1.11**. The linear absorption spectrum of such a system may be represented quite simply as three peaks placed at arbitrary frequencies with respect to their relative energies. The highest frequency mode will be the highest energy mode **s**, with modes **a** and **a'** occurring at

lower frequencies. As discussed in section **1.2.2**, the highest frequency mode is most often a totally symmetric stretch, with in-phase and out-of-phase antisymmetric stretches occurring at lower frequencies, as shown in **Figure 1.13a**. Extending from our discussion of vibrational coherences and populations in 2D-IR, we can readily expand this linear absorption spectrum into a 2D spectrum at an arbitrary waiting time such that $t_2 > 0$, as shown in **Figure 1.13b**. With an excitation frequency axis of ω_1 and a detection frequency axis of ω_3, we recreate the density matrix formalism in the 2D spectrum directly. As in a density matrix, diagonal peaks (along an axis where $\omega_1 = \omega_3$) are formed by excitations and detections at a single frequency while two sets of off-diagonal peaks are formed by excitation and detection at different wavelengths (where $\omega_1 \neq \omega_3$). These crosspeaks can be divided into those above the diagonal ($\omega_1 < \omega_3$) and below the diagonal ($\omega_1 > \omega_3$). Furthermore, because of the separation of the excitation and detection events by t_2, we can say that crosspeaks above the diagonal are initially excited at ω_1 and subsequently

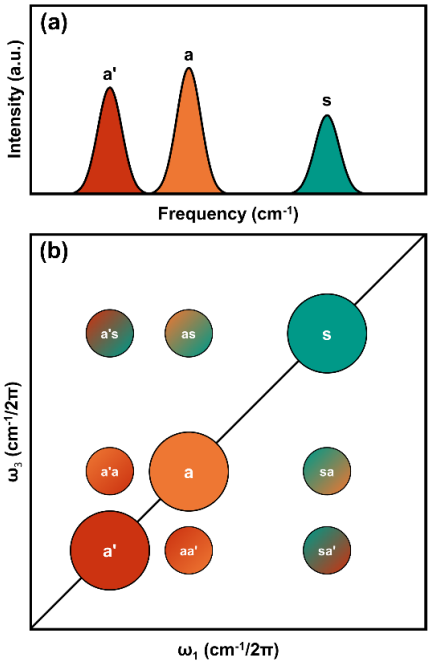

Figure 1.13: Cartoon representations of a three-mode system in (a) a linear absorption spectrum and (b) a 2D spectrum at an arbitrary waiting time such that $t_2 > 0$.

detected at ω_3. Conversely, the opposite holds true for crosspeaks found below the diagonal.

Employing the double-sided Feynman diagrams presented in section **1.3.2**, we can easily assign pathways in Liouville space to individual peaks in the 2D spectrum featured in **Figure 1.13b**. For both rephasing and nonrephasing signals, diagonal peaks and crosspeaks' interpretations align with what has been presented thus far; however, it is important to note that t_2 coherences arise along different pathways in the two signal regimes.[71] These coherences, which are generated alongside the detection pulse k_3, see an excited state population that evolves in time at a difference frequency determined by the two states involved in the coherence. In rephasing spectra, these coherences are found in the crosspeaks. Meanwhile, in nonrephasing spectra, these coherences are found along the diagonal. In both cases, the t_2 coherence generates an oscillation in the amplitude of the relevant peak where the oscillatory frequency is equal to the difference frequency of the two states and is modulated by a dephasing time τ, such that:

$$A(t_2) \propto e^{i\Delta\omega_{ab}t_2} \cdot e^{-t_2/\tau} \tag{1.5}$$

Where $\Delta\omega_{ab} = \omega_b - \omega_a$, and τ may be experimentally found. It is important to note that although t_2 coherences are quite often present in 2D spectra, they do not contribute to new peaks or spectral features in a traditional analysis of 2D-IR data.[11,12]

1.3.4 Analysis of t_2 coherences in 2D-IR

Because t_2 coherences are found in the peak amplitudes of 2D-IR spectra, it is important for us to turn our attention to the ways in which 2D-IR datasets are often generated and manipulated. In general, the 2D-IR signal can be thought of as a function

of excitation frequency (ω_1), waiting time (t_2), and detection frequency (ω_3). In a standard approach to data analysis, the frequency axes define the bounds of the spectra while t_2 timepoints are used to take slices of those axes to generate a single 2D spectrum at that waiting time. Vibrational dynamics, such as spectral diffusion and intramolecular vibrational redistribution (IVR), are evaluated by taking population slices of individual peaks defined by a region of interest (ROI) and analyzed with respect to the waiting time axis.[6,72] Throughout 2D-IR spectroscopy, we see a loss of correlation between excitation and detection frequencies as waiting time is increased, leading to the broadening of peaks along the anti-diagonal, as shown in **Figure 1.14**. These dynamical features may be attributed to a variety of chemical and physical phenomena; however, the nature of the system's environment plays a vital role in the interpretation of such dynamics, which we will discuss at greater length in **Chapter 4**.

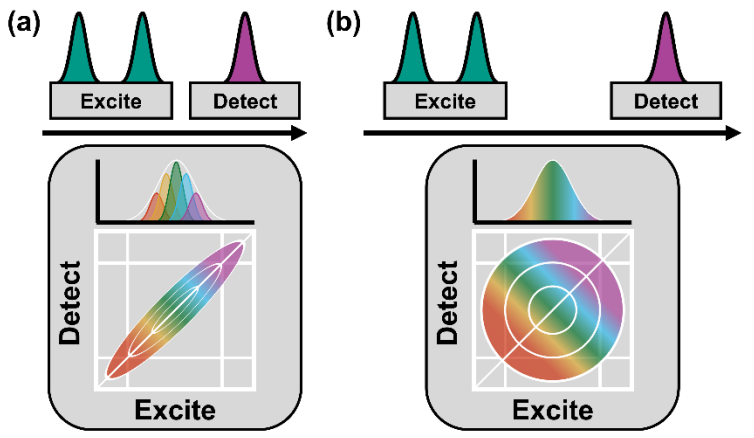

Figure 1.14: Representation of the loss of correlation between excitation and detection frequencies at (a) early waiting times and (b) later waiting times.

Returning to the model 2D spectrum presented in section **1.3.3**, we can evaluate a supposed t_2 coherence at the difference frequency of modes **s** and **a'**. In a rephasing spectrum, this coherence will occur at the crosspeaks of the two modes, represented in **Figure 1.15a** as $\Delta\omega_{sa'}$. Assigning arbitrary values to the vibrational frequencies of the two

modes, we will consider a scenario in which $\Delta\omega_{sa'} = 75\ cm^{-1}$. To evaluate the coherence at the crosspeak, we take a slice of the peak amplitude along t_2, which in this case has been simplified to match **Equation 1.5**. In an actual 2D-IR dataset, the peak amplitude of a rephasing crosspeak would also contain dynamical information pertaining to IVR.[3,4,73] Once an ROI has been established, the population trace along t_2 will show an oscillation of the peak amplitude at the relevant coherence frequency. Fourier transforming along the t_2 axis allows for direct evaluation of the coherence frequency, thus changing the evaluated signal to be a function of three wavelengths: excitation and detection frequencies as defined before, and a new ω_2 axis such that,

$$S(\omega_1, \omega_2, \omega_3) = \int_{-\infty}^{\infty} S(\omega_1, t_2, \omega_3) \cdot e^{-2\pi i \omega t} dt_2 \tag{1.6}$$

Where the Fourier transform of the original signal in the ROI causes the oscillation in time to be represented as a single peak in the frequency domain, as shown in **Figure 1.15b** and **1.15c**.

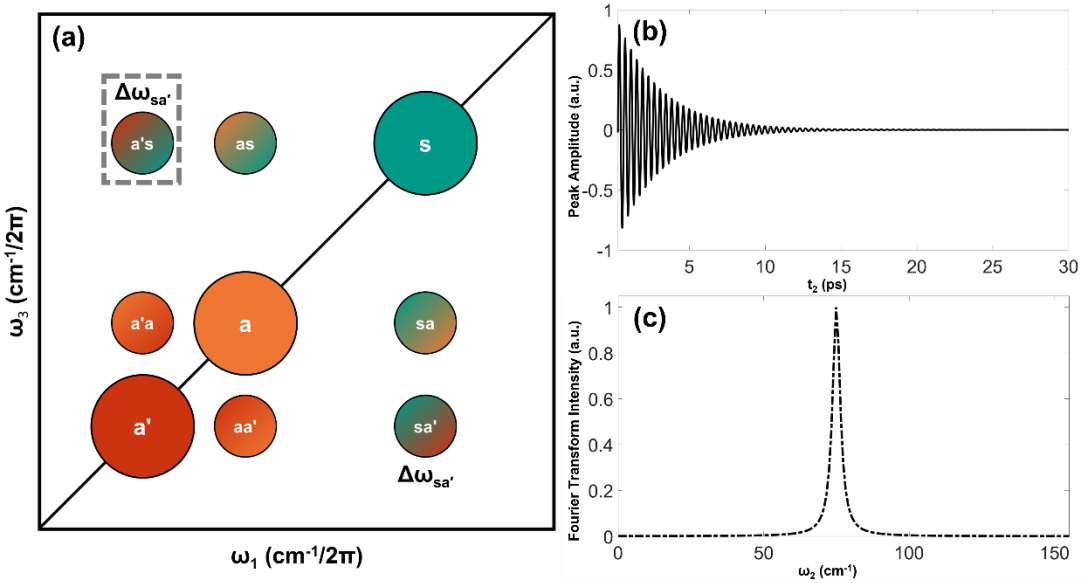

Figure 1.15: Cartoon of (a) a 2D-IR spectrum of a three-mode system with a region of interest drawn around the upper crosspeak of modes **s** and **a'**, (b) a t_2 slice of the peak amplitude oscillating at $\Delta\omega_{sa'}$, and (c) the Fourier-transformation of the oscillation at $\Delta\omega_{sa'}$.

Due to the secular approximation of Redfield theory, which serves as the undergirding framework for much of ultrafast spectroscopy, we assume that each t_2 coherence will experience only one set of oscillations; however, there are notable cases in which that approximation breaks down, that of vibrational coherence transfer being the most relevant to the present work.[15,74,75]

1.4 Redfield Theory

Developed by Alfred G. Redfield in 1965, the eponymous Redfield equation is a perturbation theory approach for understanding relaxation processes in systems of coupled oscillations.[76] Within the context of the density operator formalism for 2D-IR discussed in section **1.3.2**, Redfield theory is a foundational component in answering questions of vibrational dynamics and intraband coupling in 2D-IR.[65] Where, assuming that the interactions between states are minimal, the Redfield equation may be stated as the second-order perturbation of a system's Hamiltonian, given by the following expression:

$$\frac{\partial \sigma_{nm}(t)}{\partial t} = -i\omega_{nm}(t)\sigma_{nm}(t) + \sum_{n,m,j,k} \Gamma_{nm,jm}\sigma_{jm}(t) \tag{1.7}$$

Where σ_{nm} is the reduced density matrix and is defined by a time-dependent frequency difference of states n and m, such that $\omega_{nm} = \omega_n - \omega_m$, and a relaxation superoperator, Γ, that entails the fluctuation of external field interactions with the perturbed Hamiltonian of the relevant system. A derivation of the general Redfield equation is given in **Appendix A.1**.

1.4.1 The Secular Approximation

In general, ultrafast spectroscopy applications of Redfield theory fall under the so-called secular approximation, which Redfield proposed alongside the theory's first formulation. Under this approximation, several assumptions are held to be true: First, secular terms evolve such that their perturbation does not largely affect the wavefunction of the system unless it directly connects eigenstates with the same relative energy—meaning that energy differences between eigenstates must be smaller than the perturbations themselves.[76] Second, for a relaxation within a system pertaining to states α, α', β, and β', the density matrix of these states will be unperturbed by the relaxation itself, such that,

$$R_{\alpha\alpha'\beta\beta'} \ll |\alpha - \alpha' - \beta + \beta'| \tag{1.8}$$

Meaning that all nonsecular perturbations may be either included or ignored without any real detriment to the characterization of the system's Hamiltonian. Lastly, for any coherence state ρ_{nm} where $n \neq m$, the coherence will invariably evolve to zero, while a population state ρ_{nn} may exchange energy with a state ρ_{mm} according to an established reaction rate. These assumptions, therefore, remove considerations of energy transfer between disparate coherences as well as those between coherences and populations. These coherence transfer events, therefore, fall outside of the standard assumptions through which we typically interpret ultrafast spectroscopy. Despite this deviation from the established norm, coherence transfer has proven to be a consistent feature of systems strongly affected by anharmonic coupling and are readily found in coupled oscillators by way of intraband coherences.[11,12,15]

1.4.2 Coherence Transfer

Coherence transfer within the context of ultrafast vibrational dynamics has been previously described at length within the context of both simulated and experimental data.[2,11,15,77] Previous work by Khalil and coworkers focused on the apparent coherence transfer found in RDC, which was originally attributed to bath modes anharmonically coupled to the vibrational modes of the metal carbonyl moiety.[2] While later efforts by Marroux and coworkers as well as Pakoulev and coworkers provided alternative explanations of spectral features, the framework of anharmonically coupled coherence transfer remains the common interpretation.[12,74] Previous work in our group has focused on experimental and *ab initio* treatments of the coherence transfer processes in DMDC. In the initial findings, Nee and coworkers found that crosspeaks in the experimental results for DMDC showed oscillations at more than one difference frequency, which was later investigated computationally by Baiz and coworkers.[11,77] The *ab initio* calculations for DMDC were performed with the possibility of coherence transfer in mind and thus included nonsecular terms in the system's anharmonic Hamiltonian. This computational supplement to the original experimental data attributed the additional quantum beat frequency to nonsecular coherence transfer pathways. Additional work in our group focused on diiron dithiolate hexacarbonyl complexes and found significant evidence for coherence transfer via anharmonic coupling to low-frequency torsional modes in the metal carbonyl moiety.[15]

By employing the density operator formalism and double-sided Feynman diagrams, we can effectively visualize both intraband coherences and coherence transfer events. Occurring within signal pathways that are known to evolve according to t_2

coherences as outlined in section **1.3.2**, coherence transfer may be observed in oscillations that do not share the frequency of the expected combination band. Returning to the three-mode system described in section **1.3.4**, we will now consider a coherence between mode **s** and mode **a**—the t_2 coherence for which would normally arise as shown in **Figure 1.16a**. By allowing for coherence transfer, however, it may be possible to observe a convolution of the intraband coherences for the **sa** and **sa'** combination bands via the pathway shown in **Figure 1.16c**. Additionally, by treating the system as a 4×4 density matrix of the three modes and their shared ground state, we can chart the coherences as they are formed, as shown in **Figure 1.16b,d**.

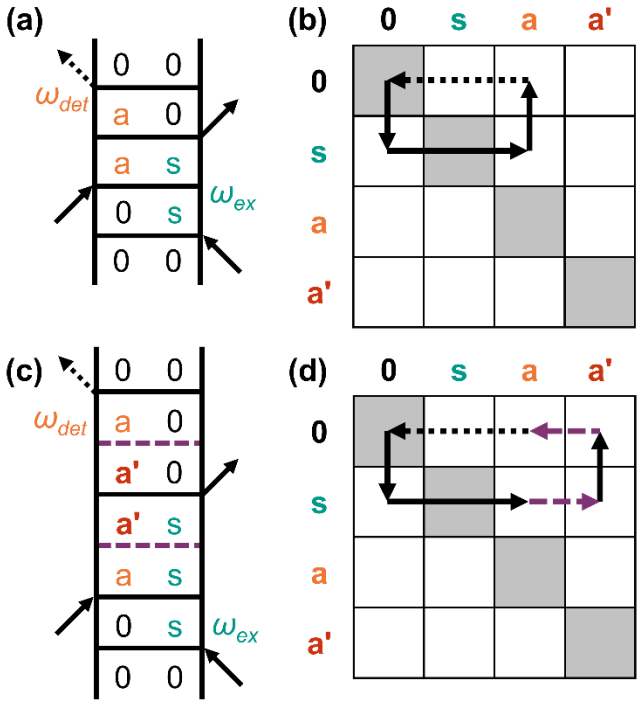

Figure 1.16: (a) Double-sided Feynman diagram for the rephasing crosspeak of mode **a** and mode **s** via t_2 coherence, and (b) a density matrix representation of that same crosspeak. (c) Double-sided Feynman diagram of that same crosspeak with a coherence-to-coherence transfer between mode **a** and mode **a'**, and (d) a density matrix showing the pathway of the coherence transfer event.

Starting from the ρ_{00} ground state population, the first interaction with the system generates the coherence ρ_{0s} that then evolves over t_1 as previously described. The

second interaction forms the coherence ρ_{as} that evolves over t_2. Within the bounds of the secular approximation the system remains largely unchanged until the third interaction, which forms the coherence ρ_{a0} that subsequently relaxes to the ground state population, ρ_{00}. Alternatively, if we allow the system to evolve in such a way that coherence transfer is possible—meaning that nonsecular terms are included in the Redfield equation—coherence-to-coherence transfer may arise such that the ρ_{as} coherence can evolve into the $\rho_{a's}$ coherence during t_2. This coherence transfer will then cause the peak amplitude to oscillate not at the ω_{as} difference frequency, but rather at the $\omega_{a's}$ difference frequency; however, because detection still occurs at ω_a rather than $\omega_{a'}$, the resulting crosspeak will appear in its normal place in the 2D spectrum. The proof of this coherence transfer, therefore, will be limited to the population amplitude oscillations discussed in section **1.3.4**. If coherence transfer is occurring for a set of modes, the difference frequencies of the involved modes will be apparent in ω_2 alongside the expected frequency. Furthermore, by including nonsecular terms, it is also possible for coherence-to-population and population-to-coherence transfer events to occur in addition to the coherence-to-coherence transfer events—all of which stand in opposition to the generally held assumptions underlying ultrafast dynamics.

1.5 Outline

The work presented here focuses primarily on discussions pertaining to the propensity for coherence transfer found in a series of alkyl- and aryl-substituted alkynyl DCHC complexes in nonpolar solvent environments.

Chapter 2 will discuss the synthesis, characterization, and ultrafast spectroscopy of the alkyl-substituted species 3-hexyne-DCHC, bis(trimethylsilyl)acetylene-DCHC, and

1-trimethylsilyl-1-hexyne-DCHC with respect to their intraband coherences and coherence transfer.

Chapter 3 will discuss the synthesis, characterization, and ultrafast spectroscopy of the aryl-substituted species diphenylacetylene-DCHC, ethynylpyrene-DCHC, ethynylferrocene-DCHC, phenylacetylene-DCHC, and 1-phenyl-2-trimethylsilyl-acetylene-DCHC with respect to their intraband coherences and coherence transfer.

Chapter 4 will discuss the ultrafast dynamics of 3-hexyne-DCHC, bis(trimethylsilyl)acetylene-DCHC, and ethynylpyrene-DCHC in both heptane and dodecane, comparing their behavior in the two solvents.

Chapter 5 will summarize the presented work and discuss future directions for this project with respect to potential ligands and potential sample matrices.

Chapter 2

Alkyl-Substituted Dicobalt Hexacarbonyl Complexes as a Platform for Investigating Vibrational Coherence Transfer

2.1 Introduction

Catalytic cycles have long been the focus of significant scientific effort, both in harnessing their usefulness as well as understanding the mechanisms by which they occur. For this reason, it is important to turn our attention toward natural catalytic and enzymatic reactions to understand the ways in which they have evolved since life first arose on our planet billions of years ago. Of these biological reactions, few are as crucial to our continued existence as photosynthesis—the process through which incident sunlight is used for the efficient conversion of atmospheric carbon dioxide into oxygen and usable energy in the form of carbohydrates.[78,79] In recent years, photosynthetic reaction centers are strongly influenced by the process of coherence transfer via anharmonic coupling between the electronic and vibrational regimes of both the Fenna-Matthews-Olson (FMO) complex and the bacterial reaction center.[16,17] Unfortunately, due to the complexity of the chemical structures involved, these advancements have come at the cost of significant effort and computational investment. Therefore, to better understand coherence transfer as a process, it is imperative that suitable model systems be developed and investigated.

By taking an excitonic approach to their Hamiltonians, these large biological systems may be effectively understood in terms that are very similar to those of small molecules.[58] Although the inherent degrees of freedom vary drastically between the two types of systems, their underlying behaviors are governed by the same principles. Therefore, a thorough understanding of vibrational dynamics and coherence transfer in a small model system will enrich our understanding of those processes in much larger systems.

For many years, metal carbonyl complexes have been used as facile infrared probes due to their relatively bright oscillator strengths and the otherwise sparsely populated region of the infrared spectrum that they inhabit. Complexes such as rhodium dicarbonyl acetylacetonate (RDC) and dimanganese decacarbonyl (DMDC) have been used as excellent model systems for studying coupled oscillators in a variety of environments.[12,58,70,74] RDC has been particularly useful as a model due to the simplicity of its vibrational modes and has been used to elucidate the ways in which intraband coherences can be characterized with two-dimensional infrared spectroscopy (2D-IR). Similarly, DMDC has proven to be a useful model system for understanding more complicated vibrational systems and the ultrafast dynamics that arise within them.

Although RDC and DMDC are excellent systems for understanding ultrafast vibrational dynamics, they are both quite limited in their ability to be used for more nuanced investigations of the relationships between molecular structure, electronic structure, and vibrational dynamics due to their simplicity. Therefore, finding synthetically versatile platforms to use as model systems is of vital importance. Previous work in our group has focused on a series of diiron dithiolate hexacarbonyl complexes that serve as

biomimetic stand-ins for the diiron hydrogenase active site.[6] These diiron hexacarbonyl complexes, we found, were spectroscopically sensitive to both anharmonic coupling as well as coherence transfer.[15] Furthermore, by changing the dithiolate ligand on the diiron hexacarbonyl moiety, we found that the ultrafast vibrational dynamics were somewhat tunable depending on the affixed ligand.

In seeking to expand our understanding of coherence transfer as a phenomenon, we turned to alkynyl dicobalt hexacarbonyl (DCHC) complexes. First employed as catalytic intermediates and protecting groups, alkynyl DCHC complexes have since been used as IR chromophores and chemical tags.[46,50,80] Proceeding from a click chemistry-like reaction involving stoichiometric amounts of dicobalt octacarbonyl and an alkyne ligand, DCHC complexes have proven to be a synthetically tunable platform for understanding vibrational coherence transfer.[43,45,81] Unlike the diiron dithiolate hexacarbonyls previously studied in our group, the haptic coordination of the alkyne to the dicobalt moiety allows for more direct electronic overlap between the ligand and the metal carbonyls themselves, which will be discussed at greater length in **Chapter 3**.

2.2 Experimental Methods

For this work, three alkyl-substituted alkynyl DCHC complexes were synthesized using methods established by Happ and coworkers in the early 1990s.[45] All reagents were purchased from Sigma Aldrich and used without further modification or preparation. For all three reactions, stoichiometric amounts of dicobalt octacarbonyl (~3 mmol) were mixed with the respective ligand (3-hexyne, bis(trimethylsilyl)acetylene, and 1-trimethylsilyl-1-hexyne) in approximately 30 mL of *n*-pentane and left to stir overnight at room

temperature (~20°C). The solvent bath was then removed *in vacuo* before purification. Reaction products were purified via column chromatography using a mobile phase consisting of an 80%:20% mixture of petroleum ether and dichloromethane (v/v) and a silica gel stationary phase. Products were collected as a single dark reddish-brown band, as reported elsewhere.[82] Remaining solvent was then removed *in vacuo*, yielding a reddish-brown product. Both 3-hexyne (3-hex) DCHC and bis(trimethylsilyl)acetylene (TMSi) DCHC formed dark reddish-brown crystals, while 1-trimethylsilyl-1-hexyne (1T1H) DCHC formed a dark reddish-brown oil. Each reaction was performed under positive nitrogen pressure and red-light conditions to prevent degradation of the dicobalt octacarbonyl during the course of the reaction. All three complexes, their structures shown alongside their linear absorption spectra in *n*-heptane in **Figure 2.1**, were synthesized in quantitative yields as expected.

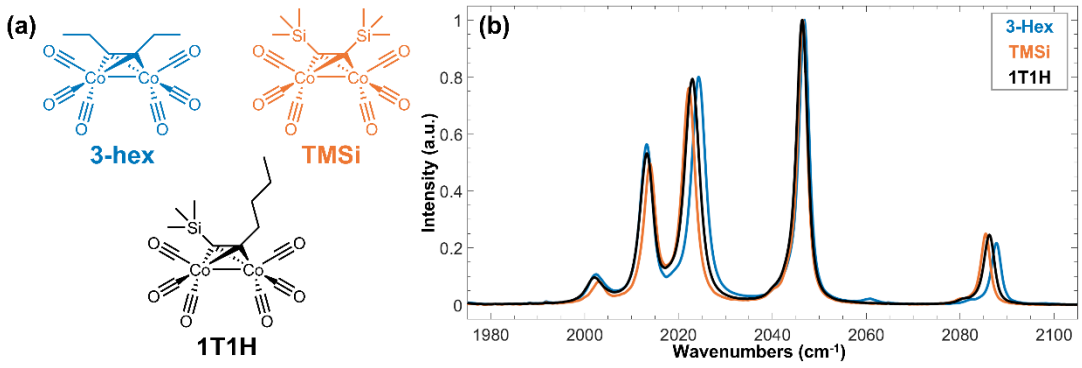

Figure 2.1: (a) Structures of the 3-hex, TMSi, and 1T1H DCHC complexes, and (b) linear absorption spectra of their metal carbonyl stretching modes in n-heptane.

Two-dimensional infrared (2D-IR) spectroscopy experiments were performed using the apparatus described in section **1.3.1**. Absolute value rephasing and nonrephasing 2D-IR spectra were collected along a series of time points between -0.5 and 35 ps, with fine sampling over the first 5 picoseconds and more sparse sampling out

to 35 picoseconds. These time points were developed with Dr. Peter Eckert's work on diiron dithiolate hexacarbonyls in mind. Additionally, the final waiting time was truncated to 35 picoseconds, which more than accounted for the vibrational lifetimes of the carbonyl modes in a nonpolar solvent, which will be discussed further in **Chapter 4**. Once collected, the absolute value 2D spectra were interpolated along evenly-spaced t_2 points starting at 0.15 picoseconds and Fourier transformed to produce a series of coherence maps with respect to ω_2. This transformation of the data yields frequency-domain interpretations of peak amplitudes as discussed in section **1.3.4** and is well-documented in the analysis of intraband coherences in 2D electronic and 2D-IR spectroscopies.[2,14,74] The coherence maps presented in this work are, therefore, representations of the 2D-IR signal in terms of $S(\omega_1, \omega_2, \omega_3)$, with specified slices of ω_2 projected onto the ω_1 and ω_3 axes.

2.3 Results

Absolute value rephasing and nonrephasing spectra of these DCHC complexes provide insights into the intraband coherences of their vibrational coherences and populations respectively, as discussed in section **1.3.3**. For the sake of clarity, the vibrational modes of each complex will be referred to as modes **1** through **6**, starting from the low frequency mode and counting toward the high frequency mode, as in section **1.2.3**. All three complexes are predicted by DFT to have both modes **1** and **2** convolved under the same peak, due to the degeneracy or near degeneracy of the vibrational modes involved. For the sake of this discussion, however, we will focus on modes **3** through **6**, which span a region of approximately 2013 cm^{-1} to 2088 cm^{-1}. All discussions of crosspeaks will similarly take place in the same framework, where the mode **3** to mode **6** crosspeak (hereafter referred to as crosspeak **3**,**6**) will correspond to excitation at mode

3 (2014 cm^{-1} for 3-hex-DCHC) and detection at mode **6** (2088 cm^{-1} for 3-hex-DCHC). A full assignment of modes for the rephasing 2D spectrum of 3-hex-DCHC is shown in **Figure 2.2** as a guide for further discussion.

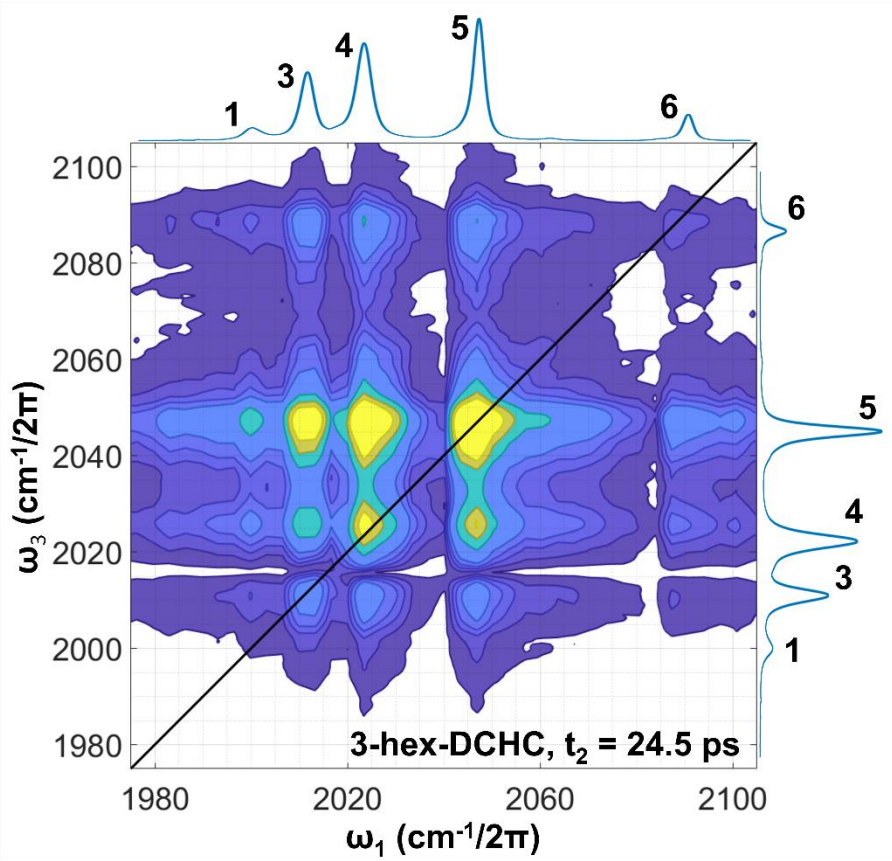

Figure 2.2: Rephasing absolute value 2D-IR spectrum of 3-hex-DCHC in n-heptane with mode assignments and representations of the linear absorption spectrum along each frequency axis.

Rephasing and nonrephasing coherence maps show intensity in ω_2 matched to the ω_1 and ω_3 coordinates at which it arises. As discussed in section **1.3.4**, we expect t_2 coherences to arise in the crosspeaks of rephasing spectra, while we expect t_2 coherences to arise along the diagonal in nonrephasing spectra. Therefore, in the coherence maps, we expect to see ω_2 coherences arise near their respective peaks in an

ω_2 window relevant to the difference frequencies associated therewith. Selected coherence maps for 3-hex-DCHC are presented in **Figure 2.3**.

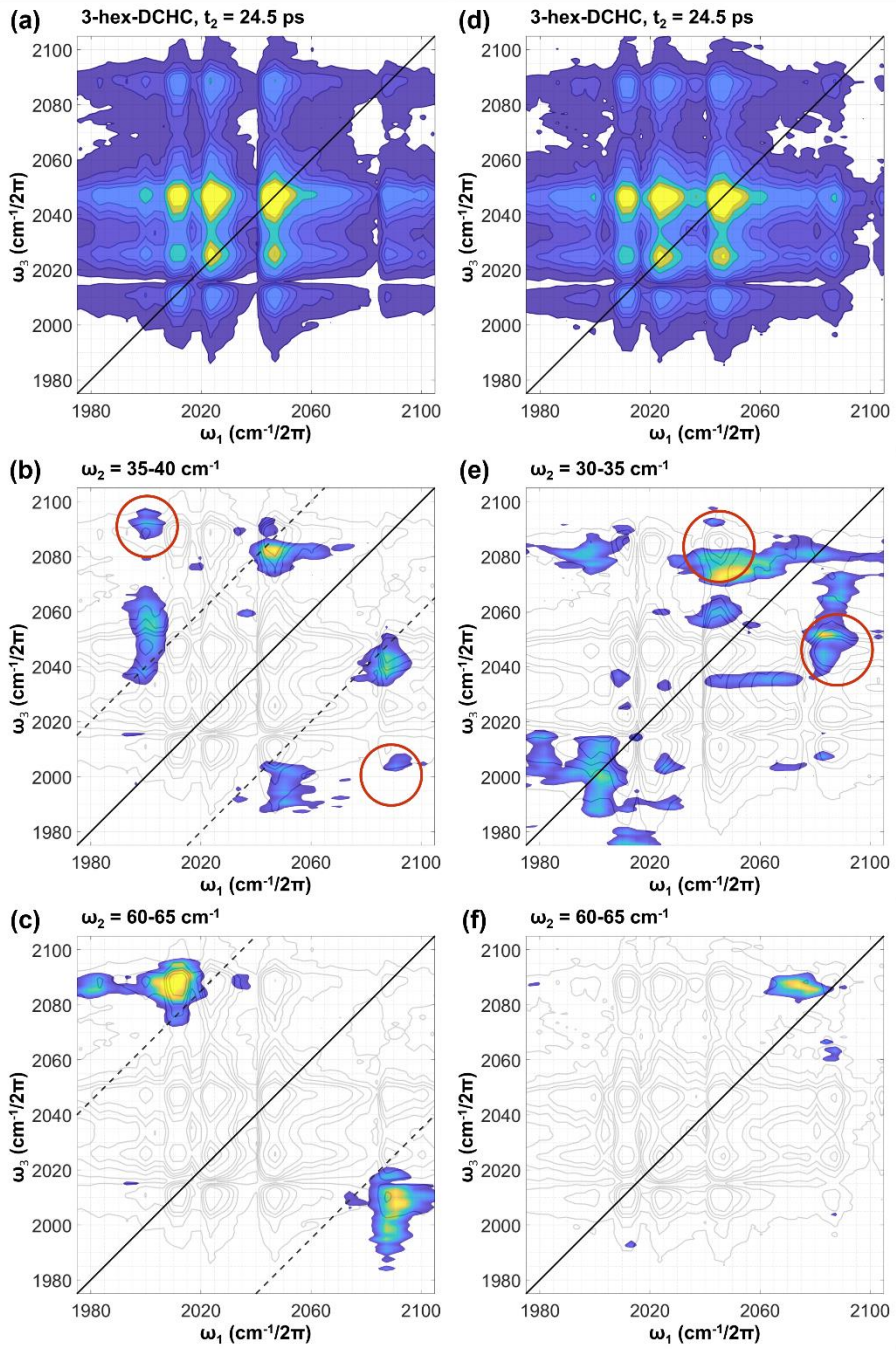

Figure 2.3: 2D-IR data for 3-hex-DCHC including (a) rephasing absolute value 2D-IR spectrum, (b) rephasing coherence map at ω_2 = 35-40 cm^{-1}, (c) rephasing coherence map at ω_2 = 60-65 cm^{-1}, (d) nonrephasing absolute value 2D-IR spectrum, (e) nonrephasing coherence map at ω_2 = 30-35 cm^{-1}, and (f) nonrephasing coherence map at ω_2 = 60-65 cm^{-1}. Dotted lines have been added to show the upper limit of ω_2 for rephasing coherence maps. Red circles denote unexpected ω_2 intensity.

Coherence maps for TMSi-DCHC and 1T1H-DCHC show similar features in both their rephasing and nonrephasing spectra, as shown in **Figure 2.4** and **Figure 2.5,** respectively.

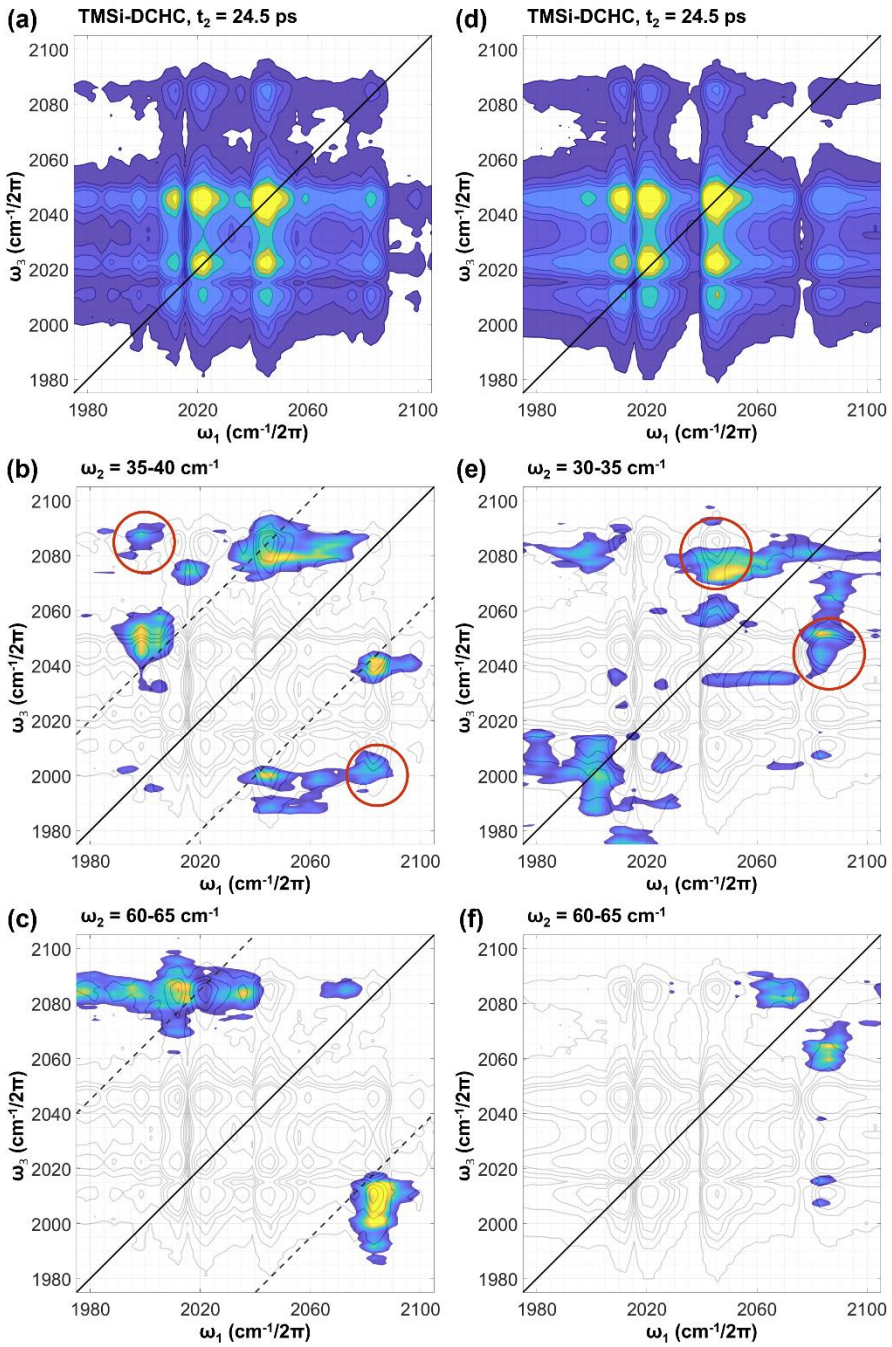

Figure 2.4: 2D-IR data for TMSi-DCHC including (a) rephasing absolute value 2D-IR spectrum, (b) rephasing coherence map at ω_2 = 35-40 cm^{-1}, (c) rephasing coherence map at ω_2 = 60-65 cm^{-1}, (d) nonrephasing absolute value 2D-IR spectrum, (e) nonrephasing coherence map at ω_2 = 30-35 cm^{-1}, and (f) nonrephasing coherence map at ω_2 = 60-65 cm^{-1}. Dotted lines have been added to show the upper limit of ω_2 for rephasing coherence maps. Red circles denote unexpected ω_2 intensities.

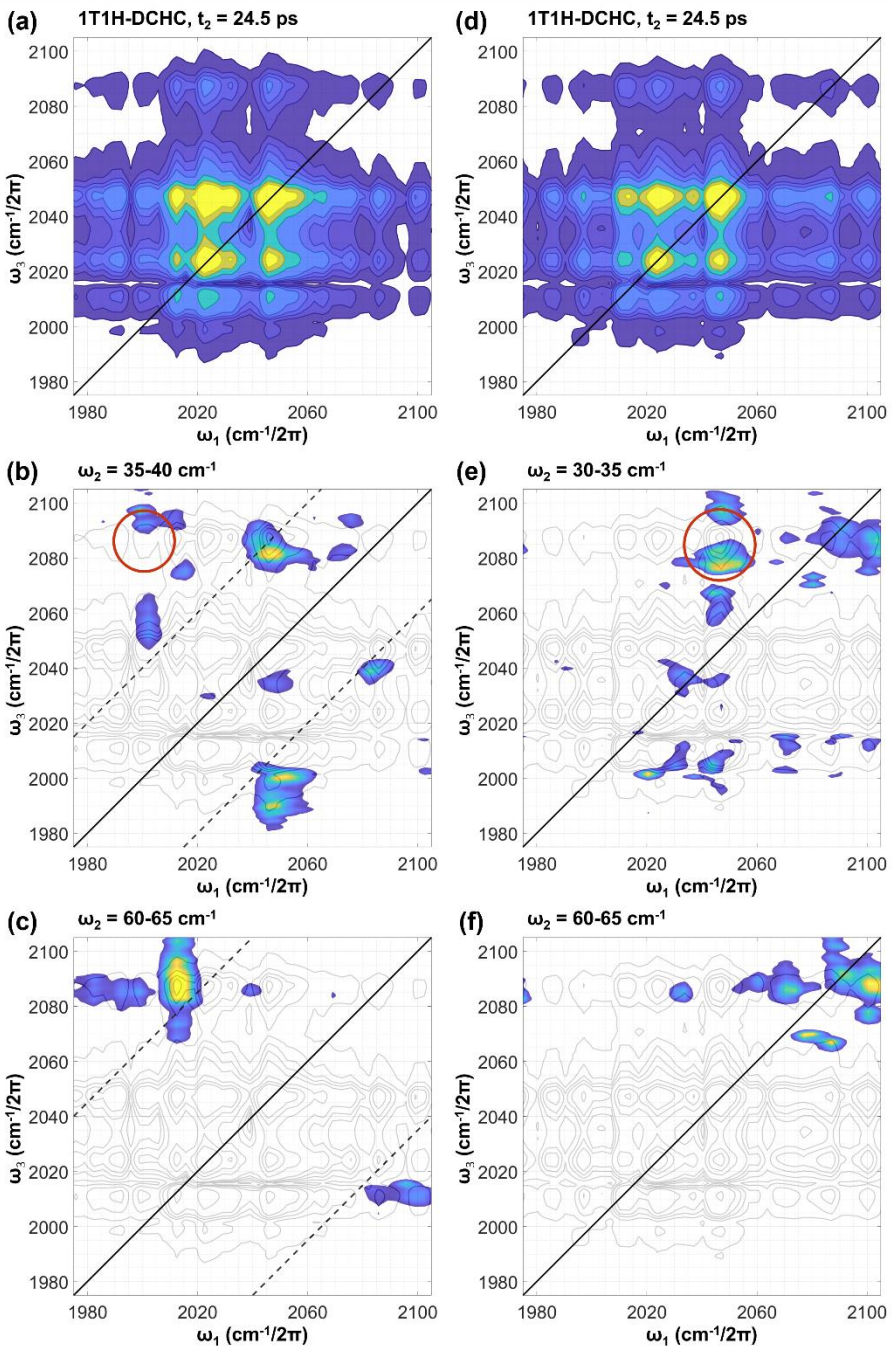

Figure 2.5: 2D-IR data for 1T1H-DCHC including (a) rephasing absolute value 2D-IR spectrum, (b) rephasing coherence map at ω_2 = 35-40 cm^{-1}, (c) rephasing coherence map at ω_2 = 60-65 cm^{-1}, (d) nonrephasing absolute value 2D-IR spectrum, (e) nonrephasing coherence map at ω_2 = 30-35 cm^{-1}, and (f) nonrephasing coherence map at ω_2 = 60-65 cm^{-1}. Dotted lines have been added to show the upper limit of ω_2 for rephasing coherence maps. Red circles denote unexpected ω_2 intensities.

2.4 Discussion

The three alkyl-substituted DCHC complexes, shown in **Figure 2.1a**, were selected to induce varying amounts of steric bulk without much perturbance to the electronic structure of the DCHC moiety. The simplest complex, 3-hex-DCHC, serves as our archetypal case, while TMSi-DCHC and 1T1H-DCHC are used to investigate the direct steric effects of the ligand on coherence transfer, if any. In the process described in section **1.2.3**, vibrational modes were computationally assigned to each complex with DFT (B3LYP/6-311+G(d,p),LanL2DZ) calculations.[56] The modes for 3-hex-DCHC and 1T1H-DCHC, represented by the probability of each carbonyl being displaced, are shown in **Figure 2.6**.

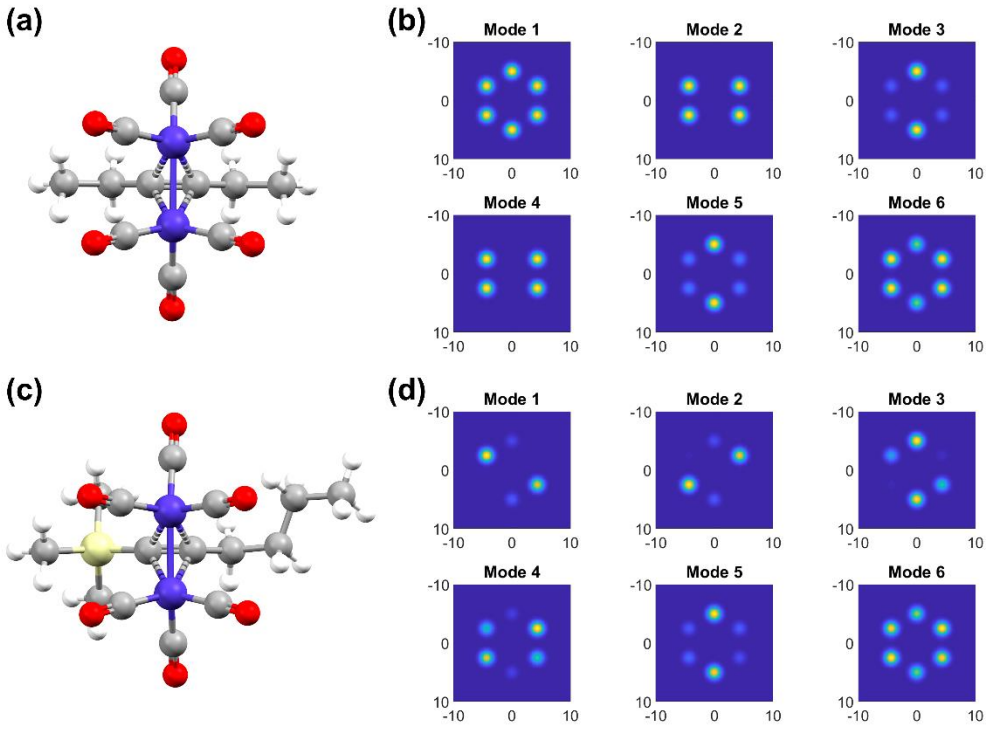

Figure 2.6: (a) Calculated structure and (b) carbonyl displacement probabilities for 3-hex-DCHC as compared to (c) the calculated structure and (d) carbonyl displacement probabilities for 1T1H-DCHC.

From their computationally assigned modes, 3-hex-DCHC and TMSi-DCHC, both of which are symmetrically substituted, share almost all of their modes in common with

the exception of modes **1** and **2**, which have a flipped order in TMSi-DCHC when compared to 3-hex-DCHC. The vibrational modes for 1T1H-DCHC, however, are affected by the asymmetry of its ligand. These differences can be broadly attributed to the difference in steric effects between the ligand's trimethylsilyl moiety and the alkane tail.[83] Even when considered within the context of changes in symmetry, the relative contributions of axial and equatorial carbonyls are equivalent in modes **3** through **6**. Furthermore, the similarities of the complexes' vibrational energies, shown in **Figure 2.1b**, suggest that the electronic nature of the metal carbonyls themselves is unchanged despite these differences in mode symmetry.[40,42]

As expected from their linear absorption spectra, all three complexes experience similar intraband coherences, as indicated in their coherence maps. Further analysis of Fourier transformed peak amplitude oscillations reveals the extent to which these complexes experience coherence transfer. For the rephasing coherence maps pertaining to 35-40 cm^{-1}, ω_2 intensity is expected around crosspeaks **1,5** and **5,1** as well as crosspeaks **5,6** and **6,5** due to their difference frequencies around 40 cm^{-1}; however, intensity arising in crosspeaks **1,6** and **6,1** are unexpected, as denoted by red circles, due to the 86 cm^{-1} difference frequency associated with modes **1** and **6**. For each complex, the coherence maps for 60-65 cm^{-1}, which is relevant to crosspeaks **4,6** and **6,4**, have ω_2 intensity arise instead on the **3,6** and **6,3** crosspeaks. Further investigation of the **3,6** and **6,3** crosspeaks' peak amplitudes reveals a more complete picture of the coherence transfer events occurring in all three complexes, as shown in **Figure 2.7**.

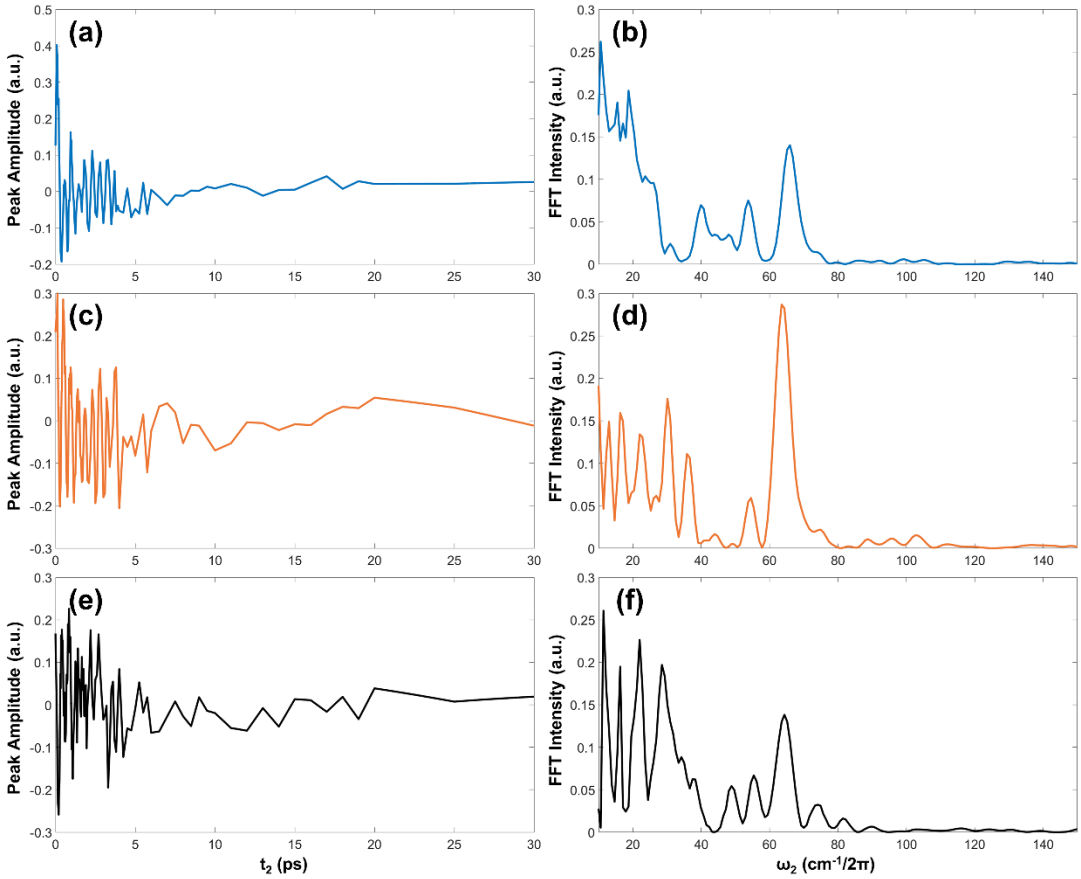

Figure 2.7: Time-domain population slices and frequency-domain Frobenius spectra for the **3,6** crosspeak of (a, b) 3-hex-DCHC, (c, d) TMSi-DCHC, and (e, f) 1T1H-DCHC featuring a prominent spectral feature at 64 cm^{-1}, indicating coherence-to-coherence transfer from **4,6** to **3,6**.

From the Frobenius spectra shown in **Figure 2.7**, it is apparent that crosspeak **3,6** experiences fluctuations other than at its difference frequency of roughly 75 cm^{-1} in all alkyl DCHC complexes, but its most defined oscillation is at the difference frequency associated with crosspeak **4,6**—indicating coherence-to-coherence transfer between the **4,6** and **3,6** t_2 vibrational coherences. For both 3-hex-DCHC and TMSi-DCHC, the broad line shape of the oscillatory feature at 65 cm^{-1} occludes the expected oscillation; however, for 1T1H-DCHC, both oscillations are clearly visible in its Frobenius spectrum.

Looking to the nonrephasing coherence maps presented in **Figures 2.3-2.5**, we find unexpected ω_2 intensity in the **5,6** and **6,5** crosspeaks at 30-35 cm^{-1}. These features

are unexpected for two reasons—first, for systems evolving wholly within the bounds of the secular approximation, we should not observe any oscillations in the crosspeaks of nonrephasing spectra. Furthermore, the difference frequency associated with the **5,6** and **6,5** crosspeaks is 40 cm^{-1}. Instead, the oscillations are red-shifted by roughly 10 cm^{-1}, which corresponds most closely to the difference frequency between mode **3** and mode **5**, occurring at 32-34 cm^{-1} for three complexes. Therefore, it is possible that the observed ω_2 intensity about the **5,6** and **6,5** crosspeaks may be attributed to a coherence transfer event occurring between the vibrational population of mode **5** and the vibrational coherences between the two highest frequency modes in the metal carbonyl system.

In all three alkyl DCHC complexes, the low frequency modes (<100 cm^{-1}) may be attributed to fluxional motion in their overall molecular structure, which has been reported elsewhere and is supported by previous work in our group pertaining to diiron dithiolate hexacarbonyls.[15,40] This collection of low frequency motions is known to contribute to intramolecular vibrational relaxation and spectral diffusion in nonpolar solvent environments.[72] Because of this modulation, the low frequency modes hold the key to further understanding the mechanisms by which the metal carbonyl modes share energy so freely. The low-frequency modes, which account for torsion and other fluctuations in molecular structure, strongly affect the metal carbonyls' positions and relative bond orders via the influence of π-backbonding. These effects are compounded by the haptic bonds formed between the alkyne carbons and the metal carbonyl moiety, which exert similar influence to the metal carbonyl π-backbonding on the electronic structure of the DCHC complexes. Furthermore, DFT calculations of all three alkyl complexes indicate a series of fluxional modes that occur around 40-70 cm^{-1}, which are relevant to the difference

frequencies of the modes in which we find the most evidence for coherence transfer. Therefore, given the context of previous work with diiron dithiolate hexacarbonyl complexes, it is reasonable to assert that the coherence transfer observed in the alkyl-DCHC complexes likely proceeds from a similar anharmonic coupling between the metal carbonyl stretching frequencies and the low-frequency fluxional modes.

2.5 Conclusion

The work presented here gives new experimental data providing experimental evidence that we observe vibrational coherence transfer observed in a series of alkyl-substituted alkynyl-DCHC complexes via 2D-IR spectroscopy. As previously observed in a class of similar diiron dithiolate hexacarbonyl complexes, we find evidence for anharmonically coupled coherence transfer among the metal carbonyl stretching modes. Furthermore, because the appended ligands do not significantly affect the electronic structure of the cobalt carbonyl bonds, this work serves as a direct comparison of moderate intramolecular steric effects on the coherence transfer properties of the alkyl-DCHC complexes, which we have found to be negligible.

Chapter 3

Aryl-Substituted Dicobalt Hexacarbonyl Complexes as an Electronically Tunable Model System for Vibrational Coherence Transfer

3.1 Introduction

For many catalytic systems, including those we find in nature, understanding the relationship between molecular and electronic structure is of utmost importance. From the light-harvesting antennae of photosynthetic complexes to the active sites of enzymes, the relationship between structure and function very often extends beyond the bounds of their molecular geometry and into the realm of their electronic structure.[16,17,25,84] In these large systems, the propensity for anharmonic coupling and coherence transfer necessitates a thorough understanding of every facet of their energetic structures. As the complexity of a system increases, however, the complexity of its analysis increases in tandem—often exponentially so. This scaling problem presents researchers with a series of design challenges centered around the careful selection of both theoretical frameworks and model systems in which to employ those frameworks. In terms of theory, excitonic models are often suited to questions of electronic and vibrational phenomena due to their flexibility in describing a myriad of systems with remarkable efficiency. Conversely, model systems for coherence transfer range in complexity from biological reaction centers dependent upon hundreds of energy levels to small molecules comprised of only a

handful of modes. It is vital, therefore, to find model systems that exist between these extremes of complexity.

Since their development in the late 1970s, alkynyl dicobalt hexacarbonyl (DCHC) complexes have provided a remarkable suite of physically and chemically tunable catalysts for a variety of applications. Expanding from their original roles as catalysts in the formation of regioselective cyclopentenones and protecting groups for nucleophilic replacement in the presence of a Lewis Acid, DCHC complexes have found widespread use in a host of applications ranging from labile bioorthogonal tags to the modulation of photophysical properties in conjugated dyads.[46,50,85] Among DCHC complexes, aryl-substituted complexes exert considerable influence on the electronic and vibrational structure of the DCHC moiety itself due electron delocalization throughout the conjugated system.[40] These electronic effects are shared between the ligand and metal carbonyls, as seen in a series of luminescent pyrene-thiophene dyads and their DCHC complexes, where the adduction of the cobalt carbonyl moiety effectively quenches the fluorescence typically attributed to pyrene.[46]

When compared to complexes containing non-aromatic and alkyl substituted ligands, the vibrational energies of aryl-substituted are noticeably blue-shifted, indicating that the π-backbonding between the cobalt centers and their associated carbonyls is diminished due to the electronic structure of the aryl-alkyne ligand. This electronic overlap between the metal centers and the π system of the haptically bound ligand has been reported in organometallic complexes with similar bonding motifs and is supported by the

calculated molecular orbitals of aryl DCHC complexes, as shown in **Figure 3.1** for ethynylpyrene-DCHC.

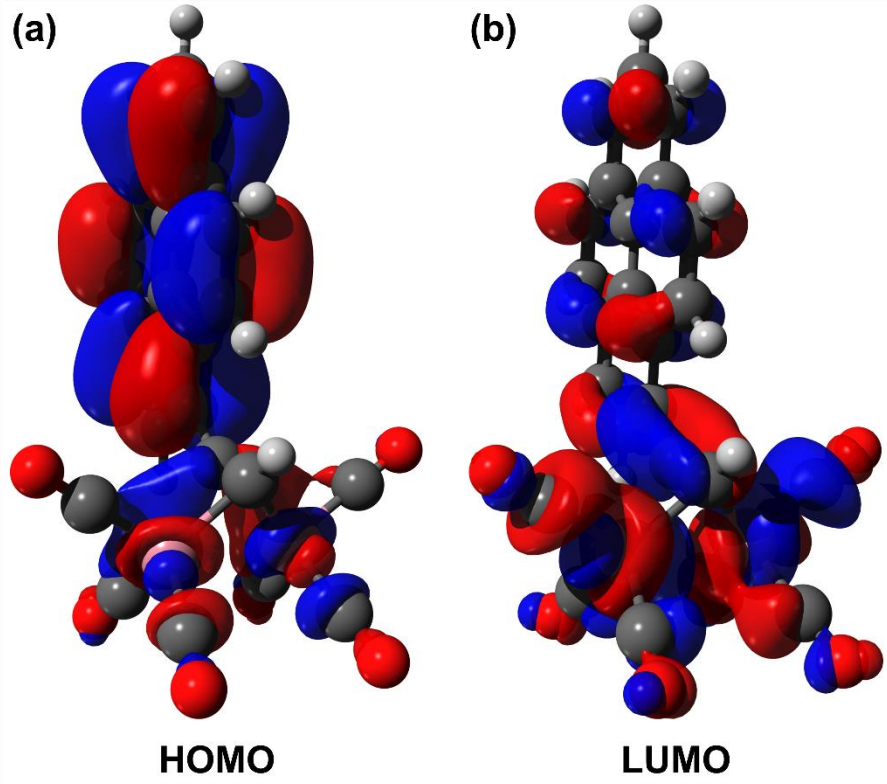

Figure 3.1: Molecular orbitals for ethynylpyrene-DCHC (EtPyr-DCHC) showing (a) the highest occupied molecular orbital (HOMO) and (b) the lowest unoccupied molecular orbital (LUMO) both with significant overlap between the alkyne ligand and the cobalt carbonyl moiety.

3.2 Experimental Methods

For this work, five aryl-substituted alkynyl DCHC complexes were synthesized using well-established methods from the literature.[45,46] All reagents were purchased from Sigma Aldrich and used without further purification or preparation. In each reaction, stoichiometric amounts of dicobalt octacarbonyl (~3 mmol) were mixed with the respective ligand (diphenylacetylene, ethynylpyrene, ethynylferrocene, phenylacetylene, 1-phenyl-2-trimethylsilylacetylene) in approximately 30 mL of *n*-pentane and left to stir overnight at room temperature (~20°C). The solvent bath was then removed *in vacuo* before purification. Reaction products were purified via column chromatography using a

mobile phase consisting of an 80%:20% mixture of petroleum ether and dichloromethane (v/v) and a silica gel stationary phase. Products were collected as a single dark reddish-brown band, as reported elsewhere, except for the ethynylferrocene product, which was dark green.[86] Remaining solvent was then removed *in vacuo*, yielding a dark brown product. Diphenylacetylene (DPhA) DCHC, ethynylpyrene (EtPyr) DCHC, ethynylferrocene (EtFc) DCHC, and 1-phenyl-2-trimethylsilylacetylene (PhTMSi) DCHC formed dark brown to reddish-brown solids, where phenylacetylene (PhA) DCHC formed a dark reddish-brown oil. Each reaction was performed under positive nitrogen pressure and red-light conditions to prevent degradation of the dicobalt octacarbonyl during the course of the reaction. All five complexes, their structures shown alongside their linear absorption spectra in *n*-heptane in **Figure 3.2**, were synthesized with quantitative yields, as expected from previous reports.

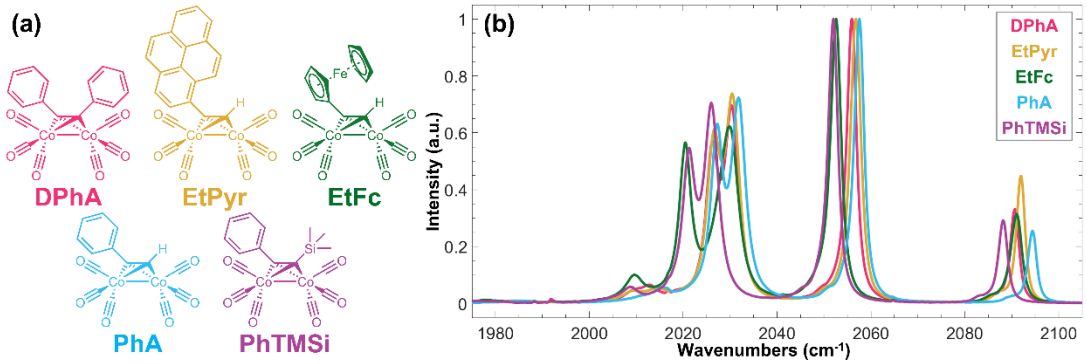

Figure 3.2: (a) Structures of the DPhA, EtPyr, EtFc, PhA, and PhTMSi DCHC complexes, and (b) linear absorption spectra of their metal carbonyl stretching modes in n-heptane.

Two-dimensional infrared (2D-IR) spectroscopy experiments in *n*-heptane were performed according to the method outlined in section **2.2,** using the apparatus described in section **1.3.1**. Coherence maps for interpolated spectra were made using the method described in section **2.2** as well.

3.3 Results

As with the previously discussed alkyl DCHC complexes, the 2D-IR spectra collected for the aryl series focus primarily on the higher frequency modes, which lie between 2020 and 2095 cm^{-1}. Compared to the alkyl series, the aryl DCHC complexes are significantly blue-shifted. Using the same mode assignment convention established in section **1.2.3**, modes **1** through **6** are assigned to their relevant peaks from low frequency to high frequency. Additionally, crosspeaks between modes will be discussed as described in section **2.3**. As a guide for discussion, an absolute value rephasing spectrum of EtPyr-DCHC in *n*-heptane is provided with mode assignments in **Figure 3.3**.

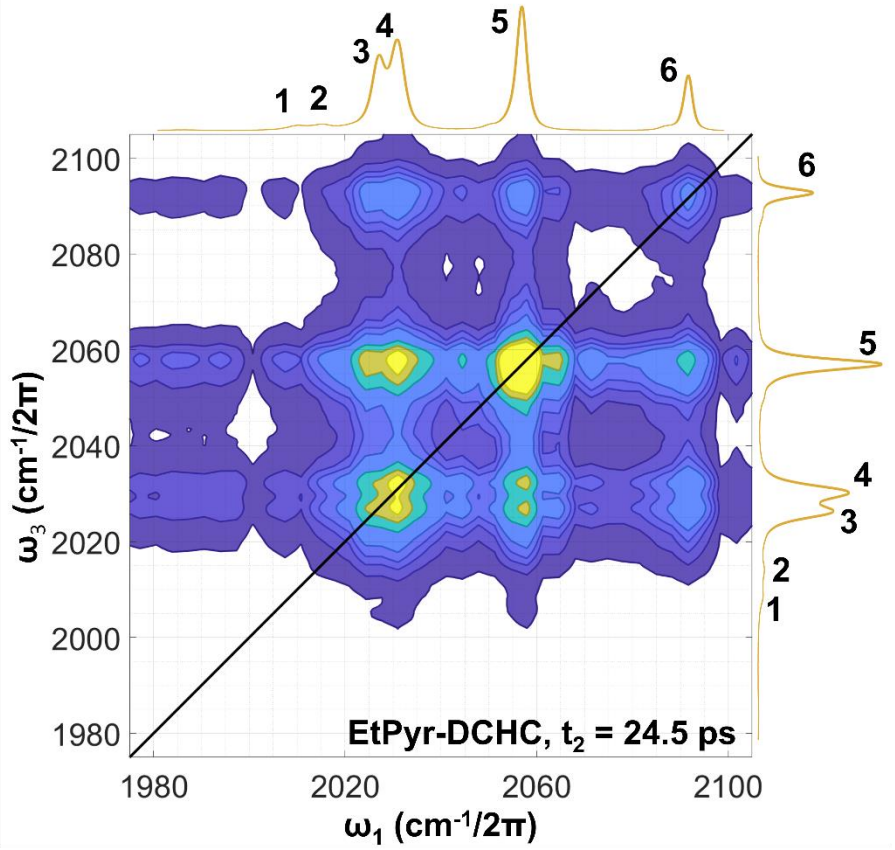

Figure 3.3: Rephasing absolute value 2D-IR spectrum of EtPyr-DCHC in n-heptane with mode assignments and representations of the linear absorption spectrum along each frequency axis.

Selected rephasing and nonrephasing coherence maps are shown for DPhA-DCHC, EtPyr-DCHC, EtFc-DCHC, PhA-DCHC, and PhTMSi-DCHC are shown in **Figures 3.4-3.8**, respectively.

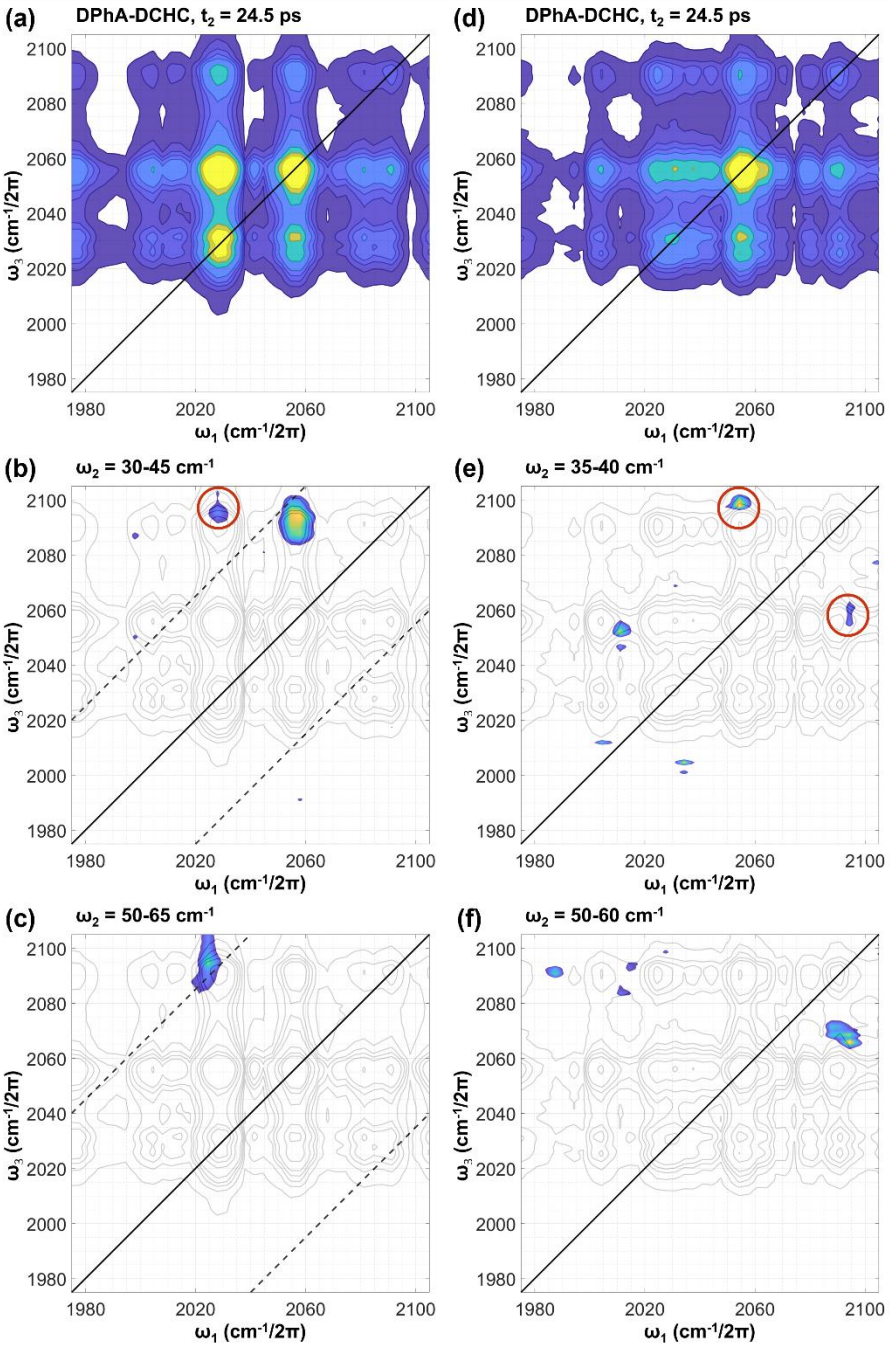

Figure 3.4: 2D-IR data for DPhA-DCHC including (a) rephasing absolute value 2D-IR spectrum, (b) rephasing coherence map at ω_2 = 30-45 cm^{-1}, (c) rephasing coherence map at ω_2 = 50-65 cm^{-1}, (d) nonrephasing absolute value 2D-IR spectrum, (e) nonrephasing coherence map at ω_2 = 35-40 cm^{-1}, and (f) nonrephasing coherence map at ω_2 = 50-60 cm^{-1}. Dotted lines have been added to show the upper limit of ω_2 for rephasing coherence maps. Red circles denote unexpected ω_2 intensities.

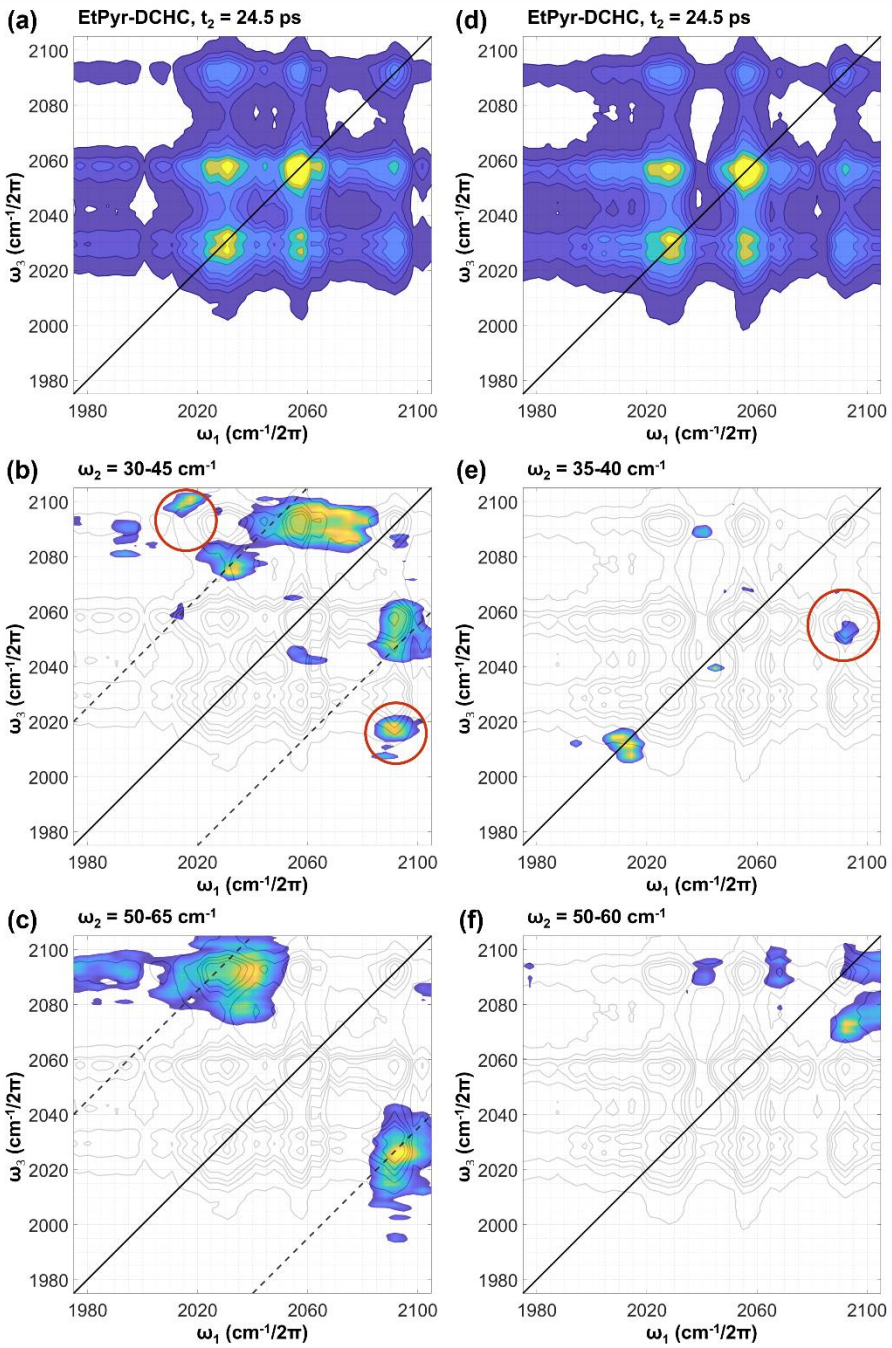

Figure 3.5: 2D-IR data for EtPyr-DCHC including (a) rephasing absolute value 2D-IR spectrum, (b) rephasing coherence map at ω_2 = 30-45 cm^{-1}, (c) rephasing coherence map at ω_2 = 50-65 cm^{-1}, (d) nonrephasing absolute value 2D-IR spectrum, (e) nonrephasing coherence map at ω_2 = 35-40 cm^{-1}, and (f) nonrephasing coherence map at ω_2 = 50-60 cm^{-1}. Dotted lines have been added to show the upper limit of ω_2 for rephasing coherence maps. Red circles denote unexpected ω_2 intensities.

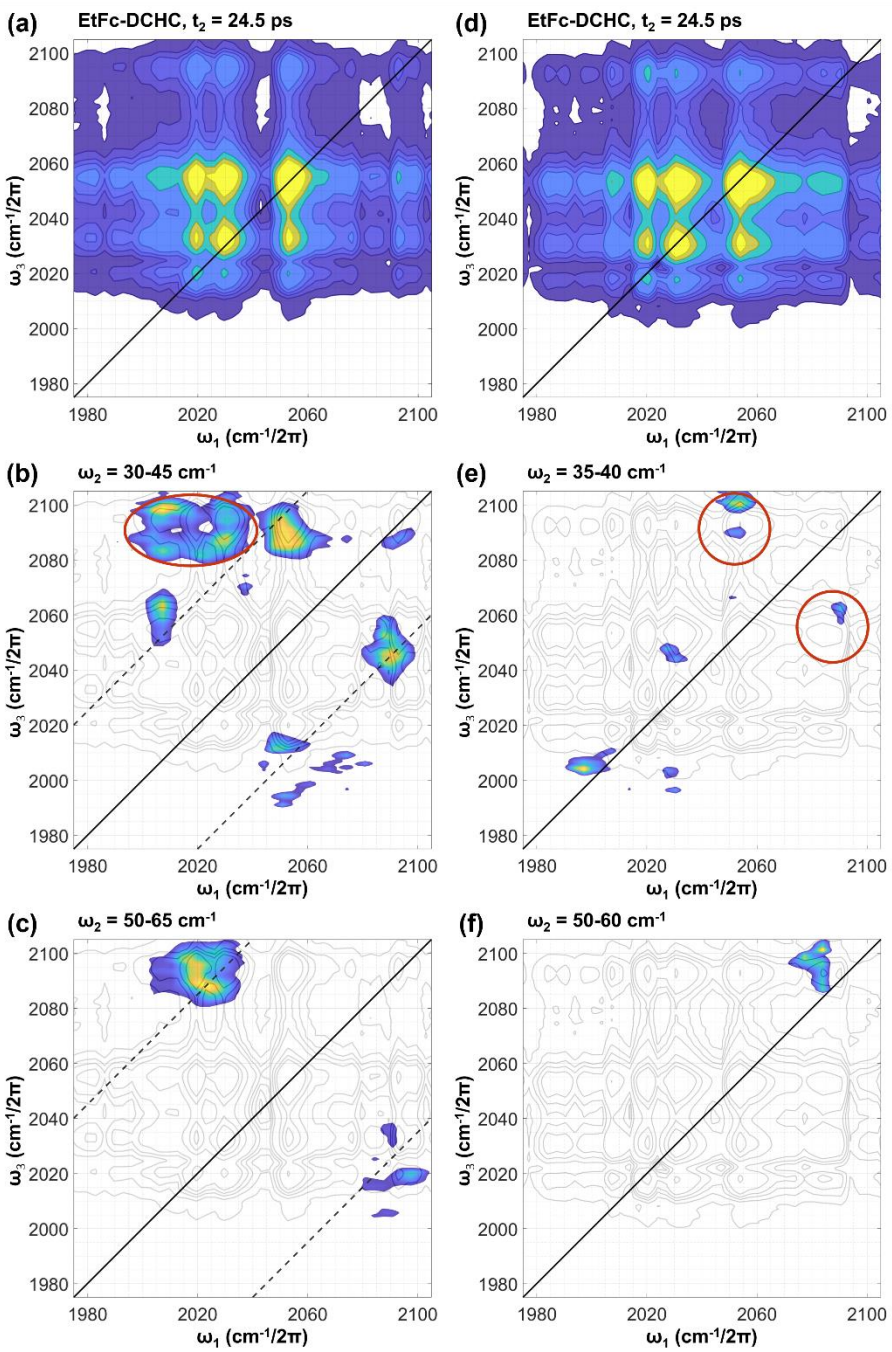

Figure 3.6: 2D-IR data for EtFc-DCHC including (a) rephasing absolute value 2D-IR spectrum, (b) rephasing coherence map at ω_2 = 30-45 cm^{-1}, (c) rephasing coherence map at ω_2 = 50-65 cm^{-1}, (d) nonrephasing absolute value 2D-IR spectrum, (e) nonrephasing coherence map at ω_2 = 35-40 cm^{-1}, and (f) nonrephasing coherence map at ω_2 = 50-60 cm^{-1}. Dotted lines have been added to show the upper limit of ω_2 for rephasing coherence maps. Red circles denote unexpected ω_2 intensities.

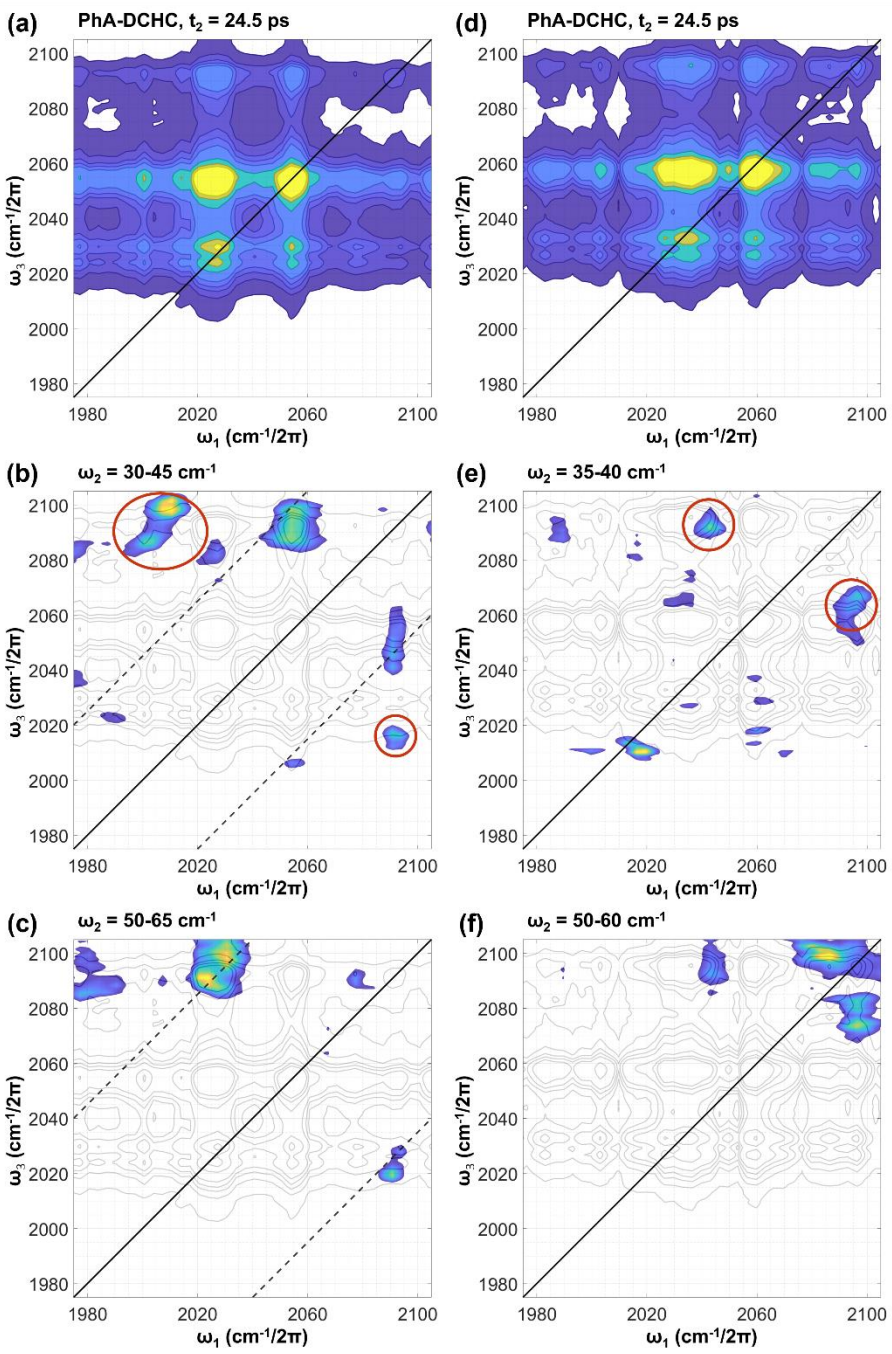

Figure 3.7: 2D-IR data for PhA-DCHC including (a) rephasing absolute value 2D-IR spectrum, (b) rephasing coherence map at ω_2 = 30-45 cm^{-1}, (c) rephasing coherence map at ω_2 = 50-65 cm^{-1}, (d) nonrephasing absolute value 2D-IR spectrum, (e) nonrephasing coherence map at ω_2 = 35-40 cm^{-1}, and (f) nonrephasing coherence map at ω_2 = 50-60 cm^{-1}. Dotted lines have been added to show the upper limit of ω_2 for rephasing coherence maps. Red circles denote unexpected ω_2 intensities.

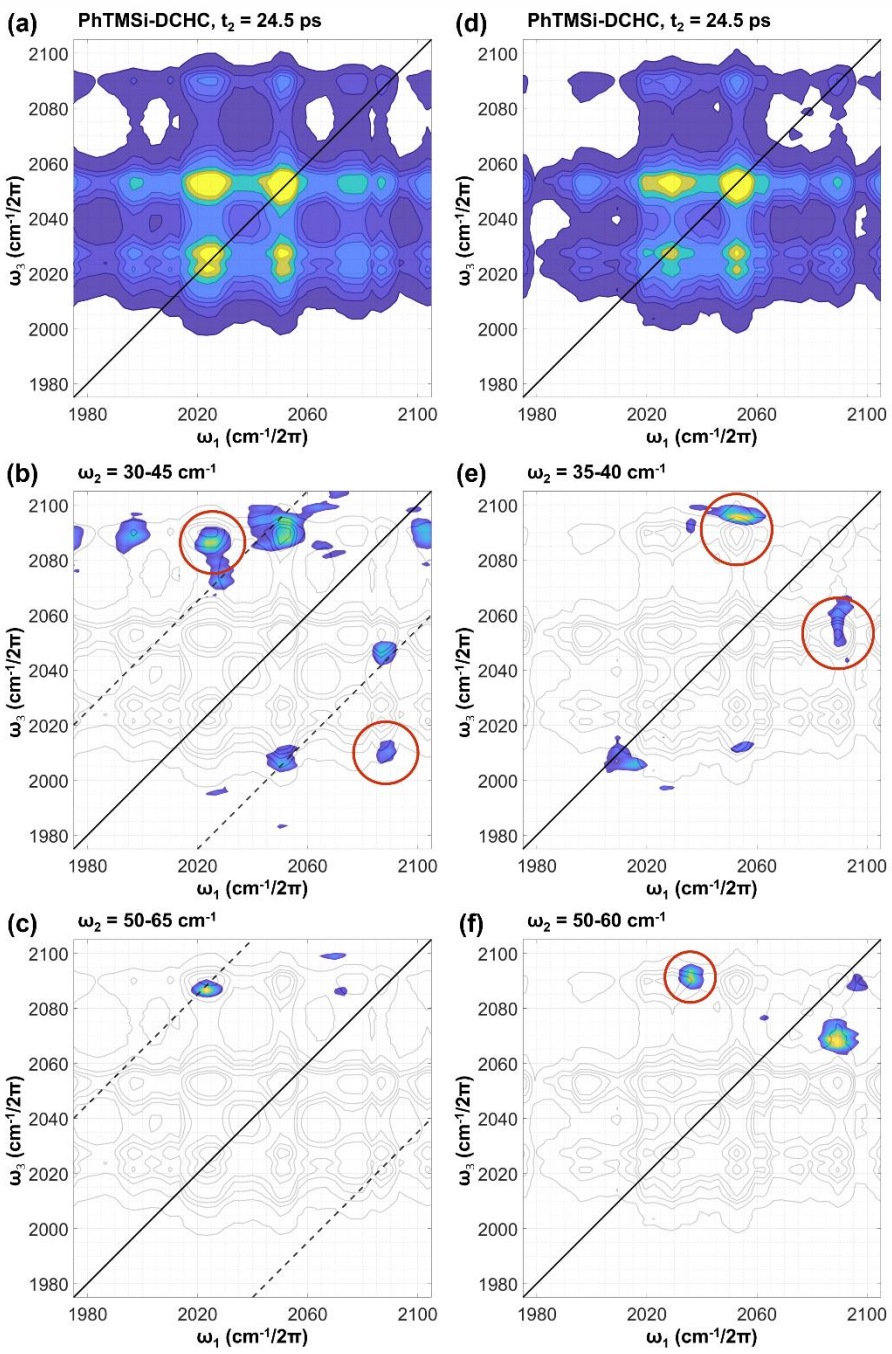

Figure 3.8: 2D-IR data for PhTMSi-DCHC including (a) rephasing absolute value 2D-IR spectrum, (b) rephasing coherence map at ω_2 = 30-45 cm^{-1}, (c) rephasing coherence map at ω_2 = 50-65 cm^{-1}, (d) nonrephasing absolute value 2D-IR spectrum, (e) nonrephasing coherence map at ω_2 = 35-40 cm^{-1}, and (f) nonrephasing coherence map at ω_2 = 50-60 cm^{-1}. Dotted lines have been added to show the upper limit of ω_2 for rephasing coherence maps. Red circles denote unexpected ω_2 intensities.

3.4 Discussion

In addition to the overall blue-shift in the energies of the aryl DCHC complexes' metal carbonyl stretching modes, two features are especially notable in comparison to the alkyl series—the separation of the low-frequency modes, and the convergence of modes **3** and **4**. For DPhA-DCHC and EtPyr-DCHC, modes **1** and **2** are distinguishable from one another due to the distorted symmetry of both complexes. In DPhA-DCHC, this distortion is caused by steric interactions between the two phenyl groups, which is analogous to that of *cis*-stilbene, and has been observed elsewhere in its crystal structure.[40,42] In EtPyr-DCHC, however, the separation of modes **1** and **2** is attributable to the large shift in the structure's dipole caused by pyrene itself. For both complexes, these structural changes induce stress on the relative C_{2v} symmetry of the cobalt carbonyl moiety, leading to the elimination of the potential dark mode. Conversely, EtFc-DCHC, PhA-DCHC, and PhTMSi-DCHC do not perturb the metal carbonyl modes sufficiently to deconvolute the two low frequency modes from one another, even though they are not symmetrically substituted complexes. Furthermore, in all five aryl-substituted complexes, modes **3** and **4** are shown to converge to varying degrees when compared to the alkyl series. This effect is least pronounced in EtFc-DCHC, while it is most pronounced in EtPyr-DCHC and DPhA-DCHC—leading to a possible explanation in the ligands' degrees of aromaticity. As increasingly aromatic ligands are introduced to the cobalt carbonyl moiety, electron density around the metal centers is delocalized by way of conjugation—leading to less π-backbonding between the cobalt atoms and their carbonyls.[34,37,38,87] Therefore, it is reasonable to assert that as ligand aromaticity increases, the carbonyls themselves are free to behave more like free CO than in the alkyl series. This

interpretation is further supported by the behaviors of PhA-DCHC and PhTMSi-DCHC, which have the same aromaticity due to a single phenyl group bound to one side of the bridging alkyne. With respect to DPhA-DCHC, PhA-DCHC, and PhTMSi-DCHC, it is important to note that PhA-DCHC experiences the farthest blue-shift of the three complexes, with PhTMSi-DCHC experiencing the smallest blue-shift of the aryl-substituted DCHC complexes. In this way, trimethylsilane can be seen as a mediator to the electron delocalization caused by the phenyl group.

Of the aryl series, EtFc-DCHC exhibits the most alkyl-like behaviors in its spectrum and vibrational modes, which is evidence for electron localization about the iron center of the ethynylferrocene ligand. The electronic properties of ferrocene both as a free-standing molecule and as a ligand are well known and have been reported at length elsewhere.[88,89] Despite its innate aromaticity, the presence of a third metal center in the ligand disrupts the normal electronic behavior of the bimetallic cobalt with an aromatic ligand; therefore, EtFc-DCHC is the least perturbed of the aryl-substituted complexes.

As with the alkyl series, the aryl complexes share several carbonyl modes in common without significant change. Namely, modes **5** and **6** are an in-phase antisymmetric stretch and a fully symmetric stretch, respectively, as they are in the alkyl complexes. For all aryl complexes except for EtFc-DCHC, mode **3** is a rocking motion in the equatorial carbonyls while mode **4** is an out-of-phase symmetric stretch; however, in EtFc-DCHC, these modes are flipped, which closely resembles the alkyl-substituted complexes.

Drawing further comparison between the alkyl and aryl series, the ω_2 coherences exhibited by the aryl-DCHC complexes are quite similar to those found in the alkyl complexes. As with the alkyl series, we observe the ω_2 coherences of modes **3** and **4** coalescing in all five aryl complexes, suggesting that coherence-to-coherence transfer occurs between the **4,6** vibrational coherence and the **3,6** vibrational coherence. This feature is even less surprising in the aryl series than in the alkyl series due to the convergence of the two modes in all but EtFc-DCHC, which maintains a 10 cm^{-1} difference frequency between modes **3** and **4**. Linear absorption spectra of the phenyl- and pyrene-substituted complexes show difference frequencies between 3 and 5 cm^{-1}, which is an even smaller barrier to interconversion than in EtFc-DCHC or the alkyl complexes. Additionally, all aryl complexes also show evidence for population-to-coherence transfer in their nonrephasing spectra, with ω_2 intensity arising along the **5,6** and **6,5** crosspeaks.

As with the alkyl series, a possible explanation for the coherence transfer phenomena observed in the aryl DCHC complexes is anharmonic coupling to low frequency fluxional modes that recruit the entire cobalt carbonyl moiety. Additionally, with the increased size of the aryl substituents, it is possible that torsional motion in the ligand itself may have a greater impact on the overall arrangement of the carbonyls themselves due to the high degree of conjugation throughout the ligand and metal center. The extent of this effect would be most noticeable in a more traditional treatment of the DCHC complexes' ultrafast dynamics.

As in the alkyl-DCHC series, the mechanism by which these modes undergo coherence transfer is likely due to anharmonic coupling between the high-frequency metal carbonyl stretching modes and low-frequency fluxional modes. Furthermore, DFT

calculations of the aryl-DCHC complexes indicate a manifold of low-frequency torsional modes that occur at frequencies analogous to the difference frequencies of the carbonyl stretching modes. Therefore, with the presence of these modes and strong electronic conjugation of the aryl-substituents themselves, it is reasonable to assert that the vibrational coherence transfer observed in the aryl-DCHC series proceeds along a similar mechanism to the alkyl-DCHC series, as discussed in chapter **2**.

3.5 Conclusion

In this work, we present evidence for coherence transfer events in a series of aromatically-substituted alkynyl dicobalt hexacarbonyl complexes. The similarities in the data between the alkyl- and aryl-substituted DCHC complexes suggest that vibrational coherence transfer in these molecules is robust even in the face of noticeable perturbance to their vibrational modes and molecular symmetries. Therefore, based on this work, the electronic influence of the selected aromatic ligands does not seem to otherwise disrupt the propensity for coherence transfer exhibited by alkynyl DCHC complexes in nonpolar solvent environments. Furthermore, due to the convergence of modes **3** and **4**, it is possible that the electronic delocalization granted by the aromatic ligand's conjugation contributes to the ease with which the metal carbonyl modes may share energy via anharmonic coupling.

Chapter 4

Ultrafast Vibrational Dynamics of Alkynyl Dicobalt Hexacarbonyl Complexes in Alkane Solvent Environments

4.1 Introduction

Since its earliest experiments, two-dimensional infrared (2D-IR) spectroscopy has relied on metal carbonyls as model systems for understanding ultrafast vibrational dynamics.[4,12] From the simplest complexes consisting of one or two carbonyls to metal carbonyl clusters containing many oscillators, metal carbonyls are uniquely useful as vibrational probes due to their electronic sensitivity—which is immediately reported in their vibrational energies.[33] This vibronic sensitivity is due largely to π-backbonding, in which the metal carbonyl both donates to and receives electrons from the metal to which it is bound. More precisely, the back-donation of electron density from the metal's valence shell into the π* antibonding orbital of the carbonyl directly affects the C≡O bond order, which, in turn, causes immediate changes in the metal carbonyl's observed stretching frequency.

Because the primary observable of the metal carbonyls—their stretching frequencies—are sensitive to the carbonyls' environment, a great deal of insight into ultrafast phenomena can be wrought from studying groups of metal carbonyls in various systems and conditions. For instance, for dicobalt octacarbonyl, which exists in two

distinct isomers, it is possible to spectroscopically distinguish between those isomers due to the cobalt carbonyls' stretching frequencies changing as the structure of the complex changes. Furthermore, with the use of 2D-IR, it is possible to observe this process as it happens by way of the metal carbonyls' vibrational modes changing during the course of the isomerization.[31]

For questions of vibrational dynamics in condensed media, one of 2D-IR's key observables is that of spectral diffusion, whereby we see a loss of correlation between excitation and detection frequencies as the system is allowed to evolve over time.[6,32] In polar solvent environments, the system's sampling of the unique microenvironments comprising its solvation shell are largely responsible for spectral diffusion. In general, we know that as the polarity of a solvent increases, the spectral features of a system in that solvent broaden as vibrational lifetimes decrease due to dephasing.[4] In addition to solvent polarity, the viscosity of a solvent also plays a key role in spectral diffusion. From previous work in our group, we know that alkanes, alkyl alcohols, and alkyl nitriles all modulate ultrafast vibrational dynamics with respect to the carbon chain length of the solvent.[3,6,58] An important distinction, however, must be made for the spectral diffusion of systems in nonpolar solvent environments. In a polar solvent, the collection of potential microenvironments depends greatly on the orientation of individual solvent molecules that can all individually exert influence over the solute. Conversely, in nonpolar solvents, the differences experienced by the solute in different solvation conditions are greatly diminished.[4] Therefore, when speaking of spectral diffusion in terms of a solute in a nonpolar environment, our attention turns inward. Rather than looking to intermolecular

forces competing with one another, we look to intramolecular phenomenon to make sense of the changes occurring within our systems.

Within the experimental constraints of 2D-IR, we can readily turn to intramolecular vibrational redistribution (IVR) to understand why a system of metal carbonyls in a nonpolar environment could experience enough change to undergo noticeable spectral diffusion. If we consider a hypothetical vibrational mode belonging to a metal carbonyl, we can envision that mode as a gaussian distribution of possible energies that can excite that particular vibration. Furthermore, because the excitation of a metal carbonyl is sensitive to the π-backbonding between the metal and the C≡O moiety itself, we can assign particular states of the metal carbonyl to energetic regimes within this gaussian distribution, as shown in **Figure 4.1a**.

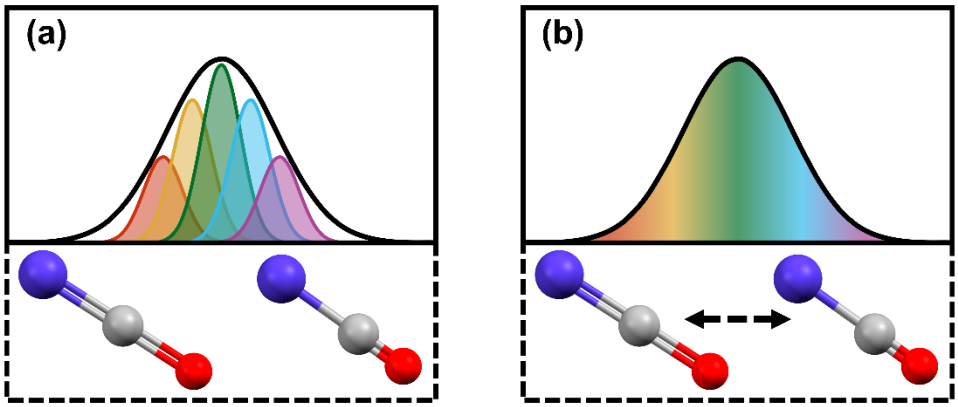

Figure 4.1: An illustration of (a) potential carbonyl stretching frequencies with respect to C≡O bond length, and (b) the spectral results of interconversion between the carbonyl populations over time.

As previously discussed in section **1.2**, a metal carbonyl's stretching frequencies are inversely proportional to the length of the C≡O bond itself. Therefore, if we are to consider the low-energy or red end of the distribution of possible metal carbonyl excitations, we will assign that to an extended C≡O bond, that may potentially share more characteristics with a doubly bound C=O than with free carbon monoxide. Alternatively, if

we consider the high-energy or blue end of that same distribution, we know that the blue-shift is associated with a shortened C≡O bond that shares much more of its nature with free carbon monoxide. If we further assume that these carbonyls are in an environment where they can share energy with one another, we then know that the metal carbonyl populations themselves have the potential to interconvert with one another. This interconversion, over time, is therefore responsible for our nonpolar spectral diffusion, as shown in **Figure 4.1b**.

Moving away from this group of independent metal carbonyls, we can apply the same thought process to a group of metal carbonyls in a single molecule. Because they will experience similar energetic environment in potentially different ways, it follows that a distribution of metal carbonyl energies will also arise, although now the metal carbonyls are coupled to each other by way of their shared molecular structure. For systems such as alkynyl dicobalt hexacarbonyl (DCHC) complexes, there are a number of possible pathways by which individual metal carbonyls may experience slight variations in their environment, even within a single vibrational mode.

One common method that is frequently used to assess spectral diffusion in 2D-IR is the calculation of the frequency-frequency correlation function (FFCF), which provides a direct measurement of the degree of correlation between excitation and detection frequencies over time. Using absolute value rephasing and nonrephasing spectra, the FFCF may be calculated by way of an inhomogeneity index, which is defined as follows:[65]

$$II(t_2) = \frac{R(t_2) - NR(t_2)}{R(t_2) + NR(t_2)} \tag{4.1}$$

This work presents a series of three alkynyl DCHC complexes that have been investigated with 2D-IR spectroscopy in both *n*-heptane and *n*-dodecane to uncover the intramolecular processes that may impact their ultrafast vibrational dynamics through IVR.

4.2 Experimental Methods

Three substituted alkynyl DCHC complexes were synthesized according to the methods established by Happ and coworkers.[45] 3-hexyne (3-hex) DCHC, bis(trimethylsilyl)acetylene (TMSi) DCHC, and ethynylpyrene (EtPyr) DCHC were synthesized according to literature methods using equimolar quantities of dicobalt octacarbonyl and their respective alkyne ligands mixed in *n*-pentane. Reaction mixtures were left to stir overnight under nitrogen pressure and red light to prevent the degradation of the cobalt carbonyl. The remaining solvent was removed *in vacuo,* and reaction products were purified with column chromatography using an 80%:20% (v/v) petroleum ether and dichloromethane mobile phase with a silica gel stationary phase. The products were collected as a single dark band and were subsequently recrystallized. All three reactions produced dark brown or dark reddish-brown crystalline products. The structures and linear absorption spectra of the three complexes are shown in **Figure 4.2**.

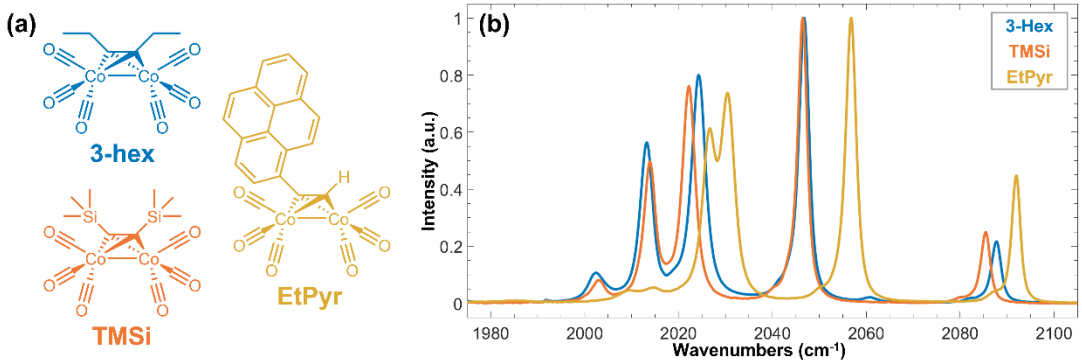

Figure 4.2: (a) Structures of the 3-hex (blue), TMSi (orange), and EtPyr (yellow) DCHC complexes, and (b) linear absorption spectra of their metal carbonyl stretching modes in n-heptane.

2D-IR spectroscopy experiments were performed using the apparatus described in section **1.3.1**. Absolute value rephasing and nonrephasing 2D-IR spectra were collected along a series of time points between -0.5 and 35 ps, with fine sampling over the first 5 picoseconds and more sparse sampling out to 35 picoseconds. Spectra were recorded for all three complexes in both *n*-heptane and *n*-dodecane. The linear absorption spectra for all three complexes show almost no differences between the two solvents; therefore, only FTIR spectra for *n*-heptane are shown.

4.3 Results

Absolute value rephasing and nonrephasing spectra were collected for all three complexes in both *n*-heptane and *n*-dodecane between -0.5 and 35 ps. Progressions of 2D-IR spectra for 3-hex-DCHC, TMSi-DCHC, and EtPyr-DCHC in *n*-heptane at t_2 = 0.5 ps, 10 ps, and 25 ps are provided in **Figure 4.3** through **4.5**, respectively.

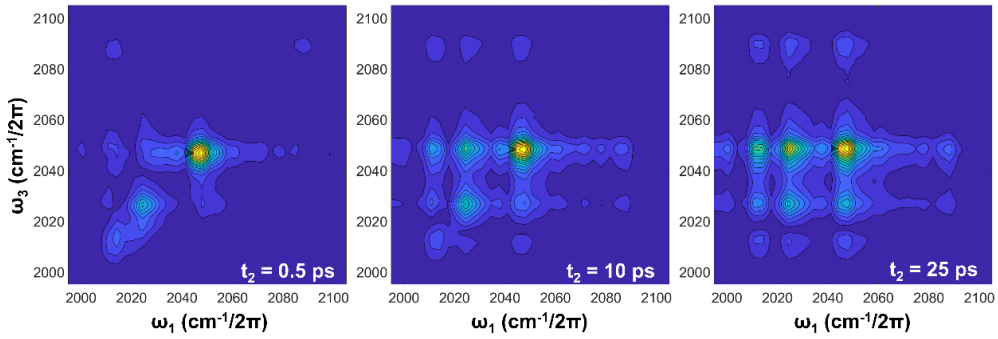

Figure 4.3: 2D-IR spectra of 3-hex-DCHC in n-heptane at 0.5 ps, 10 ps, and 25 ps.

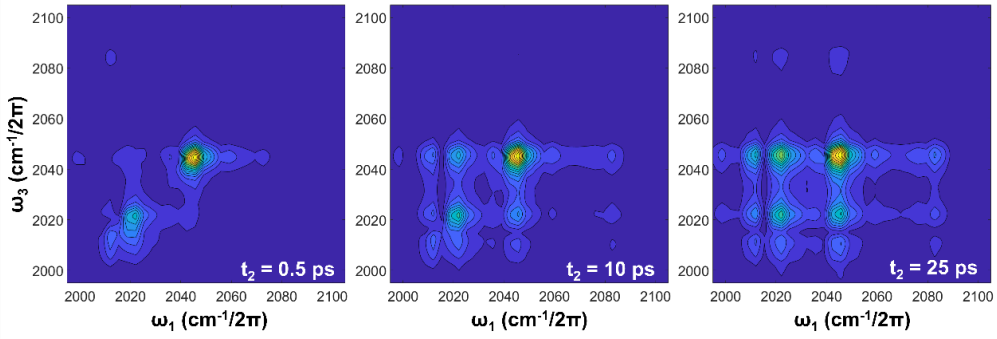

Figure 4.4: 2D-IR spectra of TMSi -DCHC in n-heptane at 0.5 ps, 10 ps, and 25 ps.

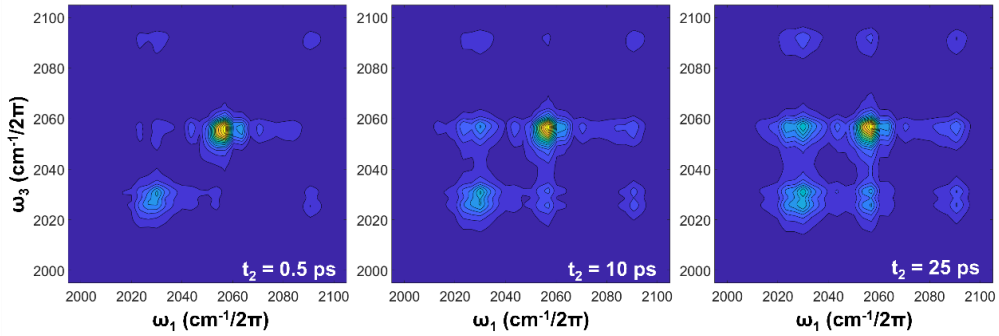

Figure 4.5: 2D-IR spectra of EtPyr -DCHC in n-heptane at 0.5 ps, 10 ps, and 25 ps.

FFCFs were calculated for each complex in both solvents, via their inhomogeneity indices. FFCFs and rephasing peak amplitudes for mode **5** in each complex are given in **Figure 4.6** for data collected in *n*-heptane and **Figure 4.7** for data collected in *n*-dodecane.

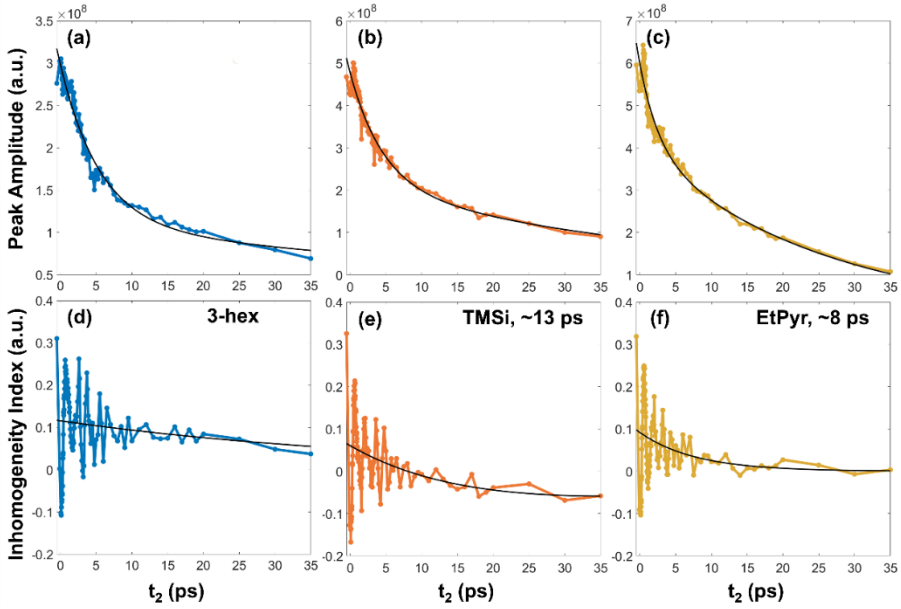

Figure 4.6:: Traces over t_2 for (a-c) rephasing peak amplitudes for mode **5** of 3-hex-DCHC (blue), TMSi-DCHC (orange), and EtPyr-DCHC (yellow) and (d-f) FFCFs for mode **5** of 3-hex-DCHC (blue), TMSi-DCHC (orange), and EtPyr-DCHC (yellow) in n-heptane.

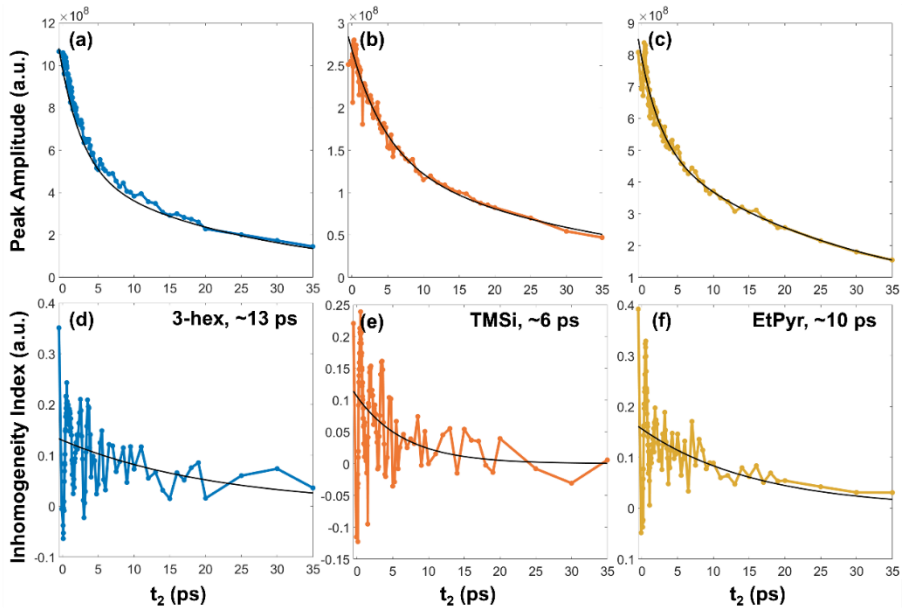

Figure 4.7: Traces over t_2 for (a-c) rephasing peak amplitudes for mode **5** of 3-hex-DCHC (blue), TMSi-DCHC (orange), and EtPyr-DCHC (yellow) and (d-f) FFCFs for mode **5** of 3-hex-DCHC (blue), TMSi-DCHC (orange), and EtPyr-DCHC (yellow) in n-dodecane.

Looking at the ω_2 coherences of the complexes, we see no substantive change in coherence or coherence transfer behavior between the two solvent environments. Rephasing Frobenius spectra for the **3,6** crosspeak and selected rephasing coherence maps for TMSi-DCHC in *n*-heptane and *n*-dodecane are provided in **Figure 4.8** and **Figure 4.9**, respectively.

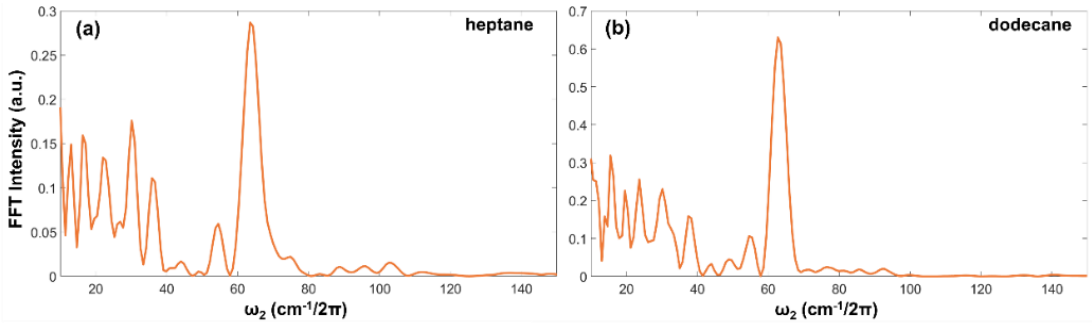

Figure 4.8: Rephasing Frobenius spectra of the **3,6** crosspeak in TMSi in (a) n-heptane and (b) n-dodecane.

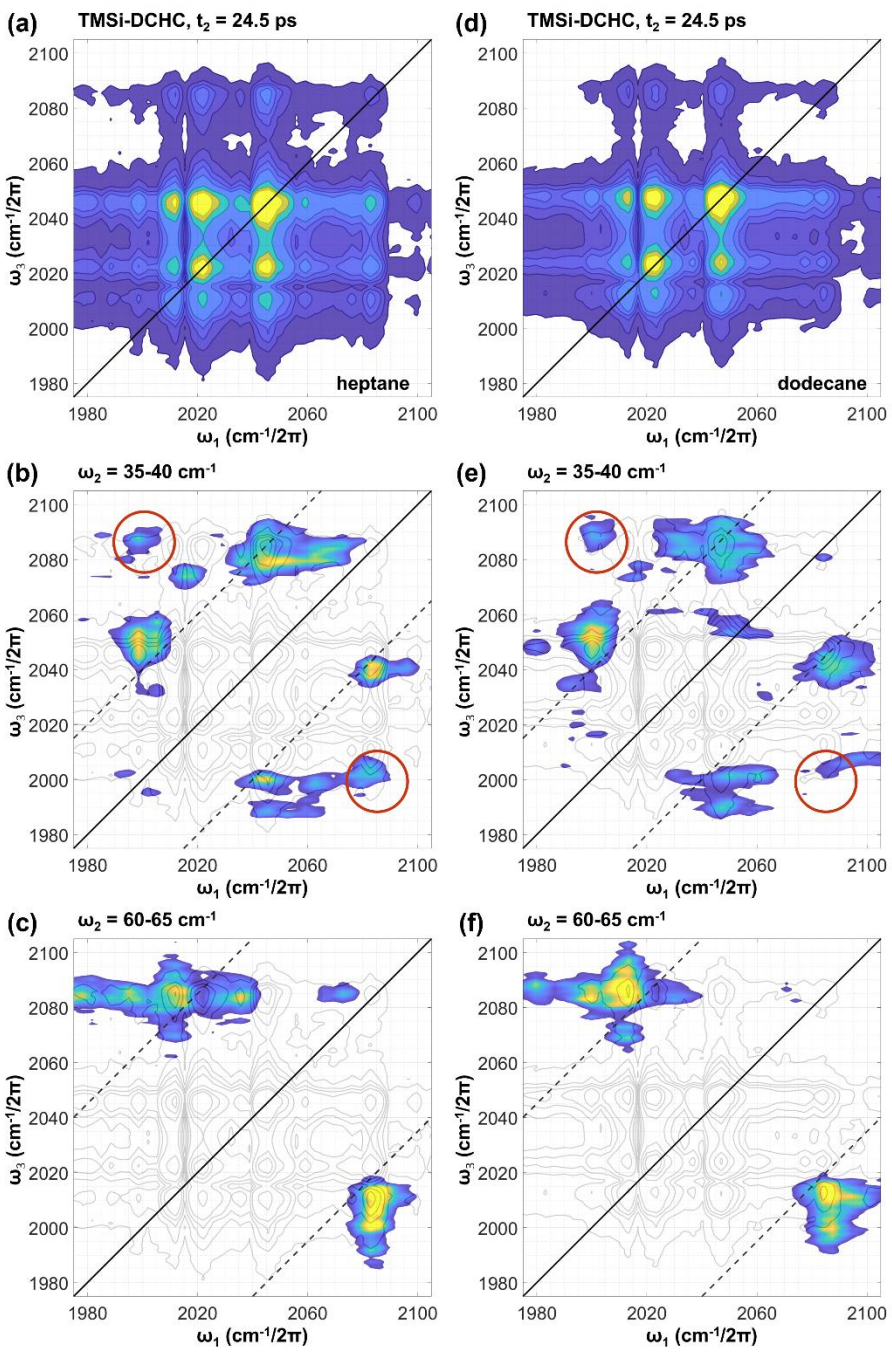

Figure 4.9: 2D-IR data for TMSi-DCHC in (a-c) n-heptane and (d-f) n-dodecane including (a and d) rephasing absolute value 2D-IR spectrum, (b and e) rephasing coherence maps at ω_2 = 35-40 cm^{-1}, and (c and f) rephasing coherence maps at ω_2 = 60-65 cm^{-1}.

4.4 Discussion

All three complexes exhibit ultrafast vibrational dynamics consistent with those reported elsewhere for metal carbonyls in alkane environments.[6] Due to oscillations in

the nonrephasing peak amplitude for mode **5**, approximate timescales for spectral diffusion are given with large confidence intervals. Conversely, when comparing the mode **5** peak amplitudes of the three complexes, all of which may be easily fit with a biexponential function, slight but ultimately negligible differences arise in their short timescale decays. 3-hex-DCHC exhibits the most difference between the two solvent environments, with τ = 5.5 ± 1.0 ps for *n*-heptane and τ = 3.1 ± 0.5 ps for *n*-dodecane. The data for TMSi-DCHC suggest decays of τ = 4.5 ± 1.2 ps in *n*-heptane and τ = 4.9 ± 1.5 ps in *n*-dodecane. Finally, the data for EtPyr-DCHC suggest decays of τ = 2.6 ± 0.9 ps in *n*-heptane and τ = 2.9 ± 0.8 ps in *n*-dodecane. For both TMSi- and EtPyr-DCHC, timescales in the two solvents fall within error, and do not suggest a strong relationship between the two solvent environments and the complexes' spectral diffusion. Conversely, 3-hex-DCHC exhibits significantly different timescales in the two constants; however, this anomalous result can be attributed to the oscillations in the FFCF due to quantum beating in the diagonal peak for mode **5**. Systems with similar characteristics have shown negligible differences once their FFCFs have been corrected to remove these large oscillatory features.[6] Because this data was collected with coherences in mind, the t_2 vector is not long enough to properly assess IVR timescales.

Furthermore, similarities in the ω_2 coherences of the complexes in the two solvents suggest that the environment experienced by the complexes in *n*-heptane and *n*-dodecane do not differ enough to influence the complexes' ability to share energy among their carbonyl modes. When accounting for the relative intensities of the ω_2 coherences, the complexes exhibit the same behavior in both solvents.

4.5 Conclusion

The 2D-IR data presented here concurs with that collected for similar systems in alkane environments.[6] For the aspects of ultrafast dynamics that these 2D-IR data are able to address, we do not see significant differences between either the complexes themselves or their solvent environments. The vibrational lifetimes and FFCF data presented here are in general agreement with data previously collected in our group for diiron dithiolate hexacarbonyls; however, further investigation of the DCHC complexes' IVR with respect to their solvent environments is warranted.

Chapter 5

Conclusion

5.1 Key Results

The work presented here provides an investigation into the ultrafast dynamics of a series of eight systematically-substituted dicobalt hexacarbonyl (DCHC) complexes. More specifically, we assert that all eight DCHC complexes studied exhibit evidence for anharmonically coupled coherence transfer. Despite steric and electronic changes in the ligands' substituents and obvious perturbances to the complexes' IR absorption, we found no substantive difference in the complexes' propensity for coherence transfer. In both rephasing and nonrephasing signal pathways, we observe quantum beats that can only arise through nonsecular coherence transfer processes. Therefore, this dissertation serves as a first step in arguing for the generalization of coherence transfer in C_{2v} bimetallic hexacarbonyl complexes.

We demonstrate, to the extent investigated here, that perturbances to the molecular, electronic, and vibrational structure of the DCHC moiety do not preclude coherence transfer events. Therefore, for questions of their ultrafast dynamics, it is vital that these complexes' behavior be understood within the context of the strong intraband coherences they experience and the anharmonic coupling that may potentially play a significant role in the exchange of energy between the vibrational modes. In fact, despite

noticeable shifts in the overall vibrational modes of the aryl series with respect to the electronically unperturbed alkyl series, we observe no significant changes in the intraband coherences or the observed coherence transfer of the DCHC complexes. When considered within the context of work previously done in our group on diiron dithiolate hexacarbonyls, we find that vibrational coherence transfer is characteristic in both the diiron and dicobalt hexacarbonyl systems. This commonality may be attributed to their geometric and electronic similarities and is sufficient evidence to warrant further investigation of similar molecular systems with respect to potential vibrational coherence transfer.

The robustness of the vibrational coherence transfer processes we find in alkynyl DCHC complexes indicate that the secular approximation of Redfield theory is not sufficient to fully address the physical reality of how these molecules interact with themselves or their surroundings during and after photoexcitation. Moreover, the profound similarities between alkynyl DCHC complexes and diiron dithiolate hexacarbonyl complexes suggests that the vibrational coherence transfer we observe in both is a foundational feature of their molecular structures and not merely the result of coincidence.

5.2 Future Directions

Systematically understanding vibrational coherence transfer from a vibronic and structural viewpoint necessitates the selection of new and more varied systems containing similarities to those already investigated. For DCHC complexes as a synthetic platform, the work presented here focused primarily on making incremental changes to the structure of the ligand; however, the versatility of the dicobalt-alkyne click chemistry

provides innumerable possibilities for ligands tailored to questions of electronic and steric interference. First looking to the electronic structure of DCHC complexes, adduction of ligands with stronger electron-withdrawing or electron-donating characteristics may provide ample disruption to the metal carbonyls to obstruct their vibrational modes more forcefully. As a first step toward this direct electronic modulation, we propose the future study of ethynylfluorobenzene ligands, as shown in **Figure 5.1**.

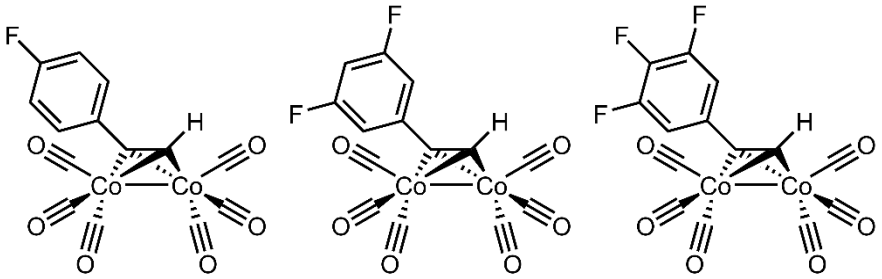

Figure 5.1: A series of ethynylfluorobenzene DCHC complexes.

In addition to dicobalt carbonyl complexes, heterobimetallic carbonyl complexes may provide insight into the overall resilience of the hexacarbonyl motif found in both the DCHC complexes as well as the diiron dithiolate complexes. Moore and coworkers have reported the synthesis of stable propargyl iron-cobalt hexacarbonyl complexes by substitution of $Fe(CO)_3$ for one side of the $Co_2(CO)_6$ moiety, yielding a heterobimetallic hexacarbonyl complex with an asymmetrically bridging alkene ligand, as shown in **Figure 5.2**.[90] These FeCo complexes have long been the focus of work seeking to characterize paramagnetic and spin-coupled complexes, and could provide unique insights into questions of anharmonic coupling with respect to mixed-valence systems.[91,92]

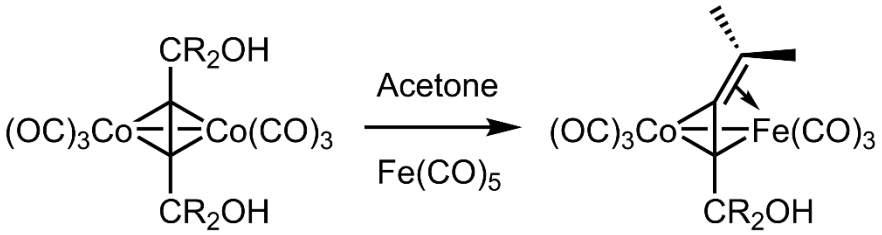

Figure 5.2: Synthesis of a heterobimetallic iron-cobalt hexacarbonyl propargyl cation by isolobal substitution of cobalt tricarbonyl by iron pentacarbonyl.[78]

Ultrafast spectroelectrochemistry (SEC) provides additional opportunities for continued investigation of DCHC complexes. Given the established electrochemistry of ferrocene-containing complexes, 2D-IR SEC of heterometallic DCHC complexes offers an alternative route toward electronic control of the metal carbonyl moiety.[93] Recent work in our group studying chlororhenium tricarbonyl complexes with 2D-IR SEC serves as an excellent foundation for future studies of heterometallic systems' vibronic coupling.

Due to the apparent effectiveness of the secular approximation in describing the ultrafast dynamics of many systems, the effects of vibrational coherence transfer in small molecules are largely unexplored outside of a few isolated systems.[2,11,12,15,74,77] Because of this dearth of information, any further experimental work must also be accompanied by further theoretical and computational evaluation of the models we use to assess ultrafast processes. In both the diiron dithiolate and alkynyl dicobalt hexacarbonyl complexes, we observe near-identical coherence transfer among their analogous metal carbonyl stretching modes. Therefore, uncovering the mechanisms by which these coherence transfer events arise is a worthy pursuit as we seek increasingly better models with which we may describe the world around us.

Appendix

A.1 Derivation of the Redfield Equation

The following derivation of the Redfield equation is adapted from the notes of Gert van der Zwan and largely follows the derivations presented by A.G. Redfield and Shaul Mukamel.[67,76,94] Beginning with the Liouville equation for a density operator $\rho(t)$, we find that

$$\frac{\partial \rho(t)}{\partial t} = -2\pi i[\mathcal{H}, \rho(t)] \tag{1.6}$$

Which is functionally equivalent to **Equation 1.1**. For the sake of this derivation, the system Hamiltonian $\mathcal{H}$ will consist of the unperturbed term $\mathcal{H}_0$ with eigenvalues ϵ_n and eigenfunctions $|n\rangle$ and the randomly perturbed term $\mathcal{H}_r$ that couples the system operators A_k to an external field $E_k(t)$ such that,

$$\mathcal{H}_r = \sum_k A_k E_k(t) \tag{1.7}$$

Moving into the interaction picture, $\rho(t)$ becomes

$$\rho_I(t) = e^{2\pi i \mathcal{H}_0 t} \rho(t) e^{-2\pi i \mathcal{H}_0 t} \tag{1.8}$$

To evolve over time, which allows **Equation 1.6** to be expressed in terms of $\rho_I(t)$, as follows:

$$\frac{\partial \rho_I(t)}{\partial t} = -2\pi i\left[\mathcal{H}_{r,I}(t), \rho_I(t)\right] \tag{1.9}$$

Iteratively solving $\partial\rho_I(t)/\partial t$ to the second order yields the following integral solution, which serves as the foundation of the rest of the derivation:

$$\rho_I(t) = \rho_I(0) - 2\pi i \int_0^t d\tau \left[\mathcal{H}_{r,I}(\tau), \rho_I(\tau)\right] \tag{1.10}$$

By employing a series expansion, $\rho_I(t)$ becomes

$$\rho_I(t) = \rho_I(0) - 2\pi i \int_0^t d\tau\left[\mathcal{H}_{r,I}(\tau), \rho_I(\tau)\right] - 4\pi^2 \int_0^t d\tau \int_0^\tau d\tau' \left[\mathcal{H}_{r,I}(\tau), \left[\mathcal{H}_{r,I}(\tau'), \rho_I(0)\right]\right] + \cdots \tag{1.11}$$

Taking the time derivative of the previous expression then yields

$$\frac{d\rho_I(t)}{dt} = -2\pi i\left[\mathcal{H}_{r,I}(t), \rho_I(0)\right] - 4\pi^2 \int_0^t d\tau[\mathcal{H}_{r,I}(t), \mathcal{H}_{r,I}(\tau), \rho_I(0)]] + \cdots \tag{1.12}$$

Moving forward, we make two assumptions: First, that the average of the external field $\langle E_k(t)\rangle$ is equal to zero; and second, that the external field's fluctuations are uncorrelated with $\rho_I(0)$. These assumptions cause the first term in **Equation 1.12** to drop to zero, leaving the following expression:

$$\frac{d\rho_I(t)}{dt} = -4\pi^2 \int_0^t d\tau \left\langle\left[\mathcal{H}_{r,I}(t), \left[\mathcal{H}_{r,I}(\tau), \rho_I(0)\right]\right]\right\rangle \tag{1.13}$$

Furthermore, because $A_k(t)$ and $E_k(t)$ are independent of one another, they may be separated, such that

$$\frac{d\rho_I(t)}{dt} = -4\pi^2 \sum_{n,m} \int_0^t d\tau \langle E_n(t) E_m(t) \rangle \big[A_n(t), [A_m(\tau), \rho_I(0)]\big] \tag{1.14}$$

Where the time-dependence ascribed to $A_{n,m}$ necessitates an evaluation within the interaction picture, and we may further assume that the averaged interaction is stationary such that

$$\frac{d\rho_I(t)}{dt} = -4\pi^2 \sum_{n,m} \int_0^t d\tau \langle E_m E_n(t-\tau) \rangle \big[A_n(t), [A_m(\tau), \rho_I(0)]\big] \tag{1.15}$$

Substituting $t - \tau$ for τ then yields the following expression that has exchanged the upper integration limit t for $+\infty$ to indicate that the correlation term $\langle E_m E_n(\tau) \rangle$ will vanish entirely before $\rho_I(0)$ can substantively change.

$$\frac{d\rho_I(t)}{dt} = -4\pi^2 \sum_{n,m} \int_0^\infty d\tau \langle E_m E_n(\tau) \rangle \big[A_n(t), [A_m(t-\tau), \rho_I(0)]\big] \tag{1.16}$$

Using eigenfunctions of $\mathcal{H}_0$, $|\alpha\rangle$ and $|\beta\rangle$, we are able to evaluate the commutators for A_k, such that

$$\frac{d}{dt}(\rho_I)_{\alpha\alpha'} = -4\pi^2 \sum_{n,m} \int_0^\infty d\tau \langle E_m E_n(\tau) \rangle \big\langle \alpha \big| \big[A_n(t), [A_m(t-\tau), \rho_I]\big] \big| \alpha' \big\rangle \tag{1.17}$$

Where the commutator itself has four terms that must be considered separately. With the first term being presented as follows:

$$\langle \alpha | A_n(t) A_m(t-\tau) \rho_I | \alpha' \rangle = \sum_{\beta,\beta'} \langle \alpha | A_n(t) | \beta \rangle \langle \beta | A_m(t-\tau) | \beta' \rangle \langle \beta' | \rho_I | \alpha' \rangle \tag{1.18}$$

Returning to the interaction picture definition of $\rho(t)$ presented in **Equation 1.8**, we may further transform the first term of the commutator such that

$$\langle\alpha|A_n(t)A_m(t-\tau)\rho_I|\alpha'\rangle = \sum_{\beta,\beta'} e^{2\pi i(\alpha-\beta)t} e^{2\pi i(\beta-\beta')(t-\tau)} (A_n)_{\alpha\beta}(A_m)_{\beta\beta'}(\rho_I)_{\beta'\alpha'} \quad (1.19)$$

Introducing a dummy summation over γ allows the first term to become

$$\langle\alpha|A_n(t)A_m(t-\tau)\rho_I|\alpha'\rangle = \sum_{\beta,\beta'} \left[\delta_{\alpha'\beta'} \sum_{\gamma} e^{2\pi i(\beta-\gamma)\tau} e^{2\pi i(\alpha-\beta)t} (A_m)_{\gamma\beta}(A_n)_{\alpha\gamma} \right] (\rho_I)_{\beta\beta'} \quad (1.20)$$

The other three terms of the commutator are treated similarly, leading to the following second term:

$$-\langle\alpha|A_m(t-\tau)\rho_I A_n(t)|\alpha'\rangle = -\sum_{\beta,\beta'} e^{2\pi i(\beta-\alpha)\tau} e^{2\pi i(\alpha-\beta+\beta'-\alpha')t} (A_m)_{\alpha\beta}(A_n)_{\beta'\alpha'}(\rho_I)_{\beta\beta'} \quad (1.21)$$

The third term, additionally, becomes

$$-\langle\alpha|A_m(t-\tau)\rho_I A_n(t)|\alpha'\rangle = -\sum_{\beta,\beta'} e^{2\pi i(\beta-\alpha)\tau} e^{2\pi i(\alpha-\beta+\beta'-\alpha')t} (A_m)_{\alpha\beta}(A_n)_{\beta'\alpha'}(\rho_I)_{\beta\beta'} \quad (1.22)$$

Leading to the following fourth term:

$$\langle\alpha|\rho_I A_m(t-\tau)A_n(t)|\alpha'\rangle = \sum_{\beta,\beta'} \left[\delta_{\alpha\beta} \sum_{\gamma} e^{2\pi i(\gamma-\beta')\tau} e^{2\pi i(\beta'-\alpha)t} (A_m)_{\beta'\gamma}(A_n)_{\gamma\alpha'} \right] (\rho_I)_{\beta\beta'} \quad (1.23)$$

Upon returning to the Heisenberg picture, each exponential term containing t cancel with one another, leaving the following expression for the Redfield equation in the most general terms, where each term of the commutator is represented as C_k for $k = 1$ to $k = 4$:

$$\frac{\partial \rho_{\alpha\alpha'}(t)}{\partial t} = -2\pi i(\alpha-\alpha')\rho_{\alpha\alpha'}(t) - 4\pi^2 \sum_{n,m} \sum_{k=1}^{4} C_k \quad (1.24)$$

By further assuming that, for an isotropic system, every field component, $E_k(t)$, will decay in the same way and will have equal equilibrium averages, the integral terms of each commutator simplify to

$$\int_0^\infty d\tau \langle E_m E_n(\tau)\rangle e^{2\pi i\omega\tau} = \delta_{nm}\frac{\langle E^2\rangle}{2\pi(\zeta - i\omega)} \equiv \delta_{nm}\frac{1}{2\pi}J(\omega) \tag{1.25}$$

Where coupling between two modes separated by a frequency ω, is given by $J(\omega)$, and the Which yields the following definition of the general Redfield equation:

$$\begin{aligned}\frac{\partial \rho_{\alpha\alpha'}(t)}{\partial t} &= -2\pi i(\alpha - \alpha')\rho_{\alpha\alpha'}(t) \\ -2\pi \sum_{\beta,\beta'} \Bigg[&\delta_{\alpha'\beta'} \sum_{\gamma} J(\beta - \gamma) A_{\gamma\beta} \cdot A_{\alpha\gamma} \\ &- [J(\alpha' - \beta') + J(\beta - \alpha)] A_{\beta'\alpha'} \cdot A_{\alpha\beta} \\ &+ \delta_{\alpha\beta} \sum_{\gamma} J(\gamma - \beta') A_{\beta'\gamma} \cdot A_{\gamma\alpha'} \Bigg] \rho_{\beta\beta'}\end{aligned} \tag{1.26}$$

Where each $A_{nm} \cdot A_{mn}$ represents the inner product such that

$$A_{\beta'\alpha'} \cdot A_{\alpha\beta} = \sum_n (A_n)_{\beta'\alpha'} (A_n)_{\alpha\beta} \tag{1.27}$$

A.2 Assignment of Modes for Alkynyl DCHC Complexes

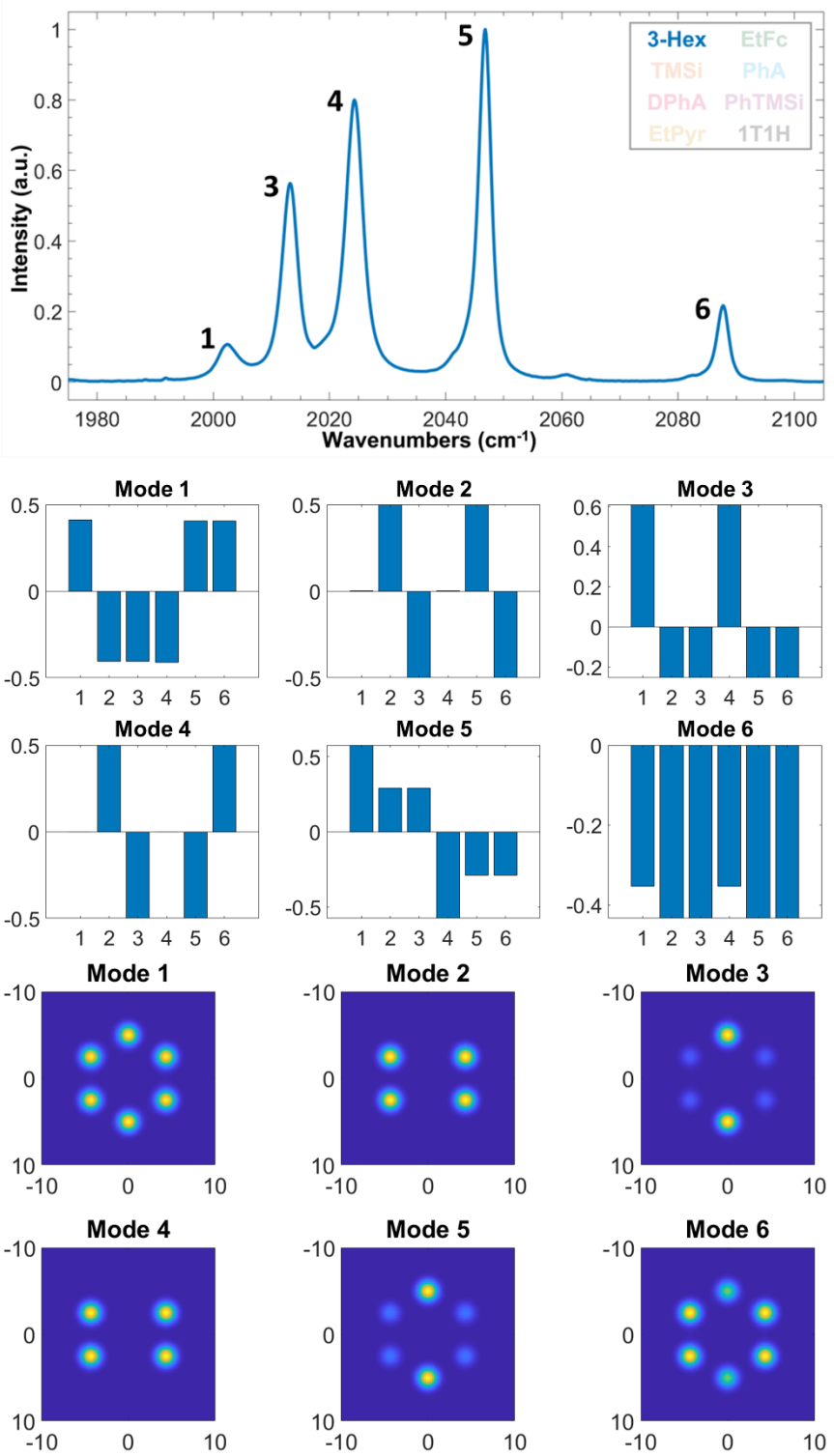

Figure A.1: (top-down) Linear absorption spectrum, normalized carbonyl displacements by vibrational mode, and carbonyl recruitment probability by vibrational mode for 3-Hex-DCHC.

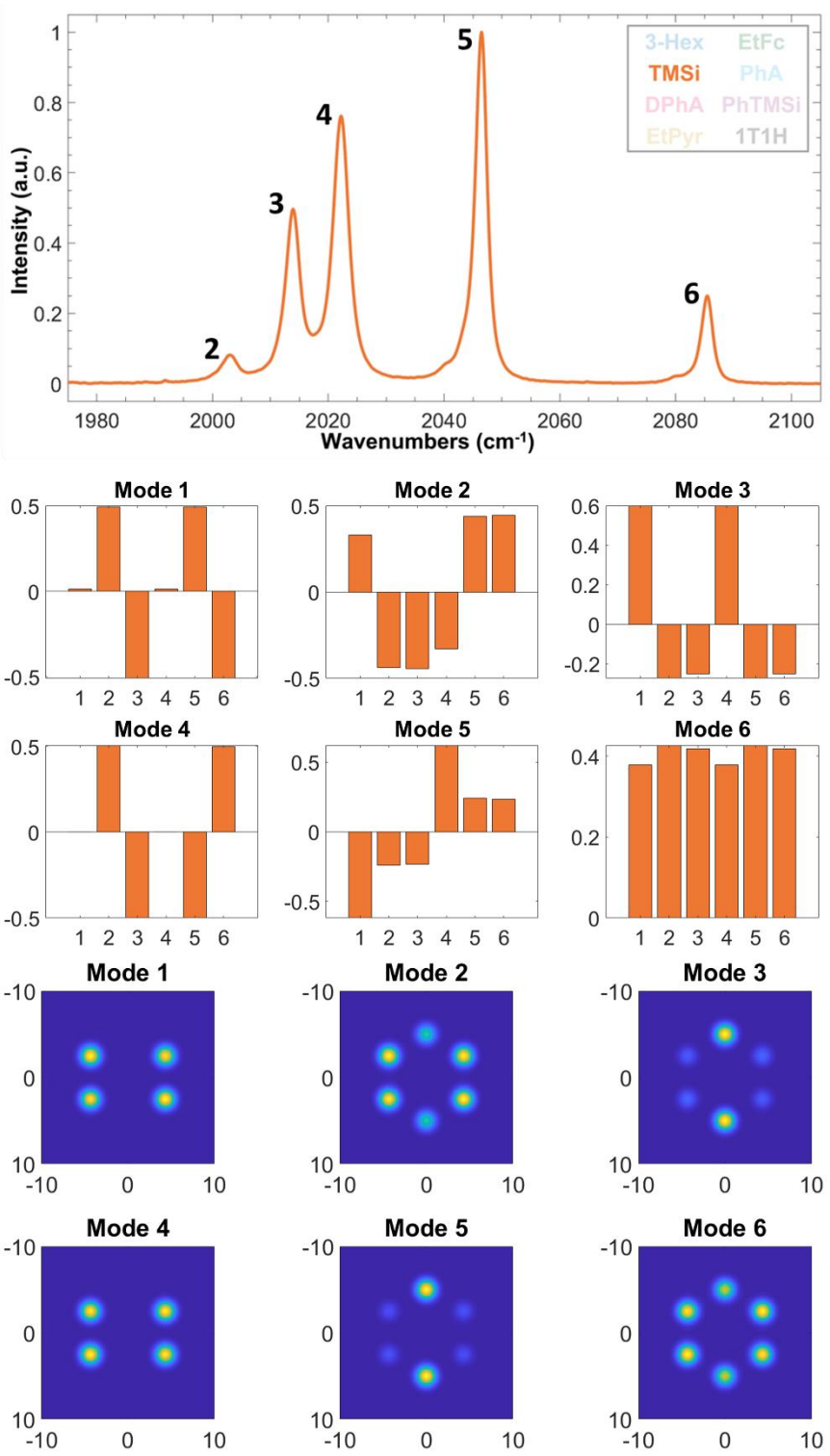

Figure A.2: (top-down) Linear absorption spectrum, normalized carbonyl displacements by vibrational mode, and carbonyl recruitment probability by vibrational mode for TMSi-DCHC.

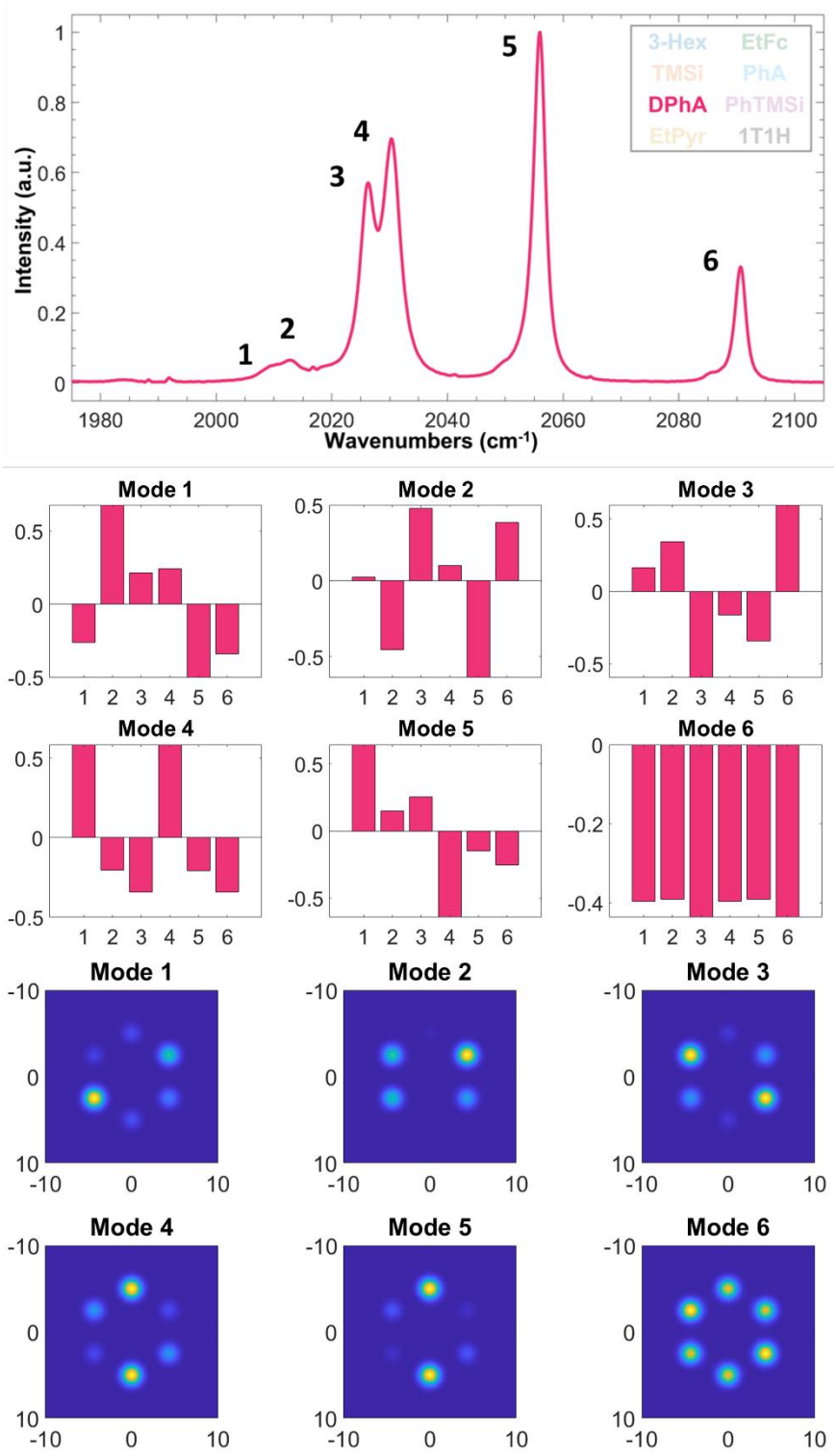

Figure A.3: (top-down) Linear absorption spectrum, normalized carbonyl displacements by vibrational mode, and carbonyl recruitment probability by vibrational mode for DPhA-DCHC.

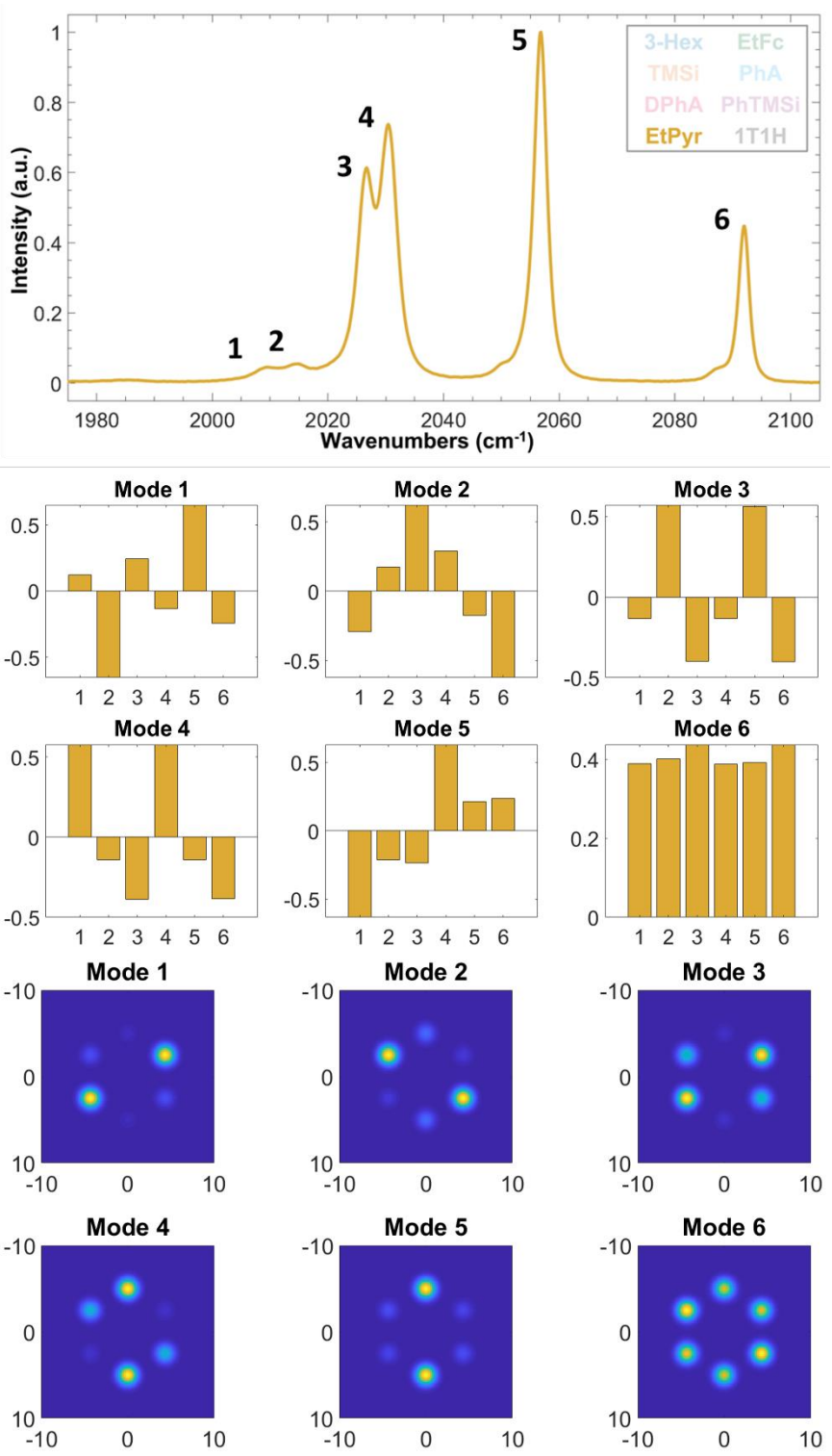

Figure A.4: (top-down) Linear absorption spectrum, normalized carbonyl displacements by vibrational mode, and carbonyl recruitment probability by vibrational mode for EtPyr-DCHC.

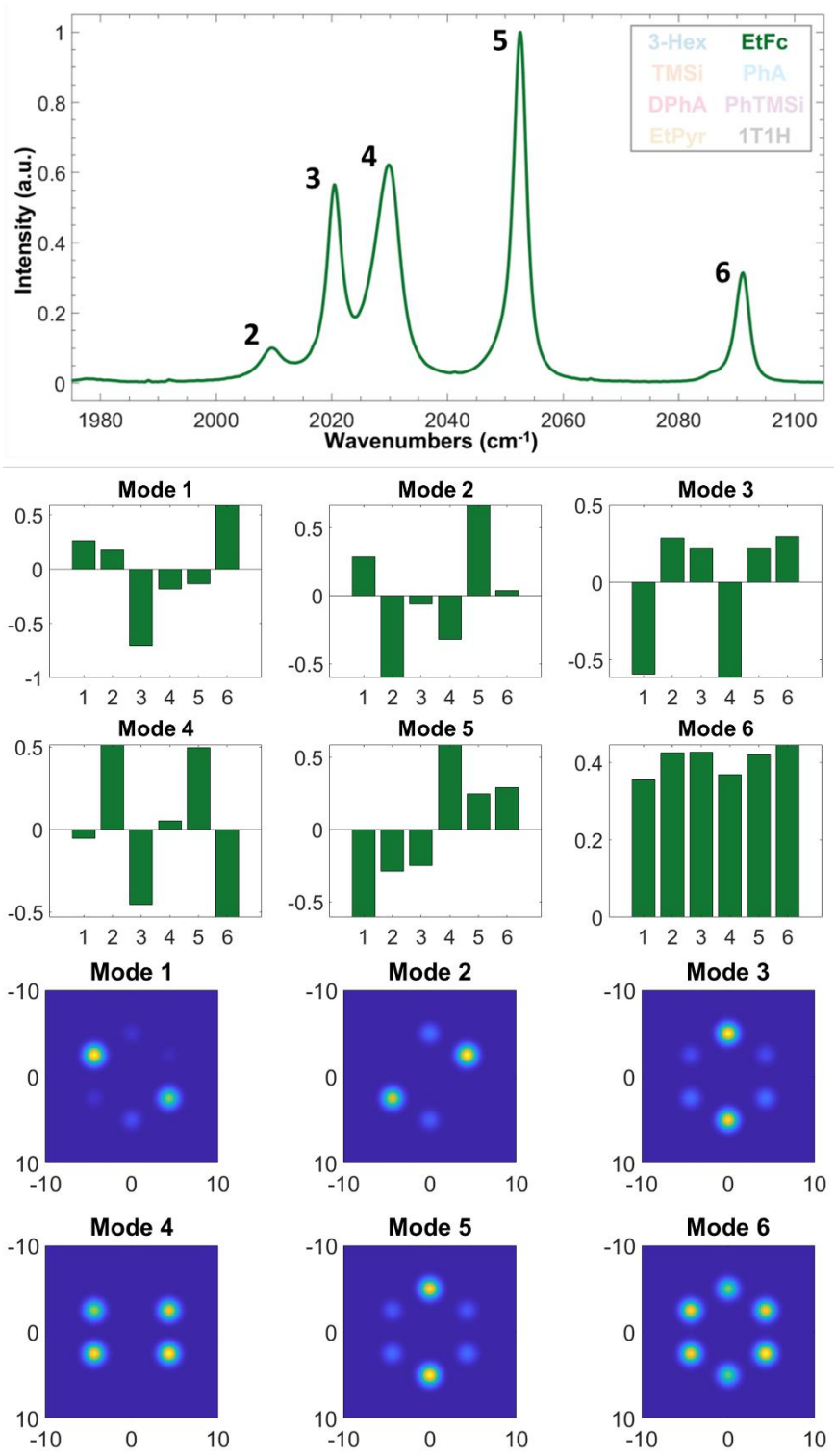

Figure A.5: (top-down) Linear absorption spectrum, normalized carbonyl displacements by vibrational mode, and carbonyl recruitment probability by vibrational mode for EtFc-DCHC.

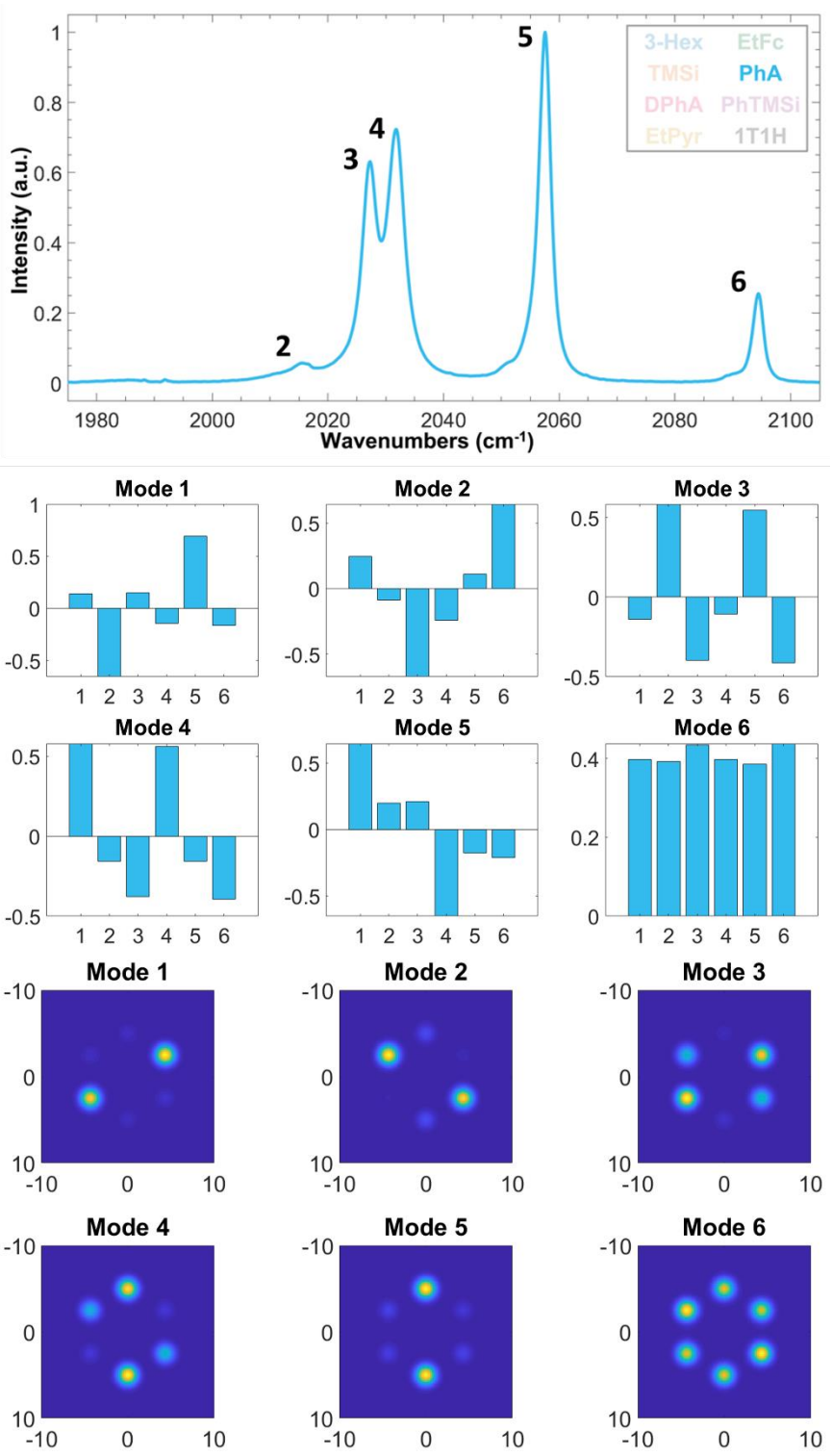

Figure A.6: (top-down) Linear absorption spectrum, normalized carbonyl displacements by vibrational mode, and carbonyl recruitment probability by vibrational mode for PhA-DCHC.

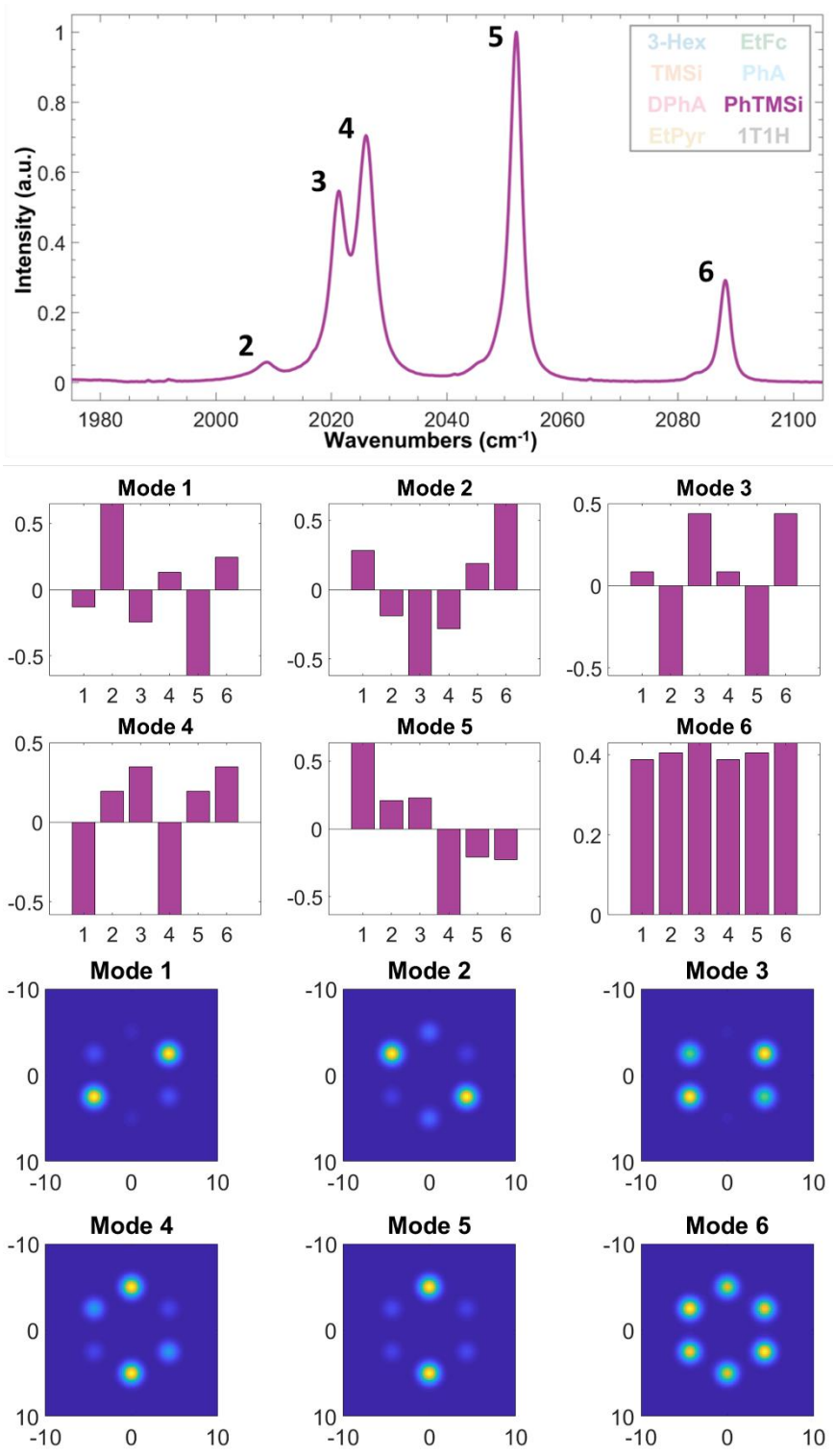

Figure A.7: (top-down) Linear absorption spectrum, normalized carbonyl displacements by vibrational mode, and carbonyl recruitment probability by vibrational mode for PhTMSi-DCHC.

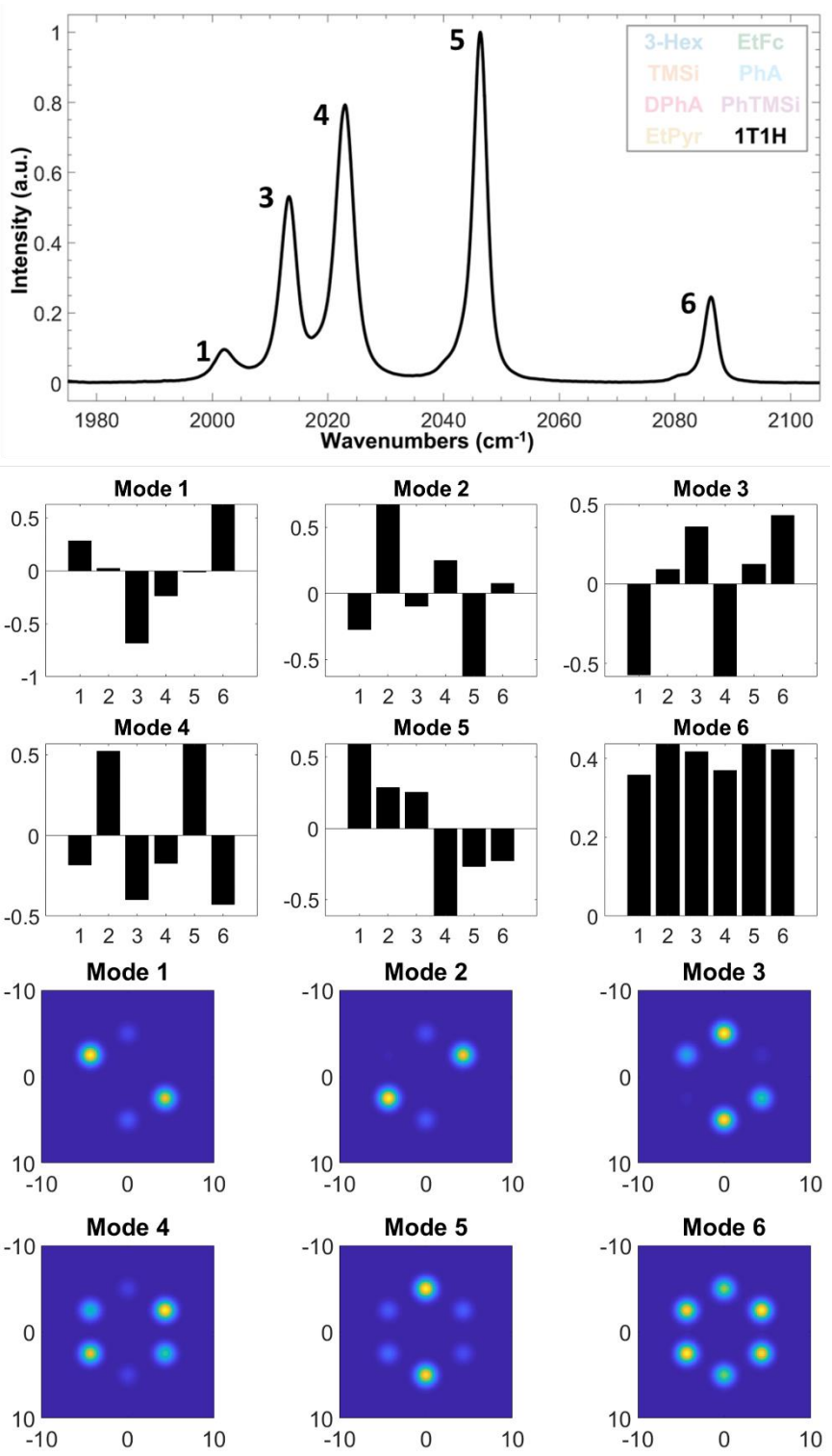

Figure A.8: (top-down) Linear absorption spectrum, normalized carbonyl displacements by vibrational mode, and carbonyl recruitment probability by vibrational mode for 1T1H-DCHC.

A.3 Difference Frequency Tables for Alkynyl DCHC Complexes

Table A.1: 3-Hex-DCHC Frequency Table

Mode	2002	2004*	2013	2024	2047	2088
2002	0					
2004*	2	0				
2013	11	9	0			
2024	22	20	11	0		
2047	45	43	34	23	0	
2088	86	84	75	64	41	0

*DFT-predicted dark mode

Table A.2: TMSi-DCHC Frequency Table

Mode	2003*	2003*	2014	2022	2046	2086
2003*	0					
2003*	0	0				
2014	11	11	0			
2022	19	19	8	0		
2046	43	43	32	24	0	
2086	83	72	72	64	40	0

*DFT-predicted degenerate modes

Table A.3: DPhA-DCHC Frequency Table

Mode	2010	2013	2026	2030	2056	2091
2010	0					
2013	3	0				
2026	16	13	0			
2030	20	17	4	0		
2056	46	43	30	26	0	
2091	81	78	65	61	35	0

Table A.4: EtPyr-DCHC Frequency Table

Mode	2009	2015	2027	2030	2057	2092
2009	0					
2015	6	0				
2027	18	12	0			
2030	21	15	3	0		
2057	48	42	30	27	0	
2092	83	77	65	62	35	0

Table A.5: EtFc-DCHC Frequency Table

Mode	2010*	2010*	2020	2030	2053	2091
2010*	0					
2010*	0	0				
2020	10	10	0			
2030	20	20	10	0		
2053	43	43	33	23	0	
2091	81	81	71	61	38	0

*DFT-predicted degenerate modes

Table A.6: PhA-DCHC Frequency Table

Mode	2011*	2015	2027	2032	2058	2094
2011*	0					
2015	4	0				
2027	16	12	0			
2032	21	17	5	0		
2058	47	43	31	26	0	
2094	83	79	67	62	36	0

*DFT-predicted dark mode

Table A.7: PhTMSi-DCHC Frequency Table

Mode	2007*	2009	2021	2026	2052	2088
2007*	0					
2009	2	0				
2021	14	12	0			
2026	19	17	5	0		
2052	45	43	31	26	0	
2088	81	79	67	62	36	0

*DFT-predicted dark mode

Table A.8: 1T1H-DCHC Frequency Table

Mode	2002	2006*	2013	2023	2046	2086
2002	0					
2006*	4	0				
2013	11	7	0			
2023	21	17	10	0		
2046	44	40	33	23	0	
2086	84	80	73	63	40	0

*DFT-predicted dark mode

A.4 2D-IR Spectra of Selected DCHC Complexes in *n*-dodecane

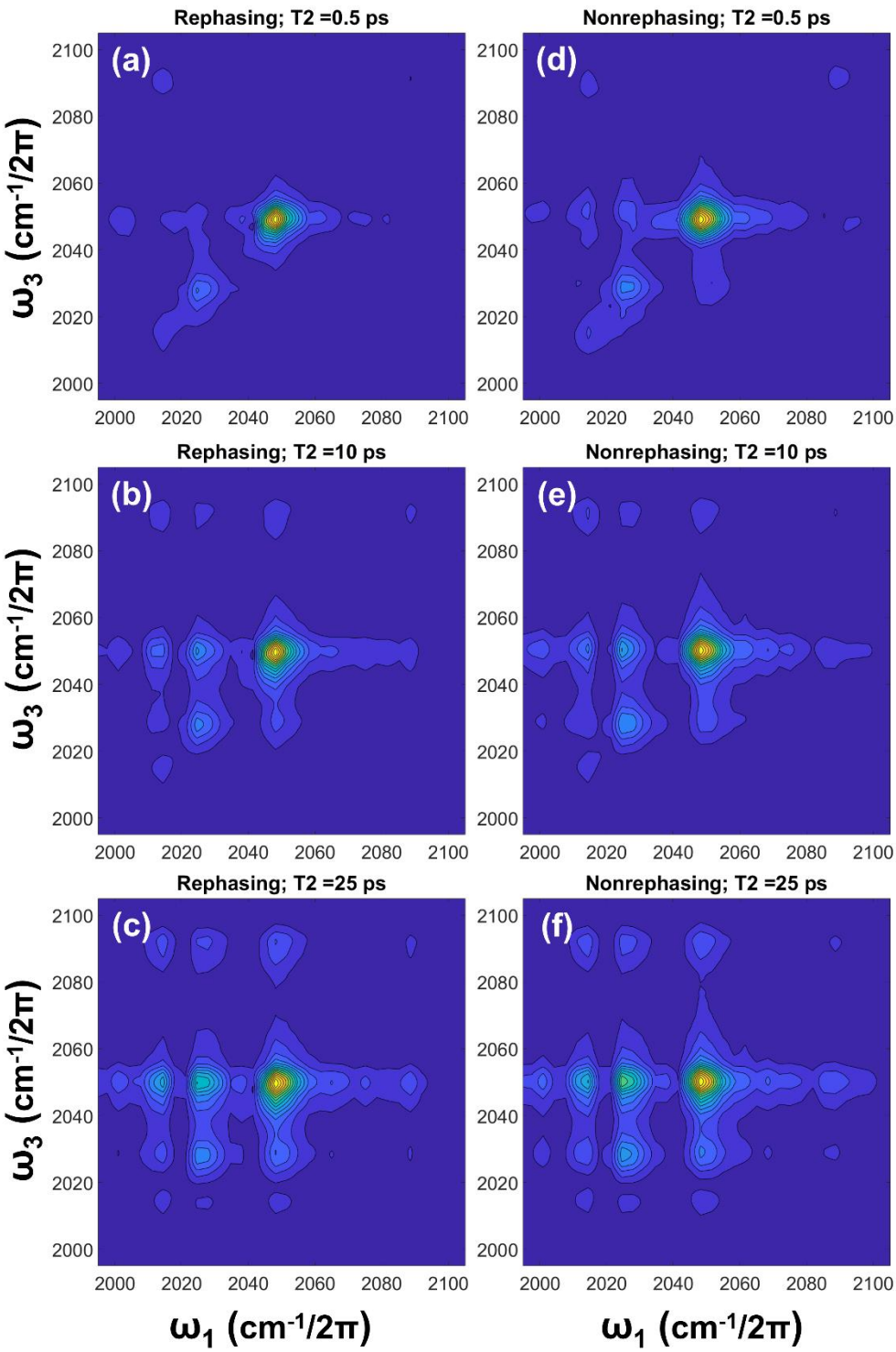

Figure A.9: 2D-IR spectra of 3-hex-DCHC in n-dodecane, featuring (a-c) rephasing and (d-f) nonrephasing spectra at t_2 = 0.5 ps, 10 ps, and 25 ps.

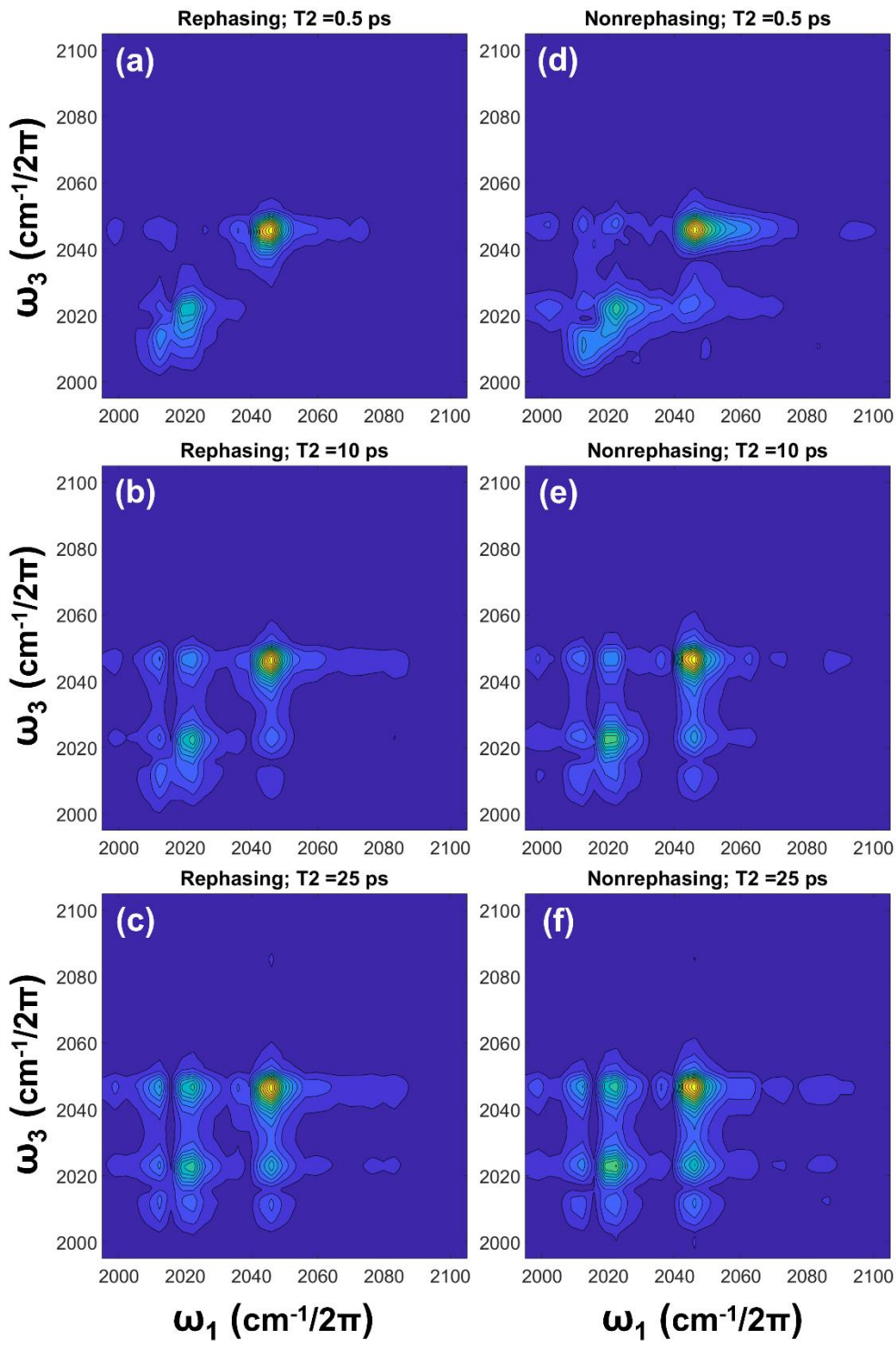

Figure A.9: 2D-IR spectra of TMSi-DCHC in n-dodecane, featuring (a-c) rephasing and (d-f) nonrephasing spectra at t_2 = 0.5 ps, 10 ps, and 25 ps.

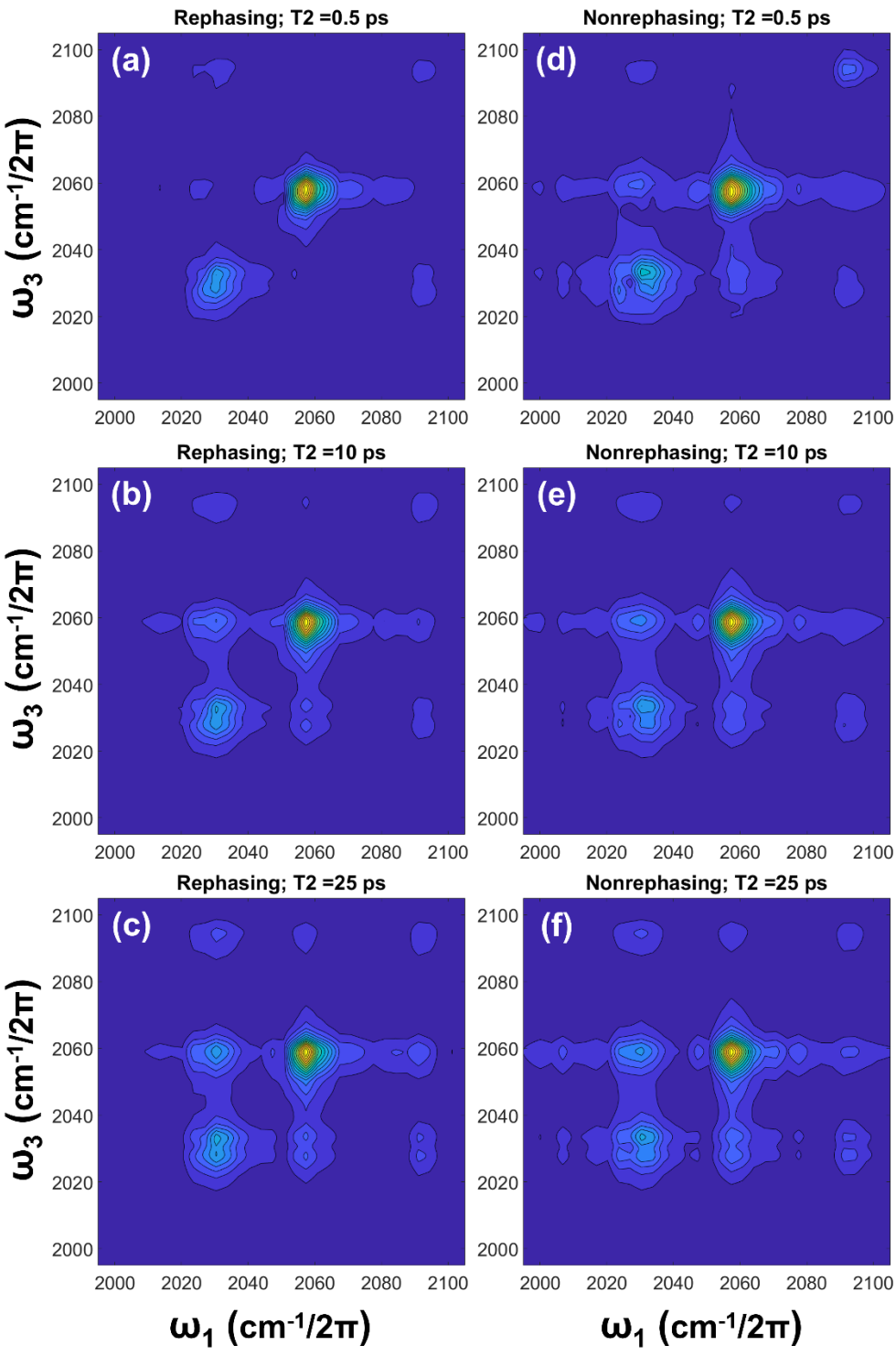

Figure A.10: 2D-IR spectra of EtPyr-DCHC in n-dodecane, featuring (a-c) rephasing and (d-f) nonrephasing spectra at t_2 = 0.5 ps, 10 ps, and 25 ps.

References

(1) Hamm, P.; Zanni, M. Concepts and Methods of 2D Infrared Spectroscopy; 2011.

(2) Khalil, M.; Demirdöven, N.; Tokmakoff, A. Vibrational Coherence Transfer Characterized with Fourier-Transform 2D IR Spectroscopy. J. Chem. Phys. 2004, 121 (1), 362–373. https://doi.org/10.1063/1.1756870.

(3) Crum, V. F.; Kiefer, L. M.; Kubarych, K. J. Ultrafast Vibrational Dynamics of a Solute Correlates with Dynamics of the Solvent. J. Chem. Phys. 2021, 155 (13). https://doi.org/10.1063/5.0061770.

(4) King, J. T.; Anna, J. M.; Kubarych, K. J. Solvent-Hindered Intramolecular Vibrational Redistribution. Phys. Chem. Chem. Phys. 2011, 13 (13), 5579–5583. https://doi.org/10.1039/c0cp02138e.

(5) Nilsen, I. A.; Osborne, D. G.; White, A. M.; Anna, J. M.; Kubarych, K. J. Monitoring Equilibrium Reaction Dynamics of a Nearly Barrierless Molecular Rotor Using Ultrafast Vibrational Echoes. J. Chem. Phys. 2014, 141 (13). https://doi.org/10.1063/1.4896536.

(6) Eckert, P. A.; Kubarych, K. J. Dynamic Flexibility of Hydrogenase Active Site Models Studied with 2D-IR Spectroscopy. J. Phys. Chem. A 2017, 121 (3), 608–615. https://doi.org/10.1021/acs.jpca.6b11962.

(7) Bullock, R. M.; Dey, A. Introduction: Catalysis beyond the First Coordination Sphere. Chem. Rev. 2022, 122 (14), 11897–11899. https://doi.org/10.1021/acs.chemrev.2c00428.

(8) Parker, G. L.; Van Lommel, R.; Roig, N.; Alonso, M.; Chaplin, A. B. Modulation of Metal Carbonyl Stretching Frequencies in the Second Coordination Sphere through the Internal Stark Effect. Chem. - A Eur. J. 2022, 28 (69). https://doi.org/10.1002/chem.202202283.

(9) Arpin, P. C.; Turner, D. B. Signatures of Vibrational and Electronic Quantum Beats in Femtosecond Coherence Spectra. J. Phys. Chem. A 2021, 125 (12), 2425–2435. https://doi.org/10.1021/acs.jpca.0c10807.

(10) Mitsunaga, M.; Tang, C. L. Theory of Quantum Beats in Optical Transmission-Correlation and Pump-Probe Measurements. Phys. Rev. A 1987, 35 (4), 1720–1728. https://doi.org/10.1103/PhysRevA.35.1720.

(11) Nee, M. J.; Baiz, C. R.; Anna, J. M.; McCanne, R.; Kubarych, K. J. Multilevel Vibrational Coherence Transfer and Wavepacket Dynamics Probed with Multidimensional IR Spectroscopy. J. Chem. Phys. 2008, 129 (8). https://doi.org/10.1063/1.2969900.

(12) Marroux, H. J. B.; Orr-Ewing, A. J. Distinguishing Population and Coherence Transfer Pathways in a Metal Dicarbonyl Complex Using Pulse-Shaped Two-Dimensional Infrared Spectroscopy. J. Phys. Chem. B 2016, 120 (17), 4125–4130. https://doi.org/10.1021/acs.jpcb.6b02979.

(13) Kupef, E.; Freeman, R. Multiple Hartmann-Hahn Coherence Transfer in Nuclear Magnetic Resonance Spectroscopy. J. Am. Chem. Soc. 1992, 114, 10671–10672.

(14) Womick, J. M.; Miller, S. A.; Moran, A. M. Probing the Dynamics of Intraband Electronic Coherences in Cylindrical Molecular Aggregates. J. Phys. Chem. A 2009, 113 (24), 6587–6598. https://doi.org/10.1021/jp811064z.

(15) Eckert, P. A.; Kubarych, K. J. Vibrational Coherence Transfer Illuminates Dark Modes in Models of the FeFe Hydrogenase Active Site. J. Chem. Phys. 2019, 151 (5), 1–16. https://doi.org/10.1063/1.5111016.

(16) Policht, V. R.; Niedringhaus, A.; Willow, R.; Laible, P. D.; Bocian, D. F.; Kirmaier, C.; Holten, D.; Mančal, T.; Ogilvie, J. P. Hidden Vibronic and Excitonic Structure and Vibronic Coherence Transfer in the Bacterial Reaction Center. Sci. Adv. 2022, 8 (1), 1–11. https://doi.org/10.1126/sciadv.abk0953.

(17) Niedringhaus, A.; Policht, V. R.; Sechrist, R.; Konar, A.; Laible, P. D.; Bocian, D. F.; Holten, D.; Kirmaier, C.; Ogilvie, J. P. Primary Processes in the Bacterial Reaction Center Probed by Two-Dimensional Electronic Spectroscopy. Proc. Natl. Acad. Sci. U. S. A. 2018, 115 (14), 3563–3568. https://doi.org/10.1073/pnas.1721927115.

(18) Heathcote, P.; Jones, M. R. The Structure-Function Relationships of Photosynthetic Reaction Centers; Elsevier Ltd., 2012; Vol. 8. https://doi.org/10.1016/B978-0-12-374920-8.00809-2.

(19) Zabret, J.; Bohn, S.; Schuller, S. K.; Arnolds, O.; Möller, M.; Meier-Credo, J.; Liauw, P.; Chan, A.; Tajkhorshid, E.; Langer, J. D.; Stoll, R.; Krieger-Liszkay, A.; Engel, B. D.; Rudack, T.; Schuller, J. M.; Nowaczyk, M. M. Structural Insights into Photosystem II Assembly. Nat. Plants 2021, 7 (4), 524–538. https://doi.org/10.1038/s41477-021-00895-0.

(20) Jagannathan, B.; Golbeck, J. H. Photosynthesis: Microbial. Encycl. Microbiol. Third Ed. 2009, 325–341. https://doi.org/10.1016/B978-012373944-5.00352-7.

(21) Jagannathan, B.; Golbeck, J. H. FX, FA, and FB Iron-Sulfur Clusters in Type I Photosynthetic Reaction Centers, 2nd ed.; Elsevier Inc., 2013; Vol. 3. https://doi.org/10.1016/B978-0-12-378630-2.00184-5.

(22) Cho, K. H.; Rhee, Y. M. Computational Elucidations on the Role of Vibrations in Energy Transfer Processes of Photosynthetic Complexes. Phys. Chem. Chem. Phys. 2021, 23 (47), 26623–26639. https://doi.org/10.1039/d1cp04615b.

(23) Kühn, O.; Chernyak, V.; Mukamel, S. Two-Exciton Spectroscopy of Photosynthetic Antenna Complexes: Collective Oscillator Analysis. J. Chem. Phys. 1996, 105 (19), 8586–8601. https://doi.org/10.1063/1.472642.

(24) Meier, T.; Chernyak, V.; Mukamel, S. Multiple Exciton Coherence Sizes in Photosynthetic Antenna Complexes Viewed by Pump-Probe Spectroscopy. J. Phys. Chem. B 1997, 101 (37), 7332–7342. https://doi.org/10.1021/jp970045v.

(25) Plenio, M. B.; Almeida, J.; Huelga, S. F. Origin of Long-Lived Oscillations in 2D-Spectra of a Quantum Vibronic Model: Electronic versus Vibrational Coherence. J. Chem. Phys. 2013, 139 (23). https://doi.org/10.1063/1.4846275.

(26) Fuller, F. D.; Pan, J.; Senlik, S. S.; Wilcox, D. E.; Ogilvie, J. P. Observation of Coherence in the Photosystem II Reaction Center. 2013, No. 2.

(27) Chenu, A.; Scholes, G. D. Coherence in Energy Transfer and Photosynthesis. Annu. Rev. Phys. Chem. 2015, 66, 69–96. https://doi.org/10.1146/annurev-physchem-040214-121713.

(28) Karak, P.; Ruud, K.; Chakrabarti, S. Demystifying the Origin of Vibrational Coherence Transfer between the S1and T1States of the Pt-Pop Complex. J. Phys. Chem. Lett. 2021, 12 (40), 9768–9773. https://doi.org/10.1021/acs.jpclett.1c02789.

(29) Husseini, F. S.; Robinson, D.; Hunt, N. T.; Parker, A. W.; Hirst, J. D. Computing Infrared Spectra of Proteins Using the Exciton Model. J. Comput. Chem. 2017, 38 (16), 1362–1375. https://doi.org/10.1002/jcc.24674.

(30) Baiz, C. R.; McCanne, R.; Kubarych, K. J. Transient Vibrational Echo versus Transient Absorption Spectroscopy: A Direct Experimental and Theoretical Comparison. Appl. Spectrosc. 2010, 64 (9), 1037–1044. https://doi.org/10.1366/000370210792434369.

(31) Anna, J. M.; Kubarych, K. J. Watching Solvent Friction Impede Ultrafast Barrier Crossings: A Direct Test of Kramers Theory. J. Chem. Phys. 2010, 133 (17). https://doi.org/10.1063/1.3492724.

(32) Kiefer, L. M.; Kubarych, K. J. Solvent-Dependent Dynamics of a Series of Rhenium Photoactivated Catalysts Measured with Ultrafast 2DIR. J. Phys. Chem. A 2015, 119 (6), 959–965. https://doi.org/10.1021/jp511686p.

(33) Timney, J. A. Metal Carbonyls; 2002; Vol. 30. https://doi.org/10.1039/9781847554192-00172.

(34) Montgomery, C. D. [Pi] π Backbonding in Carbonyl Complexes and Carbon–Oxygen Stretching Frequencies: A Molecular Modeling Exercise. J. Chem. Educ. 2007, 84 (1), 102. https://doi.org/10.1021/ed084p102.

(35) Koch, D.; Chen, Y.; Golub, P.; Manzhos, S. Revisiting π Backbonding: The Influence of d Orbitals on Metal-CO Bonds and Ligand Red Shifts. Phys. Chem. Chem. Phys. 2019, 21 (37), 20814–20821. https://doi.org/10.1039/c9cp04624k.

(36) Hocking, R. K.; Hambley, T. W. Database Analysis of Transition Metal Carbonyl Bond Lengths: Insight into the Periodicity of π Back-Bonding, σ Donation, and the Factors Affecting the Electronic Structure of the TM−C:O Moiety. Organometallics 2007, 26 (11), 2815–2823. https://doi.org/10.1021/om061072n.

(37) Bistoni, G.; Rampino, S.; Scafuri, N.; Ciancaleoni, G.; Zuccaccia, D.; Belpassi, L.; Tarantelli, F. How π Back-Donation Quantitatively Controls the CO Stretching Response in Classical and Non-Classical Metal Carbonyl Complexes. Chem. Sci. 2016, 7 (2), 1174–1184. https://doi.org/10.1039/C5SC02971F.

(38) Frenking, G.; Fernández, I.; Holzmann, N.; Pan, S.; Krossing, I.; Zhou, M. Metal-CO Bonding in Mononuclear Transition Metal Carbonyl Complexes. JACS Au 2021, 1 (5), 623–645. https://doi.org/10.1021/jacsau.1c00106.

(39) Assefa, M. K.; Devera, J. L.; Brathwaite, A. D.; Mosley, J. D.; Duncan, M. A. Vibrational Scaling Factors for Transition Metal Carbonyls. Chem. Phys. Lett. 2015, 640, 175–179. https://doi.org/10.1016/j.cplett.2015.10.031.

(40) Platts, J. A.; Evans, G. J. S.; Coogan, M. P.; Overgaard, J. Electronic Structure of the Alkyne-Bridged Dicobalt Hexacarbonyl Complex Co2 μ-C2H2 (CO)6: Evidence for

Singlet Diradical Character and Implications for Metal-Metal Bonding. Inorg. Chem. 2007, 46 (16), 6291–6298. https://doi.org/10.1021/ic070278t.

(41) Sly, W. G. The Molecular Configuration of Dicobalt Hexacarbonyl Diphenylacetylene. J. Am. Chem. Soc. 1959, 81 (1), 18–20. https://doi.org/10.1021/ja01510a005.

(42) Sly, W. G. The Molecular Configuration of Dicobalt Hexacarbonyl Diphenylacetylene. J. Am. Chem. Soc. 1959, 81 (1), 18–20. https://doi.org/10.1021/ja01510a005.

(43) Pauson, P. L.; Khand, I. U. Uses of Cobalt-Carbonyl Acetylene Complexes in Organic Synthesis. Ann. New York Acad. Sci. 1977, 2–14.

(44) Lockwood, R. F.; Nicholas, K. M. Transition Metal-Stabilized Carbenium Ions as Synthetic Intermediates. I. a-[(Alkynyl)Dicobalt Hexacarbonyl] Carbenium Ions as Propargylating Agents. Tetrahedron Lett. 1977, 48, 4163–4166.

(45) Happ, B.; Bartik, T.; Zucchi, C.; Rossi, M. C.; Ghelfi, F.; Palyi, G. On the Reactivity of Acetylenes Coordinated to Cobalt. 9. Effects of Substitution and Coordination on the LSC-NMR Chemical Shifts of the Sp Carbons of (P2-R1C2R2)Co2(CO)6 Complexes. Molecular Structure of (P2=PhC2SiPh3)Co2(CO)6. Organometallics 1995, 14, 809–819.

(46) Coleman, A.; Pryce, M. T. Synthesis , Electrochemistry , and Photophysical Properties of a Series of Luminescent Pyrene-Thiophene Dyads and the Corresponding Co 2 (CO) 6 Complexes. 2008, 47 (23), 10980–10990.

(47) Ott, I.; Schmidt, K.; Kircher, B.; Schumacher, P.; Wiglenda, T.; Gust, R. Antitumor-Active Cobalt-Alkyne Complexes Derived from Acetylsalicylic Acid: Studies on the Mode of Drug Action. J. Med. Chem. 2005, 48 (2), 622–629. https://doi.org/10.1021/jm049326z.

(48) Harvey, E. C.; Areephong, J.; Cafolla, A. A.; Long, C.; Browne, W. R.; Feringa, B. L.; Pryce, M. T. Incorporating Cobalt Carbonyl Moieties onto Ethynylthiophene-Based Dithienylcyclopentene Switches. 2. Electro- and Spectroelectrochemical Properties. Organometallics 2014, 33 (13), 3309–3319. https://doi.org/10.1021/om4005719.

(49) Milne, S. B.; Tallman, K. A.; Serwa, R.; Rouzer, C. A.; Armstrong, M. D.; Marnett, L. J.; Lukehart, C. M.; Porter, N. A.; Brown, H. A. Capture and Release of Alkyne-Derivatized Glycerophospholipids Using Cobalt Chemistry. Nat. Chem. Biol. 2010, 6 (3), 205–207. https://doi.org/10.1038/nchembio.311.

(50) Tallman, K. a; Armstrong, M. D.; Milne, S. B.; Marnett, L. J.; Brown, H. A.; Porter, N. a. Cobalt Carbonyl Complexes as Probes for Alkyne-Tagged Lipids. J. Lipid Res. 2013, 54 (3), 859–868. https://doi.org/10.1194/jlr.D033332.

(51) Baecker, D.; Sagasser, J.; Karaman, S.; Hörmann, A. A.; Gust, R. Development of Methylated Cobalt–Alkyne Complexes with Selective Cytotoxicity against COX-Positive Cancer Cell Lines. Arch. Pharm. (Weinheim). 2022, 355 (2), 1–8. https://doi.org/10.1002/ardp.202100408.

(52) Neukamm, M. A.; Pinto, A.; Metzler-Nolte, N. Synthesis and Cytotoxicity of a Cobaltcarbonyl-Alkyne Enkephalin Bioconjugate. Chem. Commun. 2008, No. 2, 232–234. https://doi.org/10.1039/b712886j.

(53) Balsells, J.; Vazquez, J.; Moyano, A.; Pericas, M. A.; Riera, A. Low-Energy Pathway for Pauson-Khand Reactions: Synthesis and Reactivity of Dicobalt Hexacarbonyl Complexes of Chiral Ynamines. J. Org. Chem. 2000, 65 (22), 7291–7302. https://doi.org/10.1021/jo000278+.

(54) Pericàs, M. A.; Balsells, J.; Castro, J.; Marchueta, I.; Moyano, A.; Riera, A.; Vázquez, J.; Verdaguer, X. Toward the Understanding of the Mechanism and Enantioselectivity of the Pauson-Khand Reaction. Theoretical and Experimental Studies. Pure Appl. Chem. 2002, 74 (1), 167–174. https://doi.org/10.1351/pac200274010167.

(55) Kellman, M. E. Group Theory of Coupled Oscillators: Normal Modes as Symmetry Breaking. J. Chem. Phys. 1982, 76 (9), 4528–4534. https://doi.org/10.1063/1.443577.

(56) Frisch, M. J.; Trucks, G. W.; Schlegel, H. B.; Scuseria, G. E.; Robb, M. A.; Cheeseman, J. R.; Scalmani, G.; Barone, V.; Mennucci, B.; Petersson, G. A.; Nakatsuji, H.; Caricato, M.; Li, X.; Hratchian, H. P.; Izmaylov, A. F.; Bloino, J.; Zheng, G.; Sonnenberg, D. J.; Hada, M.; Ehara, M.; Toyota, K.; Fukuda, R.; Hasegawa, J.; Ishida, M.; Nakajima, T.; Honda, Y.; Kitao, O.; Nakai, H.; Vreven, T.; Montgomery, J. A., J.; Peralta, J. E.; Ogliaro, F.; Bearpark, M.; Heyd, J. J.; Brothers, E.; Kudin, K. N.; Staroverov, V. N.; Kobayashi, R.; Normand, J.; Raghavachari, K.; Rendell, A.; Burant, J. C.; Iyengar, S. S.; Tomasi, J.; Cossi, M.; Rega, N.; Millam, J. M.; Klene, M.; Knox, J. E.; Cross, J. B.; Bakken, V.; Adamo, C.; Jaramillo, J.; Gomperts, R.; Stratmann, R. E.; Yazyev, O.; Austin, A. J.; Cammi, R.; Pomelli, C.; Ochterski, J. W.; Martin, R. L.; Morokuma, K.; Zakrzewski, V. G.; Voth, G. A.; Salvador, P.; Dannenberg, J. J.; Dapprich, S.; Daniels, A. D.; Farkas, Ö.; Foresman, J. B.; Ortiz, J. V.; Cioslowski, J.; Fox, D. J. Gaussian 09. Gaussian, Inc. Wallingford CT. 2009, pp 2–3. https://doi.org/111.

(57) Tiana, D.; Francisco, E.; Blanco, M. A.; MacChi, P.; Sironi, A.; Martín Pendás, A. Bonding in Classical and Nonclassical Transition Metal Carbonyls: The Interacting Quantum Atoms Perspective. J. Chem. Theory Comput. 2010, 6 (4), 1064–1074. https://doi.org/10.1021/ct9006629.

(58) King, J. T.; Baiz, C. R.; Kubarych, K. J. Solvent-Dependent Spectral Diffusion in a Hydrogen Bonded “Vibrational Aggregate.” J. Phys. Chem. A 2010, 114 (39), 10590–10604. https://doi.org/10.1021/jp106142u.

(59) Knowles, P. J. The Determination of Point Groups from Imprecise Molecular Geometries. J. Math. Chem. 2022, 60 (1), 161–171. https://doi.org/10.1007/s10910-021-01302-x.

(60) Lee, K. F.; Kubarych, K. J.; Bonvalet, A.; Joffre, M. Characterization of Mid-Infrared Femtosecond Pulses [Invited]. 2008, 25 (6), 54–62.

(61) Kaindl, R. A.; Wurm, M.; Reimann, K.; Hamm, P.; Weiner, A. M.; Woerner, M. Generation, Shaping, and Characterization of Intense Femtosecond Pulses Tunable from 3 to 20 Mm. J. Opt. Soc. Am. B 2000, 17 (12), 2086. https://doi.org/10.1364/JOSAB.17.002086.

(62) Cerullo, G.; Silvestri, S. De. Ultrafast Optical Parametric Amplifiers. Rev. Sci. Instrum. 2003, 74, 1–18. https://doi.org/10.1063/1.1523642.

(63) Nee, M. J.; McCanne, R.; Kubarych, K. J.; Joffre, M. Two-Dimensional Infrared Spectroscopy Detected by Chirped Pulse Upconversion. Opt. Lett. 2007, 32 (6), 713. https://doi.org/10.1364/OL.32.000713.

(64) Wynne, K.; Müller, M.; Brandt, D.; Van Voorst, J. D. W. Diagrammatic Density Matrix Analysis of the Raman Photon Echo. Chem. Phys. 1988, 125 (2–3), 211–223. https://doi.org/10.1016/0301-0104(88)87075-7.

(65) Ogilvie, J. P.; Kubarych, K. J. Multidimensional Electronic and Vibrational Spectroscopy. An Ultrafast Probe of Molecular Relaxation and Reaction Dynamics. In Advances in Atomic, Molecular and Optical Physics; Elsevier Inc., 2009; Vol. 57, pp 249–321. https://doi.org/10.1016/S1049-250X(09)57005-X.

(66) Jonas, D. M. Two-Dimensional Femtosecond Spectroscopy. Annu. Rev. Phys. Chem. 2003, 54 (1), 425–463. https://doi.org/10.1146/annurev.physchem.54.011002.103907.

(67) Mukamel, S. Principles of Nonlinear Optical Spectroscopy; 1995.

(68) Bowman, J. M. Self - Consistent Field Energies and Wavefunctions for Coupled Oscillators □. 2008, 610 (1978), 608–610.

(69) Khalil, M.; Demirdöven, N.; Tokmakoff, A. Obtaining Absorptive Line Shapes in Two-Dimensional Infrared Vibrational Correlation Spectra. Phys. Rev. Lett. 2003, 90 (4), 4. https://doi.org/10.1103/PhysRevLett.90.047401.

(70) Khalil, M.; Demirdöven, N.; Tokmakoff, A. Coherent 2D IR Spectroscopy: Molecular Structure and Dynamics in Solution. J. Phys. Chem. A 2003, 107 (27), 5258–5279. https://doi.org/10.1021/jp0219247.

(71) Ramakrishna, S.; Seideman, T. Coherence Spectroscopy in Dissipative Media: A Liouville Space Pathway Approach. J. Chem. Phys. 2005, 122 (8). https://doi.org/10.1063/1.1850891.

(72) Ge, A.; Rudshteyn, B.; Zhu, J.; Maurer, R. J.; Batista, V. S.; Lian, T. Electron-Hole-Pair-Induced Vibrational Energy Relaxation of Rhenium Catalysts on Gold Surfaces. J. Phys. Chem. Lett. 2018, 9 (2), 406–412. https://doi.org/10.1021/acs.jpclett.7b02885.

(73) Kiefer, L. M.; Kubarych, K. J. Two-Dimensional Infrared Spectroscopy of Coordination Complexes: From Solvent Dynamics to Photocatalysis. 1–46.

(74) Pakoulev, A. V.; Rickard, M. A.; Mathew, N. A.; Kornau, K. M.; Wright, J. C. Frequency-Domain Time-Resolved Four Wave Mixing Spectroscopy of Vibrational Coherence Transfer with Single-Color Excitation. J. Phys. Chem. A 2008, 112 (28), 6320–6329. https://doi.org/10.1021/jp711014h.

(75) Balzer, B.; Stock, G. Modeling of Decoherence and Dissipation in Nonadiabatic Photoreactions by an Effective-Scaling Nonsecular Redfield Algorithm. Chem. Phys. 2005, 310 (1–3), 33–41. https://doi.org/10.1016/j.chemphys.2004.10.001.

(76) Redfield, A. G. The Theory of Relaxation Processes; Academic Press Inc., 1965; Vol. 1. https://doi.org/10.1016/B978-1-4832-3114-3.50007-6.

(77) Baiz, C. R.; Kubarych, K. J.; Geva, E. Molecular Theory and Simulation of Coherence Transfer in Metal Carbonyls and Its Signature on Multidimensional Infrared Spectra. J. Phys. Chem. B 2011, 115 (18), 5322–5339. https://doi.org/10.1021/jp109357d.

(78) Gao, H.; McCormick, A. J.; Roston, R. L.; Lu, Y. Editorial: Structure and Function of Chloroplasts, Volume III. Front. Plant Sci. 2023, 14 (March), 1–4. https://doi.org/10.3389/fpls.2023.1145680.

(79) Lancaster, C. R. D. Purple Bacteria: Photosynthetic Reaction Centers, 2nd ed.; Elsevier Inc., 2013; Vol. 9. https://doi.org/10.1016/B978-0-12-378630-2.00148-1.

(80) Harvey, E. C.; Areephong, J.; Cafolla, A. A.; Long, C.; Browne, W. R.; Feringa, B. L.; Pryce, M. T. Incorporating Cobalt Carbonyl Moieties onto Ethynylthiophene- Based Dithienylcyclopentene Switches. 2. Electro- and Spectroelectrochemical Properties. 2014. https://doi.org/10.1021/om4005719.

(81) Krafft, M. E.; Boñaga, L. V. R.; Hirosawa, C. Practical Cobalt Carbonyl Catalysis in the Thermal Pauson-Khand Reaction: Efficiency Enhancement Using Lewis Bases. J. Org. Chem. 2001, 66 (9), 3004–3020. https://doi.org/10.1021/jo0057708.

(82) Gibson, S. E.; Stevenazzi, A. The Pauson-Khand Reaction: The Catalytic Age Is Here! Angew. Chemie - Int. Ed. 2003, 42 (16), 1800–1810. https://doi.org/10.1002/anie.200200547.

(83) Hwu, J. R.; Wang, N. Steric Influence of the Trimethylsilyl Group in Organic Reactions. Chem. Rev. 1989, 89 (7), 1599–1615. https://doi.org/10.1021/cr00097a014.

(84) Paleček, D.; Edlund, P.; Westenhoff, S.; Zigmantas, D. Quantum Coherence as a Witness of Vibronically Hot Energy Transfer in Bacterial Reaction Center. Sci. Adv. 2017, 3 (9). https://doi.org/10.1126/sciadv.1603141.

(85) Links, D. A. Catch and Release of Alkyne-Tagged Molecules in Water by a Polymer-Supported Cobalt Complex†. 2011, 2, 7667–7670. https://doi.org/10.1039/c1ob06123b.

(86) Osella, D.; Galeotti, F.; Cavigiolio, G.; Nervi, C.; Hardcastle, K. I.; Vessières, A.; Jaouen, G. The Hexacarbonyl(Ethyne)Dicobalt Unit: An Androgen Tag. Helv. Chim. Acta 2002, 85 (9), 2918–2925. https://doi.org/10.1002/1522-2675(200209)85:9<2918::AID-HLCA2918>3.0.CO;2-W.

(87) Hocking, R. K.; Hambley, T. W. Structural Insights into Transition-Metal Carbonyl Bonding †. Read 2006, No. April 2003, 1516–1517.

(88) Kowalski, K.; Hikisz, P.; Szczupak, Ł.; Therrien, B.; Koceva-Chyła, A. Ferrocenyl and Dicobalt Hexacarbonyl Chromones - New Organometallics Inducing Oxidative Stress and Arresting Human Cancer Cells in G2/M Phase. Eur. J. Med. Chem. 2014, 81, 289–300. https://doi.org/10.1016/j.ejmech.2014.05.023.

(89) Štěpnička, P.; Trojan, L.; Kubišta, J.; Ludvík, J. Internal Ferrocenylalkynes—a Comparative Electrochemical and Mass Spectrometric Study. J. Organomet. Chem. 2001, 637–639, 291–299. https://doi.org/10.1016/S0022-328X(01)00922-6.

(90) Moore, A.; Ortin, Y.; Müller-Bunz, H.; McGlinchey, M. J. Alkynyl-Dicobalt Hexacarbonyl Complexes of Menthyl Cations: Isolobal Substitution of [Co(CO)3]+ by Fe(CO)3 as a Structural Model. Organometallics 2010, 29 (21), 4882–4892. https://doi.org/10.1021/om100107x.

(91) Zall, C. M.; Clouston, L. J.; Young, V. G.; Ding, K.; Kim, H. J.; Zherebetskyy, D.; Chen, Y. S.; Bill, E.; Gagliardi, L.; Lu, C. C. Mixed-Valent Dicobalt and Iron-Cobalt

Complexes with High-Spin Configurations and Short Metal-Metal Bonds. Inorg. Chem. 2013, 52 (16), 9216–9228. https://doi.org/10.1021/ic400292g.

(92) Aime, S.; Osella, M.; Generale, C.; Corso, I. U.; Massimo, V. COMPLEXES , [μ-(1-σ, 2-3, η2-R2C-C≡CR')][(CO)3Fe-Co(CO)3] AND [μ-(1-σ, 2-3, η2-H2C-C≡CCH2OH)][(CO)3Fe-Co(CO)2(PPh3)] 1. 1983, 2 (2).

(93) Kiefer, L. M.; Michocki, L. B.; Kubarych, K. J. Transmission Mode 2D-IR Spectroelectrochemistry of in Situ Electrocatalytic Intermediates. J. Phys. Chem. Lett. 2021, 12 (15), 3712–3717. https://doi.org/10.1021/acs.jpclett.1c00504.

(94) Zwan, G. Van Der. Derivation of the Redfield Relaxation Equation. 2003, 1–13.